

# POLITECNICO DI TORINO

**Corso di Laurea Magistrale in Ingegneria Elettrica**

**Tesi di Laurea Magistrale**

## **DESIGN PROCEDURE OF SURFACE-MOUNTED PM MACHINES BASED ON ANALYTICAL SIZING**



### **Relatori**

Prof. Alberto Tenconi

Prof. Andrea Cavagnino

Ing. Silvio Vaschetto

### **Candidato**

Loris Altamore

Ottobre 2017

# Sommario

L’approccio per la progettazione di nuove macchine elettriche prevede generalmente l’utilizzo combinato dei dati di macchine già esistenti e quello di software commerciali analitici o agli elementi finiti. Tuttavia, le potenzialità di questi software si possono pienamente sfruttare solo quando le dimensioni della macchina che si sta progettando e le sue proprietà, in termini di avvolgimento e materiali utilizzati, si conoscono già in linea di massima. Qualora le specifiche geometriche non siano quelle standard, tale approccio è evidentemente inadeguato anche solo per avere un’idea preliminare sulle dimensioni della macchina e quindi sui costi. Questo perché la struttura non è nota neanche in maniera approssimativa e i tempi necessari all’ottenimento del progetto finale risulterebbero estremamente lunghi. Questo elaborato si propone perciò l’obiettivo di realizzare uno strumento per la progettazione di macchine elettriche con un algoritmo che non preveda l’utilizzo di software agli elementi finiti e di dati di motori già esistenti. Il software è stato sviluppato per la progettazione di macchine sincrone a magneti permanenti superficiali.

Nella prima parte della tesi vengono presentate le principali caratteristiche costruttive e le linee guida per la progettazione per questa tipologia di macchine. Viene in particolare evidenziato come la scelta del tipo di avvolgimento, del numero di poli e di cave influisca sulle performance della macchina in termini di tensione indotta, coppia, coppia di impuntamento e deflussaggio.

Nella seconda parte della tesi viene invece presentato il software, chiamato *SMDT (SPM Machine Design Tool)*. Quest’ultimo è stato realizzato in ambiente MATLAB® e presenta un’interfaccia grafica che permette l’inserimento delle specifiche di progetto e la visualizzazione dei risultati. Nell’algoritmo di dimensionamento sono state implementate equazioni elettromagnetiche ben note dai corsi universitari di macchine elettriche, e altre reperibili in letteratura. Queste equazioni sono inserite in un processo iterativo che, a partire dalle specifiche di progetto, prevede l’aumento progressivo delle dimensioni della macchina, diametri e lunghezza assiale. Le iterazioni si concludono al raggiungimento dell’obiettivo di coppia, nel rispetto dei vincoli sulle sollecitazioni dei materiali imposte dal progettista.

---

## *Sommario*

---

Nella terza parte, invece, viene preso come caso di studio una macchina per applicazioni aeronautiche, rotante a 2400 rpm e in grado di fornire 40 Nm di coppia al sincronismo. In particolare, i criteri progettuali hanno condotto alla scelta di una macchina a 28 poli e 24 cave, con avvolgimento concentrato, rotore esterno e frequenza nominale di 560 Hz. Il raffreddamento previsto è ad aria forzata. Le cave sono rettangolari, mentre i magneti sono stati scelti di materiale alle terre rare (NdFeB). I risultati ottenuti dal software, in termini di dimensioni dei lamierini e dati di targa, sono stati validati con un tool aggiuntivo e integrato in *SMDT*. Questo permette di realizzare alcune analisi agli elementi finiti in ambiente FEMM, in particolare in termini di tensione indotta, coppia al sincronismo, coppia in deflussaggio e valutazione delle induzioni massime nei punti critici della struttura magnetica.

I risultati ottenuti con *SMDT*, se confrontati con quelli ottenuti mediante il tool, sono molto positivi in quanto le differenze percentuali sulla tensione indotta e sulla coppia sono rispettivamente del +1.3 % e del +5 %. Risultati soddisfacenti sono stati ottenuti anche in termini di sollecitazioni magnetiche nei gioghi, nei denti e nel traferro.

Quanto ottenuto porta quindi ad affermare che *SMDT* rappresenta uno strumento molto utile per ottenere un dimensionamento preliminare della macchina. Tuttavia, il progetto del motore non rappresenta ancora quello definitivo in quanto necessita di essere ottimizzato e migliorato. In tal senso i software agli elementi finiti forniscono sicuramente il supporto necessario.

# Abstract

The approach for the design of a new electrical machine generally involves the combined use of the data of pre-existing projects and the use of analytical or Finite-Element Method commercial software (FEMs). However, the potential of these software can be fully exploited only when the size of such machine and its features in terms of winding and materials used are already known preliminarily. However, if the geometric features are not standard, then the designer has to start the design from scratch. Hence, this approach is obviously inadequate if an idea about the machine size, and therefore its costs, is needed in short times. This is because the structure of the machine is not known, not even roughly, and the time required to obtain the final project could be extremely long. Hence, the purpose of this work is to provide a tool for the design of electrical machines, which does not require the use of FEMs and the data of pre-existing projects, but in which only well-known electromagnetic equations are implemented. To be more specific, it has been decided to develop the software for the design of synchronous machines with Surface-Mounted Permanent-Magnets (SPM).

Firstly, the main constructive features and design guidelines of SPM machines are presented. In particular, it is shown how the choice of the winding type, number of poles and slots affects the machine performances in terms of back-EMF, torque, cogging torque and field-weakening.

Secondly, the software called *SMDT (SPM Machine Design Tool)* is introduced. It has been developed in MATLAB® environment and it has a graphical interface that allows the insertion of the project specifications and the display of the results. As previously mentioned, well-known electromagnetic equations have been implemented in the sizing algorithm, partly learned during the electrical machines courses and partly available in literature. These equations are within an iterative process that, starting from the design specifications, involves the progressive increase of machine dimensions until the target torque is achieved, respecting the material solicitations imposed as constraints by the designer.

---

---

*Abstract*

---

Lastly, the project of a motor for aeronautical application rotating at 2400 rpm and capable of providing 40 Nm at synchronism is presented. In particular, the design criteria have lead to the choice of a 28-pole and 24-slots machine with a concentrated winding and a rated frequency of 560 Hz. The rotor is external and an external fan provides the cooling. The slots are rectangular-shaped and the magnets have been chosen made of rare earth material (NdFeB).

The results obtained by the software, in terms of laminations size and rated data, has been validated with an additional tool integrated into *SMDT*. It has developed with Octave, a MATLAB® tool that allow to communicate with FEMM, and it permits to carry out some Finite-Element analyses, in terms of induced voltage, torque at the synchronous speed and maximum flux density in the critical points of the magnetic structure.

The results obtained with *SMDT*, when compared with those obtained through the tool, are very satisfactory, as the percentage differences on induced voltage and torque are equal to +1.3 % and +5 %, respectively. Satisfactory results are also obtained in terms of resulting magnetic stresses in the yokes, teeth and air gap.

It is possible to state that *SMDT* is a very useful tool for obtaining a preliminary sizing of the machine. However, the project is not the definitive one, as it needs to be optimized and improved and, in this regard, FEMs surely provide the necessary support.

# Contents

<b>Sommario .....</b>	<b>i</b>
<b>Abstract .....</b>	<b>iii</b>
<b>Contents.....</b>	<b>v</b>
<b>List of figures .....</b>	<b>ix</b>
<b>List of tables .....</b>	<b>xii</b>
<b>Symbols and acronyms.....</b>	<b>xiii</b>
<b>1 Introduction.....</b>	<b>1</b>
1.1 Background.....	1
1.2 Thesis objective .....	2
1.3 Thesis outline.....	2
<b>2 SPM machines: literature review .....</b>	<b>4</b>
2.1 Introduction.....	4
2.2 Stator.....	5
2.2.1 Stator structure.....	5
2.2.1.1 Influence of stator slots: Carter's coefficient .....	6
2.2.1.2 Slot shape: slot fill factor .....	7
2.2.2 Winding layout .....	9
2.2.2.1 Introduction.....	9
2.2.2.2 Distributed winding.....	10
2.2.2.3 Fractional – Slot Concentrated Winding .....	11
2.3 Rotor .....	14

---

## *Contents*

---

2.3.1 Rotor configuration: inner versus outer rotor .....	14
2.3.2 Permanent magnets.....	15
2.3.2.1 Magnetic parameters and demagnetization curve .....	15
2.3.2.2 Permanent-Magnets for SPM machines .....	17
2.3.2.3 Operating point.....	18
2.4 Electric and magnetic equations .....	20
2.4.1 Hypothesis .....	20
2.4.2 Stator reference frame .....	20
2.4.2.1 Synchronous reference frame.....	23
2.5 Cogging torque .....	25
2.6 SPM motor drive.....	27
2.6.1 MPTA .....	27
2.6.2 Flux-weakening .....	27
2.6.3 Maximum speed .....	29
2.6.4 Characteristic current.....	30
<b>3 SMDT: SPM Machine Design Tool .....</b>	<b>31</b>
3.1 Introduction.....	31
3.2 Input user interface .....	32
3.2.1 Rated data .....	34
3.2.2 Stress indexes .....	35
3.2.3 Geometry .....	37
3.2.4 Winding .....	38
3.2.5 Materials .....	39
3.2.6 Core properties and push buttons .....	41
3.3 Output user interface.....	41
3.4 Finite–element Analysis tool .....	43
3.4.1 Introduction .....	43
3.4.2 Machine geometry and materials set up .....	44
3.4.3 Air gap flux density .....	45
3.4.4 Back-EMF .....	45
3.4.5 Torque.....	47
3.4.6 Power-speed curve.....	48

---

## Contents

---

<b>4 Analytical design procedure .....</b>	<b>50</b>
4.1 Introduction.....	50
4.2 Iterative sizing procedures .....	52
4.2.1 Air gap flux density .....	52
4.2.2 Sizing routine for inner-rotor machine .....	55
4.2.2.1 Rotor lamination design .....	55
4.2.2.2 Stator lamination design.....	57
4.2.2.3 Sizing conclusion .....	63
4.2.2.4 Exit condition.....	63
4.2.3 Sizing routine for outer-rotor machine .....	65
4.2.3.1 Stator lamination design.....	65
4.2.3.2 Exit condition.....	70
4.2.3.3 Rotor lamination design .....	71
4.3 Stator winding length.....	71
4.3.1 Distributed winding .....	73
4.3.2 Fractional-Slot Concentrated Winding.....	74
4.4 Total volume and weight of the machine .....	75
4.5 Loss models .....	77
4.6 Equivalent circuit paramaters .....	79
4.6.1 Stator resistance .....	80
4.6.2 Synchronous inductance for distributed winding .....	81
4.6.2.1 Main inductance .....	81
4.6.2.2 Slot leakage inductance .....	82
4.6.2.3 End-winding leakage inductance.....	85
4.6.3 Synchronous inductance for FSCW .....	85
4.6.4 Number of conductor in series per phase .....	86
<b>5 Prototype design and Finite-Element validation.....</b>	<b>88</b>
5.1 Introduction.....	88
5.1.1 Design specifications and target data .....	88
5.1.2 Material properties.....	91
5.1.2.1 Winding.....	91
5.1.2.2 Core .....	91

---

*Contents*

---

5.1.2.3 Magnet.....	93
5.1.3 Design results .....	94
5.1.4 FEMM analysis.....	96
5.1.4.1 No-load operation.....	97
5.1.4.2 Load working operation .....	102
<b>6 Conclusions and future work.....</b>	<b>106</b>
6.1 Conclusions.....	106
6.2 Future work.....	107
<b>Appendix A : Calculation of magnetizing inductance.....</b>	<b>108</b>
<b>Appendix B : Calculation of slot leakage inductance.....</b>	<b>110</b>
<b>Bibliography.....</b>	<b>115</b>
<b>Acknowledgements .....</b>	<b>119</b>

# List of figures

Figure 2.1: Example of SPM synchronous machine .....	4
Figure 2.2: Slotless and slotted motor .....	5
Figure 2.3: Air gap flux density under the stator slots .....	6
Figure 2.4: Rectangular and trapezoidal slot.....	7
Figure 2.5: Cross-section of trapezoidal slot filled by conductors with round cross-section.....	8
Figure 2.6: Types of winding layout: a) overlapping distributed b) overlapping concentrated c) non-overlapping double layer d) non-overlapping single layer [32].....	9
Figure 2.7: Single layer versus double layer [11] .....	11
Figure 2.8: Magnetic forces with 68 poles and 69 slots a) and b), 60 poles and 72 slots c), 10 poles and 12 slots d). Figure obtained from [11].....	12
Figure 2.9: Inner and outer rotor configuration for 24 slots - 28 poles motor.....	14
Figure 2.10: Airgap diameter for inner and outer rotor with the same external diameter [11] ...	15
Figure 2.11: Permanent magnet hysteresis loop [31].....	16
Figure 2.12: Typical demagnetization curves [13].....	17
Figure 2.13: Magnetic circuit with PM .....	18
Figure 2.14: Windings representation .....	20
Figure 2.15: Synchronous rotor frame .....	23
Figure 2.16: Cogging torque. Figure extrapolated from [11].....	25
Figure 2.17: Equilibrium positions between pole pair axis and tooth.....	25
Figure 2.18: Typical waveform of the cogging torque ( $N_c$ stands for number of slots) [9].....	26
Figure 2.19: Magnetic energy stored in the airgap and cogging torque [31] .....	26
Figure 2.20: Current and flux trajectory [20] .....	28
Figure 2.21: Power and torque versus speed curve .....	28
Figure 2.22: Normalized power curve [20].....	29

---

---

*List of figures*

---

Figure 3.1: GUI for design specification and materials .....	33
Figure 3.2: <i>Rated data</i> panel .....	34
Figure 3.3: <i>Stress indexes</i> panel .....	35
Figure 3.4: Recommended design flux densities [22] .....	36
Figure 3.5: Recommended values for current density and linear current density [22] .....	36
Figure 3.6: <i>Geometry</i> panel.....	37
Figure 3.7: Slot example .....	38
Figure 3.8: <i>Winding</i> panel.....	38
Figure 3.9: Example of winding with double layer.....	39
Figure 3.10: <i>Materials</i> panel .....	40
Figure 3.11: a) <i>Core properties</i> panel b) <i>Project/Reset</i> buttons.....	41
Figure 3.12: GUI for the results visualization.....	42
Figure 3.13: GUI for FE analysis .....	43
Figure 3.14: Outer-rotor motor and inner-rotor motor in FEMM .....	44
Figure 3.15: Distributed winding layout .....	45
Figure 3.16: Selection of the slots.....	46
Figure 3.17: Alignment of the rotor with the phase A .....	47
Figure 3.18: Anti-Clockwise and clockwise arrangement of the winding .....	48
Figure 4.1: Sizing algorithm for outer- and inner-rotor motor.....	51
Figure 4.2: Operating point of the PM .....	52
Figure 4.3: Airgap flux density .....	53
Figure 4.4: Cross-section of a SPM synchronous machine with inner rotor.....	55
Figure 4.5: Flux per pole.....	56
Figure 4.6: Shunt effect of the magnetic field lines .....	60
Figure 4.7: Rectangular slot in SPM machines with inner rotor .....	61
Figure 4.8: Trapezoidal slot in SPM machines with inner rotor .....	62
Figure 4.9: Tapered slots [26] .....	63
Figure 4.10: Cross-section of a SPM synchronous machine with outer rotor .....	65
Figure 4.11: Trapezoidal slot in SPM machines with outer rotor .....	67
Figure 4.12: Critical diameter [26].....	68
Figure 4.13: Rectangular slot in SPM machines with outer rotor .....	69
Figure 4.14: Best area available in a triangular slot [26] .....	69

---

---

*List of figures*

---

Figure 4.15: Slots model in SPM machines with inner rotor .....	72
Figure 4.16: Slots model in SPM machines with outer rotor .....	73
Figure 4.17: Winding model .....	73
Figure 4.18: Minimum and Maximum end-winding lengths in FSCW .....	75
Figure 4.19: One-phase equivalent circuit .....	79
Figure 4.20: Slot layers .....	83
Figure 4.21: $Kt0$ , $Kt1$ , $Kt01$ [30].....	84
Figure 5.1: Air flowing inside the motor [32].....	90
Figure 5.2: COGENT NO20 and VACOFLUX 50 specific losses at 50 Hz .....	91
Figure 5.3: COGENT NO20 specific losses at different frequencies .....	92
Figure 5.4: B-H curve of COGENT NO20 .....	92
Figure 5.5: FEMM model of the machine.....	95
Figure 5.6: Magnetic field distribution .....	97
Figure 5.7: Air gap flux density along on pole pair .....	97
Figure 5.8: Air gap flux density along half motor.....	98
Figure 5.9: Harmonic content of the air gap flux density .....	98
Figure 5.10: Zigzag leakage flux.....	99
Figure 5.11: Back-EMF obtained with FEA .....	100
Figure 5.12: Harmonic spectrum of the back-EMF .....	101
Figure 5.13: Cogging torque along one pole pair.....	101
Figure 5.14: Harmonic spectrum of the cogging torque along one pole pair.....	102
Figure 5.15: Torque at the synchronous speed.....	103
Figure 5.16: Magnet flux linkage .....	104
Figure 5.17: Torque versus speed .....	104
Figure 5.18: Power versus speed.....	105
Figure B.1: Trapezoidal slot and its subdivisions. ....	110

---

## List of tables

Table 2.1: Fundamental winding factor for several slots-poles combinations .....	13
Table 2.2: Typical properties of rare-earth magnets .....	18
Table 4.1: Typical values of $K_{s,max} \cdot J_s$ .....	64
Table 4.2: Typical values of $k_{hys}$ and $k_{eddy}$ . Table extracted from [28] .....	78
Table 4.3: Heights and average width of layers .....	83
Table 5.1: Design specifications .....	89
Table 5.2: N25EH properties .....	93
Table 5.3: Materials used properties .....	93
Table 5.4: Prototype's dimensions .....	94
Table 5.5: Prototype's features.....	95
Table 5.6: Peak value of the airgap flux density .....	99
Table 5.7: Maximum values of flux density in the critical points of the machine .....	99
Table 5.8: Comparison between tool and FEMM resulting back-EMF .....	100
Table 5.9: Comparison between the obtained values of the torque.....	102
Table 5.10: Cogging torque and torque ripple compared to the average torque. ....	102

# Symbols and acronyms

## Symbols

$A_{ag}$	Air gap area (Chapter 2)
$A_{cu}$	Total area of slot conductors
$A_m$	Magnet area (Chapter 2)
$A_{ts}$	Slot total area
$A_{us}$	Slot useful area
$A_{wire}$	Conductor area
$B_{1g}$	Fundamental air gap flux density
$B_g$	Air gap flux density
$(BH)_{max}$	Maximum density product
$B_{knee}$	flux density's knee of normal demagnetization curve
$B_m$	Operating magnet flux density (Chapter 2)
$B_r$	Remanence
$B_{ts,max}$	Maximum teeth flux density
$B_{yr}$	Actual rotor yoke flux density
$B_{yr,max}$	Maximum rotor yoke flux density
$B_{ys,max}$	Maximum stator yoke flux density

$\cos\varphi$	Power factor
$C_p$	Iron specific losses (50 Hz, 1T)
$D_{ag}$	Air gap diameter
$D_{a,s}$	Diameter at mid-height of the slot
$D_{a,yr}$	Diameter at mid-height of rotor yoke
$D_{a,ys}$	Diameter at mid-height of stator yoke
$D_{crit}$	Critical diameter
$D_d$	Iterative step
$D_{er}$	Rotor external diameter
$D_{es}$	Stator external diameter
$D_{h1}$	Enclosure diameter
$D_{ir}$	Rotor internal diameter
$D_{is}$	Stator internal diameter
$D_m$	Magnet surface diameter
$D_{opt}$	Optimal diameter
$D_{sh}$	Shaft diameter
$d_v$	Voltage drop
$E^s$	Back-EMF at steady state
$e_a^s, e_b^s, e_c^s$	Phase back-EMF (Chapter 2)
$E_o$	Rated back-EMF
$f$	Frequency
$f_r$	Rated frequency
$h_1$	Enclosure slot

---

$h_{11}$	Edge height
$h_{12}$	Link height
$h_{ag}$	Physical air gap
$h'_{ag}$	Total air gap
$H_{ag}$	Air gap coercivity
$H_c$	Normal coercivity
$iH_c$	Intrinsic coercivity
$h_{eq}$	Equivalent air gap
$H_{knee}$	Knee coercivity of normal demagnetization curve
$H_m$	Magnet operating coercivity
$h_{ts}$	Slot height
$h_{us}$	Slot useful height
$h_{yr}$	Rotor yoke thickness
$h_{ys}$	Stator yoke thickness
$h_{ys,opt}$	Stator optimal yoke thickness
$i_1, i_2, i_3$	Phase currents (Chapter 4)
$i_a, i_b, i_c$	Phase currents (Chapter 3)
$i_a^s, i_b^s, i_c^s$	Phase currents (Chapter 2)
$i_d, i_q$	$d$ - and $q$ -axis current
$I_{ch}$	Characteristic current
$I_r$	Rated current
$I_s$	Slot current
$J_s$	Maximum current density

---

$K_{avv}$	Winding factor
$K_c$	Slot fill factor
$K_{car}$	Carter's coefficient
$k_{corr}$	Correction factor
$K_{d,1}$	Fundamental distribution factor
$K_{fill}$	Stacking coefficient
$k_{eddy}$	Eddy-currents coefficient
$k_{hys}$	Hysteresis coefficient
$K_{racc}$	Fundamental pitch factor (Chapter 4)
$K_{racc,1}$	Fundamental pitch factor (Chapter 2)
$K_s$	Actual liner current density
$K_{s,max}$	Maximum liner current density
$K_w$	Working factor
$L_a, L_b, L_c$	Phase self-inductances (Chapter 2)
$L_{core}$	Active lenght
$L_d, L_q$	$d$ - and $q$ -axis inductance
$L_{ec}$	End-winding (end-connection) leakage inductance
$L_{ew}$	End-winding length
$L_{ew,ax}$	End-winding axial length
$L_{leak}$	Total leakage inductance
$l_m$	Magnet thickness
$L_m$	Main inductance
$L_{m,1}$	Fundamental main inductance

---

$L_s$	Synchronous inductance
$L_{sl}$	Slot leakage inductance
$L_{ss}$	Phase self-inductance
$L_w$	Winding total length
$L_\sigma$	Air gap leakage inductance
$m$	Number of phases
$M_{ab}, M_{ac}, M_{bc}$	Phase mutual-inductances (Chapter 2)
$N_{cs}$	Number of conductors per slot
$N_{ph}$	Number of turns per phase
$N_{rac}$	Number of slots that reduce the pole pitch
$N_s$	Number of slots
$N_s'$	Number of teeth wound
$p$	Number of poles
$pp$	Number of pole pairs
$P_{cu}$	Winding losses
$p_{eddy}$	Specific eddy-currents losses
$p_{phys}$	Specific hysteresis losses
$p_{ir}$	Specific iron losses
$P_{ir}$	Iron losses
$P_{out}$	Mechanical power
$q$	Number of slots per pole per phase
$R_s$	Stator phase resistance (Chapter 2)
$S$	Slot cross-section mean value

---

$T$	Temperature
$T$	Torque (Chapter 2)
$T_{cogg}$	Cogging Torque
$T_{dim}$	Sizing torque
$T_{fr}$	Friction torque
$T_{max}$	Maximum magnet temperature
$T_{magn}$	Operating magnet temperature
$T_r$	Rated torque
$T_{wdg}$	Winding temperature
$V$	Phase voltage at steady state (Chapter 2)
$v_a^s, v_b^s, v_c^s$	Stator phase voltages (Chapter 2)
$v_d, v_q$	$d$ - and $q$ -axis voltage (Chapter 2)
$V_{cu}$	Total winding volume
$V_{ir}$	Total iron volume
$V_{LL}$	Line-to-line voltage
$V_{max}$	Inverter phase maximum voltage
$V_{mg}$	Magnets volume
$V_r$	Phase voltage (Chapter 3-4)
$V_{teeth}$	Total teeth volume
$V_{tot}$	Total active materials volume
$V_{yr}$	Rotor yoke volume
$V_{ys}$	Stator yoke volume
$W$	Material weight

---

$w_{as}$	Slot average width
$w_{at}$	Tooth average width
$W_{cu}$	Winding total weight
$W_{ir}$	Core total weight
$w_m$	Magnet width
$W_m$	Air gap magnet energy
$w_{max}$	Maximum distance between slots
$W_{mg}$	Total magnets weight
$w_{min}$	Minimum distance between slots
$w_o$	Opening slot
$w_{sb}$	Slot bottom width
$w_{st}$	Slot top width
$w_{tb}$	Tooth bottom width
$W_{tot}$	Total active materials weight
$w_{tt}$	Tooth top width
$X_s$	Synchronous reactance
$Z_{ph}$	Number of conductors per phase

## Greek symbols

$\alpha_B$	Temperature coefficient of remanence
$\alpha_H$	Temperature coefficient of intrinsic coercivity
$\alpha_m$	Magnet pitch (expressed as percentage)
$\beta_c$	Slot angular pitch

---

*Symbols and acronyms*

---

$\beta_{st}$	Steinmez's coefficient
$\gamma_{cu}$	Winding specific weight
$\gamma_{ir}$	Iron specific weight
$\gamma_{mg}$ .	Magnet specific weight
$\delta$	Lamination thickness
$\Delta T$	Delta of temperature
$\varepsilon$	Chording angle
$\eta$	Efficiency
$\theta_m$	Mechanical rotor position
$\theta_{me}$	Electric rotor position
$\lambda$	Aspect ratio
$\lambda_a^s, \lambda_b^s, \lambda_c^s$	Phase fluxes linkage (Chapter 2)
$\lambda_{a,b-c}, \lambda_{b,a-c},$ $\lambda_{c,a-c}$	Phase fluxes linkage due to other currents (Chapter 2)
$\lambda_{a,m}, \lambda_{b,m}, \lambda_{c,m}$	Phase fluxes linkage due to magnet (Chapter 2)
$\lambda_m$	Magnet flux
$\lambda_{m,d}, \lambda_{m,q}$	<i>d</i> - and <i>q</i> -axis magnet flux (Chapter 2)
$\lambda_{min}$	Minimum flux
$\mu_0$	Vacuum permeability
$\mu_r$	Relative recoil permeability
$\rho_{cu}$	Resistivity
$\tau_p$	Polar pitch
$\tau_s$	Slot pitch
$\varphi$	Angle between <i>d-axis</i> and <i>a-axis</i>

---

$\phi_p$	Flux per pole
$\phi_{1p}$	Fundamental flux per pole
$\omega_b$	Base speed
$\omega_{me}$	Electrical speed
$\omega_m$	Mechanical speed
$\omega_{max}$	Maximum electrical speed

## Acronyms

back-EMF	Back ElectroMotive Force
FE	Finite-Element
FEA	Finite-Element Analysis
<i>FEA-t</i>	Finite-Element Analysis tool
FEMs	Finite-Element Method software
FSCW	Fractional-Slot Concentrated Winding
GCD	Greatest common divisor
LCM	Lower common multiple
MMF	MagnetoMotive Force
MPTA	Maximum Torque Per Ampere
MST	Maxwell's Stress Tensor
NdFeB	Neodymium-Iron-Boron
PM	Permanent-Magnet
SMDT	SPM Machine Design Tool
SPM	Surface-Mounted Permanent-Magnets

### *Symbols and acronyms*

# 1 Introduction

## 1.1 Background

The ways electrical machines are designed have changed a lot throughout the years, from more empirical procedures to more analytical methods. Despite of that, it is possible to state that still nowadays designers of rotating electrical machines usually design new motors, or generators, by relying on pre-existing projects and on own experience and by using analytical and Finite-Element Method commercial software (FEMs). These software provide a detailed analyses about the machine magnetic, mechanical and thermal behaviour but, on the other hand, they already need a reasonable preliminary geometry of the electromagnetic structure, the material properties of machine and some windings features as input. Therefore, the uncommon dimensions and very different from the standard requirements force electrical engineers involved in this field starting the design of a new machine from scratch, as the approach based on the use of own data-base collection and the use of tool based on FEMs is inefficient and inadequate. With regard of FEMs, in fact, the main problem is the incompatibility between the necessity to start a design from scratch and their using principle, because, as previously said, these software already need an initial geometry, the slots shape or the number of winding turns to work effectively. In the last years, a lot of algorithms have been implemented and developed to improve and exploit the potential of the FEMs, but their use is still limiting if a designer wants to have a fast evaluation of machine main dimensions and, so, its cost. That due to the long times required by FEMs to analyse, solve and optimize electromagnetic problems.

For these reasons, the Department of Energy of Polytechnic of Turin (DENERG), like many company R&D offices, has been studying and improving a sizing tool simply based on well-known analytical equations able to make the designing faster. By defining some basic

---

specifications, such as the material solicitations and the rated data, the tool can quickly provide the laminations dimensions and the machine main parameters.

It is extremely important to bear in mind how the project output obtained with this tool is not the machine final project, since accurate validation and optimization in terms of electromagnetic, thermal and mechanic performance is required. In this regard, the use of FEMs could be very useful: in fact, already having an accurate preliminary project with dimensions similar to those final, the optimization stage is less time-consuming.

## **1.2 Thesis objective**

Since the first version of the DENERG's tool was developed for induction motors, it has been decided to also adapt it and implement it for Surface-Mounted Permanent-Magnets (SPM) machines. In fact, an increase in use of SPM machines in aeronautical and automotive applications is currently occurring. SPM machines provide high power density and high torque density and, above all, they allow overcoming several encumbrance constraints, as compact machines are obtainable. Moreover, induction machine have additional costs in low speed and high torque applications, due to necessity to be coupled with a gearbox, often expensive. On the contrary, a SPM machine can be directly linked to the shaft, running at low speed and providing high torque. Therefore, the main objectives of this thesis are:

- Create a versatile analytical designing tool for SPM synchronous machines in MATLAB® environment.
- Explain how the tool algorithm works by discussing the equations used.
- Validate the analytical results by means of Finite-Element analyses.

## **1.3 Thesis outline**

The thesis is structured as follows:

- Chapter 2 gives an overview of SPM machines, in terms of construction aspects, operating principle and design guidelines.
  - Chapter 3 presents a description about the design tool and guidelines about how to use it.
  - Chapter 4 describes the algorithm and electromagnetic equations, which the tool is based on.
-

## *I - Introduction*

---

- Chapter 5 presents the design of a SPM machine for aeronautical applications
- Chapter 6 presents the possible future works and concludes the thesis.

## 2 SPM machines: literature review

*In this chapter a literature review on SPM synchronous machines is carried out. In particular, some construction aspects, operating principle and design guidelines are discussed.*

### 2.1 Introduction

SPM synchronous machine is perhaps the most common PM machine on the market, in addition to be the simplest one, too. The main advantage, in fact, is its simplicity of manufacturing that makes them cheapest than other machines in terms of construction. In this type of machine, the magnet material is placed and glued on the rotor surface by using carbon or glass fibre bandage. In the Fig. 2.1, an example of SPM synchronous machine is shown.

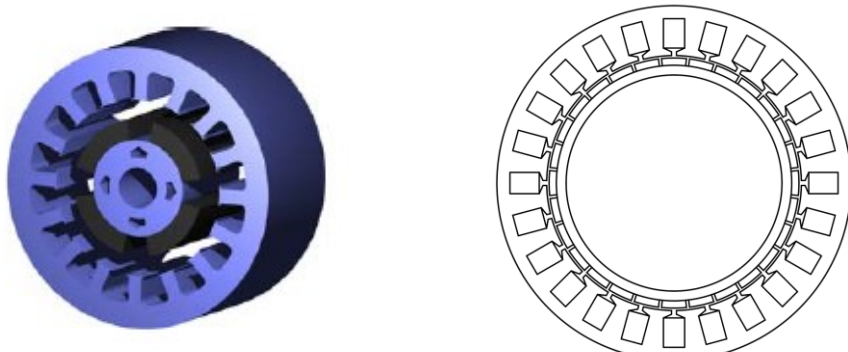


**Figure 2.1:** Example of SPM synchronous machine

Since the PM permeability is almost equal to air permeability,  $d$ - and  $q$ -axis reluctance is the same, resulting in non-salient rotor ( $L_d=L_q$ ). Therefore, the torque is generated by only interaction between stator currents and the magnets.

---

## 2.2 Stator

The stator is usually the same as induction motor. It is made up of a laminated stack and its function is hold the coils. The winding arrangement is usually distributed, however, nowadays SPM machines with Fractional-Slot Concentrated Winding (FSCW) are a good alternative for high performance applications, because of their lower winding losses and higher torque and power density.

### 2.2.1 Stator structure

The stator can be slotted or slotless, as Fig. 2.2 shows. The motors using first stator structure are usually more performing than those using the second one. In fact, motor with slotted stator are characterized by smaller magnetic air gap, which results in higher air gap flux density. The cogging torque and high costs of laying of the winding are the main drawbacks. Instead, slotless stator motors do not have saliency since the reluctance seen by the magnets is the same for any rotor position. Hence, cogging torque is totally eliminated. Moreover, lamination process is simplified.

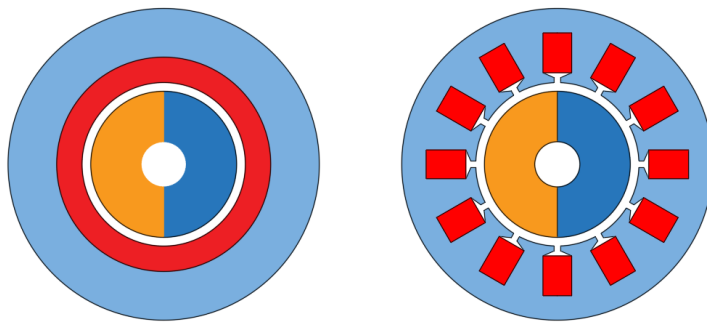


Figure 2.2: Slotless and slotted motor

Slotted stator can have opened, semi-opened or closed slots. The first ones allow to easily lay the winding, but the electrical magnitudes contain many harmonics not fundamental that could be responsible of high torque ripple. In the closed ones, the slots are bridged in proximity of the tooth's head in order to exploit the advantage of an easier laying of the winding as compared with semi-opened slots, but this technology affects the flux linkage by the coils. The bridges, in fact, deviate the flux. As result, decreasing of back-EMF is obtained. Therefore, greater quantity or

---

quality of magnets is needed to have the same back-EMF value, above all in applications where the machine works as generator [1]. For this reason, the first and second one are the most used.

### 2.2.1.1 Influence of stator slots: Carter's coefficient

In case of slotted stator, the presence of slots causes the perturbation of air gap magnetic field, as the air gap above the magnet is not constant, but it is greater in proximity of the opening slot. Here, the flux decreases its density, as shown in Fig. 2.3.

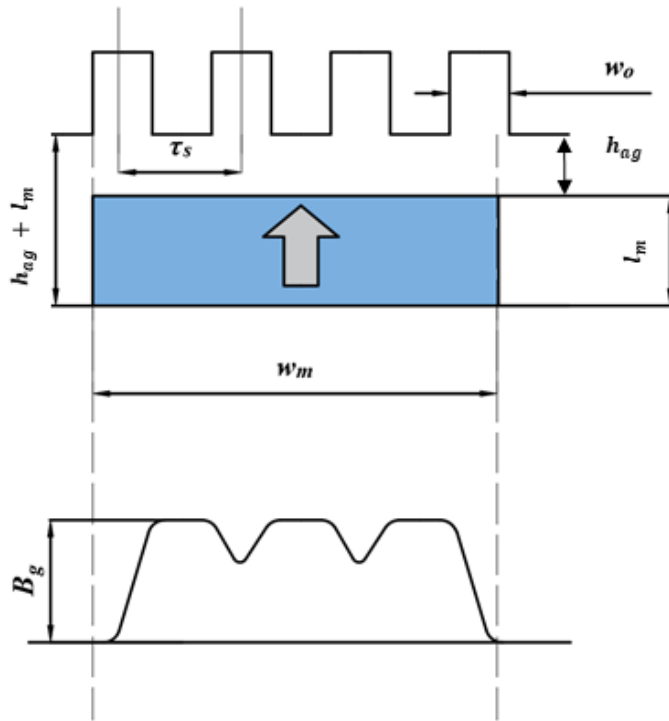


**Figure 2.3:** Air gap flux density under the stator slots

In other words, the magnetic air gap is not equal to the physical air gap, but it is greater according to Carter's principle. Therefore, by assuming a smooth stator, it is possible to take into account of this behaviour by introducing a longer equivalent air gap which is equal to physical air gap corrected by the Carter's coefficient  $K_{car}$ .

Namely,

$$h_{eq} = K_{car} \cdot h_{ag} \quad (2.1)$$

Where:

- $K_{car}$  is a number greater than one.
- $h_{eq}$  is the equivalent air gap.
- $h_{ag}$  is the physical airgap.

In this equivalent air gap, the peak value of fundamental air gap flux density is the same as one in the slotted air gap. The average Carter's coefficient can be computed with the following formula [2]:

$$K_{car} = \frac{\tau_s}{\tau_s - \frac{2}{\pi} \cdot h'_{ag} \cdot (2 \cdot \xi_a \cdot \arctan(\xi_a) - \ln(1 + \xi_a^2))} \quad (2.2)$$

Where  $h'_{ag}$  is the total air gap, which also includes the PM presence, as explained later, and  $\xi_a$  is

$$\xi_a = \frac{w_o}{2 \cdot h'_{ag}} \quad (2.3)$$

Actually, this formulation is valid for cases where the air gap magnetic field is produced by energised windings and not by the PMs. However, it is possible to state that the error committed using the (2.2) is just about 1% [3]. It is possible to use an approximated formula [4] for semi-closed slots.

$$K_{car} = \frac{\tau_s}{\tau_s - h'_{ag} \cdot \frac{4 \cdot \xi_a^2}{5 + 2 \cdot \xi_a}} \quad (2.4)$$

### 2.2.1.2 Slot shape: slot fill factor

The slot can be straight rectangular or trapezoidal, as Fig. 2.4 illustrates. The choice about the slot geometry may depend on target power or torque [4].

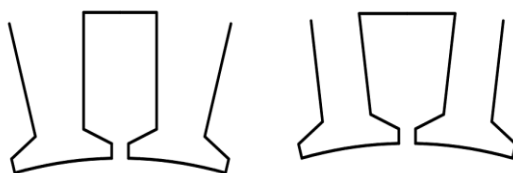


**Figure 2.4:** Rectangular and trapezoidal slot

One fundamental constraints in machine design is the slot fill factor  $K_c$ , which takes into account of influence of the slot shape.

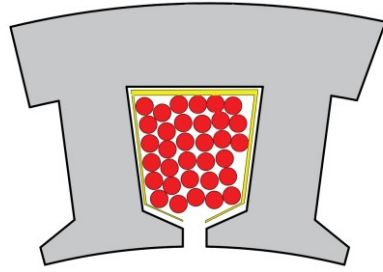


**Figure 2.5:** Cross-section of trapezoidal slot filled by conductors with round cross-section

As can be seen in Fig. 2.5, it is self-evident that is impossible to fill the slot completely as there is air between wires and the slot shape is not uniform. The insulating layer around the wires has an own thickness. Of course, this aspect limits the number of conductors can be placed inside the slot. For this reason, the slot fill factor is here introduced as

$$K_c = \frac{N_{cs} \cdot A_{wire}}{A_{ts}} \quad (2.5)$$

Where:

- $N_{cs}$  is the number of conductors per slot.
- $A_{wire}$  is the area of a conductor.
- $A_{ts}$  is the total slot area.

Furthermore, slot has usually a layer on its inner surface to guarantee insulation between stator core and winding and to avoid superficial damage when coils are placed into the slots. The fill factor can be assume a maximum value of 0.79 for rectangular slot, but its value is not known a priori as it depends on the number of winding turns, the slot shape and the general dimensions. Usually, values of 0.5 or 0.6 easily achieved [1].

## 2.2.2 Winding layout

### 2.2.2.1 Introduction

The most common types of winding used for PM synchronous machines can be divided in two categories [5]:

- Overlapping winding: it can be distributed or concentrated.
- Non-overlapping winding: concentrated, either single layer or double layer.

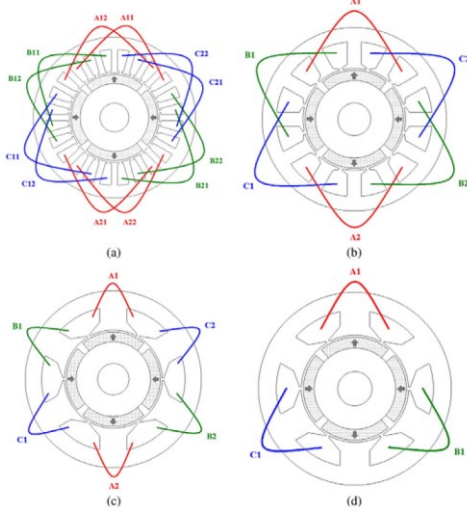


**Figure 2.6:** Types of winding layout: a) overlapping distributed b) overlapping concentrated c) non-overlapping double layer d) non-overlapping single layer [32]

In general, the overlapping distributed winding is the most common one, above all for induction machines, which are very sensitive to the high harmonic content of magneto-motive force (MMF), typical of non-overlapping windings. Instead, with regard of PM synchronous machines, the interest for fractional-slot non-overlapping concentrated winding is quickly increasing for several reasons, as reported in [6].

The number of phases  $m$ , poles  $p$  and stator slots  $N_s$  determine the type of winding by means of the definition of  $q$ , namely the number of the slots per phase per pole, defined as follows:

$$q = \frac{N_s}{m \cdot p} \quad (2.6)$$

Where  $q$  can be a number:

- Integer and greater than one: distributed winding.
- Fractional smaller than one: non-overlapping fractional-slot concentrated winding.
- Equal to one: concentrated winding, as universally accepted [7].

In this thesis, “concentrated winding” and “FSCW” are used as synonymous in order to make it easier to read.

### 2.2.2.2 Distributed winding

As said before, distributed winding has the main advantage to generate a MMF as sinusoidal as larger the number of slots per phase per pole is. Moreover, also the fundamental winding factor  $K_{avv}$ , defined in (2.7), is usually high, obviously choosing  $q$  and  $p$  properly.

$$K_{avv} = K_{racc,1} \cdot K_{d,1} \quad (2.7)$$

$$K_{racc,1} = \cos\left(N_{rac} \cdot \frac{\pi}{6 \cdot q}\right) \quad (2.8)$$

$$K_{d,1} = \frac{\operatorname{sen}\left(\frac{\pi}{6}\right)}{q \cdot \operatorname{sen}\left(\frac{\pi}{6 \cdot q}\right)} \quad (2.9)$$

Where:

- $K_{racc,1}$   $K_{d,1}$  are the fundamental distribution and pitch factor, respectively.
- $N_{rac}$  is the number of slots which reduce the pole pitch.

As will be explained in the Chapter 4, fundamental winding factor is related to the back-EMF amplitude, as well as to the magnetizing inductance: greater is this number, larger is the back-EMF amplitude. However, machines with distributed winding often have long end-windings that means greater winding losses and consequently lower efficiency, higher risk of insulation fails, in addition to higher active length [5]. Furthermore, end-windings do not give any contribution to the induced voltage. For these reasons, concentrated winding represents a good alternative to the distributed winding, above all when the number of poles is high and there are dimensional constraints.

### 2.2.2.3 Fractional – Slot Concentrated Winding

The winding arrangement for concentrated winding can be single layer or double layer, as for distributed winding. The difference is how teeth are wound. In single layer only half of the teeth is wound, on the contrary, all teeth are wound in double layer. Fig. 2.7 shows how the winding is placed in the both cases.



Figure 2.7: Single layer versus double layer [11]

The use of this type of winding gives some advantages that they can be summarized as follows:

- Better field-weakening capability because of higher leakage inductance, in terms of slot leakage inductance and air gap leakage inductance [8].
- Lower cogging torque compared with an equivalent motor with overlapping windings [9].
- Higher slot fill factor above all if the stator is segmented. It results in higher power density [5].
- Shorter end-windings, which means lower winding losses and higher efficiency. This aspect is determining for applications at low frequency where winding losses are predominant compared with iron losses.
- Good fault-tolerant capability. In fact, the windings are not overlapping, hence, the risk of insulation fail is lower, in particular in single layer configuration [5].

Despite of that, motors with FSCW have higher rotor losses due to high harmonic content of MMF, as reported in [8] and [10]. In addition, the machine can be subject of noise and vibrations due to unbalanced magnetic pull, which arises when the radial magnetic forces in the air gap are not regularly distributed [11]. This happens when the winding layout is asymmetric, hence, the pull mostly depends on the choice of number of poles and slots. It is important to avoid solutions with  $X' = 1$ , where  $X'$  is defined as greatest common divisor between the number of poles and slots, namely configurations with  $N_s = p \pm 1$ . The Fig 2.8. shows magnetic forces for different configurations.

---

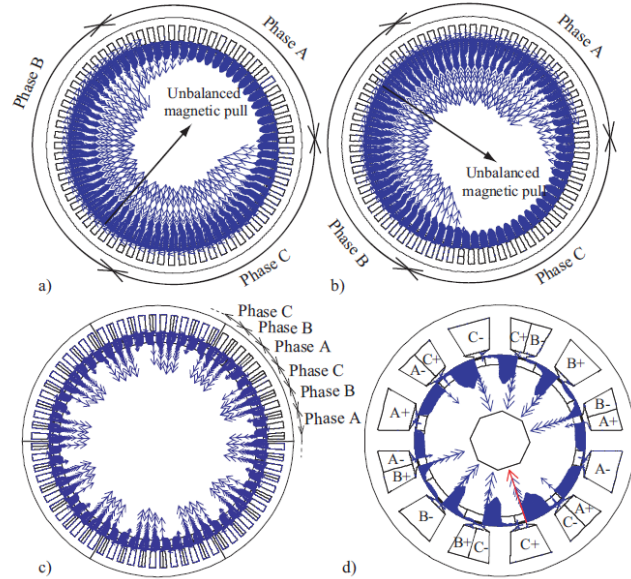


**Figure 2.8:** Magnetic forces with 68 poles and 69 slots a) and b), 60 poles and 72 slots c), 10 poles and 12 slots d). Figure obtained from [11]

### Fundamental winding factor

Equation (2.7) is still valid, but distribution factor and pitch factor must be calculated in different way. A simple method, suitable for both concentrated and FSCW, is reported in [12]. Let's define  $z$  as:

$$z = \frac{N_s'}{\text{GCD}(N_s', p \cdot m)} \quad (2.10)$$

Where:

- $N_s'$  is the number of teeth wound. It is equal to  $N_s$  if all teeth are wound (double layer), otherwise it is equal to  $\frac{N_s}{2}$ , if only half of the teeth are wound (single layer).
- $m$  is the number of phases.
- $\text{GCD}$  stands for greatest common divisor.

Distribution factor and pitch factor can be computed with the (2.11) and (2.12):

$$K_{d,1} = \frac{\sin\left(\frac{\pi}{6}\right)}{z \cdot \sin\left(\frac{\pi}{6 \cdot z}\right)} \quad (2.11)$$

$$K_{racc,1} = \cos\left(\frac{\varepsilon}{2}\right) \quad (2.12)$$

Where  $\varepsilon$  is defined as  $\pi - \frac{\pi}{q \cdot m}$  and it is called *chording angle*. For FSCW, another method is reported in [13]. The table 2.1 reports fundamental winding factor for several poles-slots configurations. Only single layer is studied. As can be noticed  $K_{avv}$  is small for  $q = 0.5$ , whereas grey cells indicate configurations with the highest  $K_{avv}$ . EL-Refai and M. Jahns suggests in [14] that solutions with  $q$  equal to 0.286 and 0.4 are the best candidates when wide speed range of constant-power operation is required in SPM synchronous machines.

**Table 2.1:** Fundamental winding factor for several slots-poles combinations

Poles ( $p$ )	Slots ( $N_s$ )	$q$	$z$	$K_{avv}$
12	18	0,5	1	0,866
16	12	0,25	1	0,866
16	18	0,375	3	0,945
16	24	0,5	1	0,866
16	30	0,625	5	0,711
16	36	0,75	3	0,617
20	18	0,3	3	0,945
20	24	0,4	1	0,966
20	30	0,5	1	0,866
20	36	0,6	3	0,735
20	42	0,7	7	0,650
20	48	0,8	2	0,588
24	18	0,25	1	0,866
24	36	0,5	1	0,866
28	24	0,286	1	0,966
28	30	0,357	5	0,951
28	36	0,429	3	0,902
28	42	0,5	1	0,866
28	48	0,571	2	0,766
32	24	0,25	1	0,866
32	30	0,313	5	0,951
32	36	0,375	3	0,945
32	42	0,438	7	0,890
32	48	0,5	1	0,866
42	36	0,286	1	0,966
40	48	0,4	1	0,966

## 2.3 Rotor

### 2.3.1 Rotor configuration: inner versus outer rotor

The rotor can assume many configurations in base of flux direction, we distinguish axial and radial rotor, direction of rotor motion with respect to axis of flux path, we distinguish longitudinal or transversal rotor, or the position of stator with respect to rotor. Considering only radial longitudinal machines, the rotor can assume the configurations illustrated in Fig. 2.9.

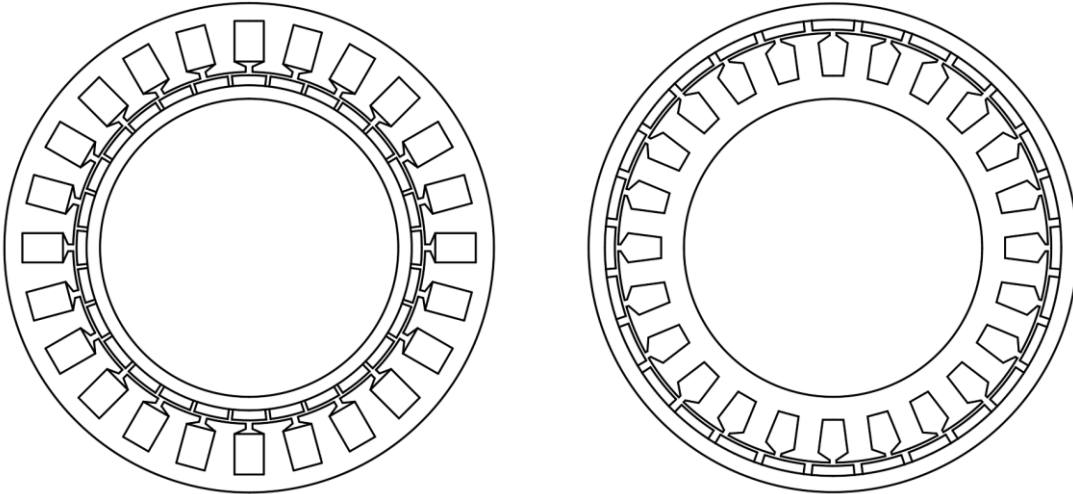


**Figure 2.9:** Inner and outer rotor configuration for 24 slots - 28 poles motor

### Advantages and drawbacks of inner and outer rotor

There are many reasons for which motors with inner rotor are those more common. For instance for an easier heat remove, because the windings are placed externally [1]. In fact, in this kind of machines, the main source of losses is the stator winding. For inner-rotor configuration, the cooling is easier, as is possible refrigerate the motor externally and directly on the surface in contact with the conductors. For outer-rotor configuration, inner cooling is often needed. In this case, the protection carter must have some inlet holes to allow coolant flow from outside to inside. Therefore, in application where the thermal aspect is critic, motor with inner rotor are often preferred.

---

Despite of that, in automotive applications or for wind turbines, outer-rotor motors are quickly spreading since permit to get compact solutions. In addition, for the same external diameter, the air gap diameter  $D_{ag}$  is greater, as Fig. 2.10 shows. Since the torque depends on  $D_{ag}^2 \cdot L_{core}$  product, then motors with outer rotor are shorter, resulting in light solutions in terms of active material weights [11]. In other words, they provide higher torque than inner-rotor motors with the same characteristics of the magnets and active length. Furthermore, external rotors allow an easier winding placement as the slots are upwards.

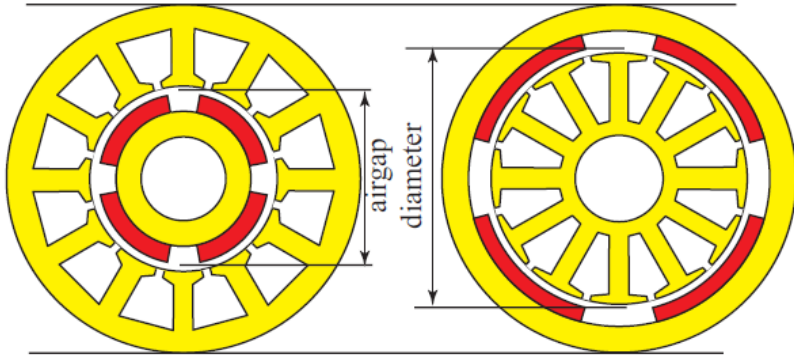


**Figure 2.10:** Airgap diameter for inner and outer rotor with the same external diameter [11]

Lastly, the permanent magnets are exposed to centrifugal forces, as is known. Although this force depends on the distance from the rotation axis and on the speed, outer rotor is the best solution for high speed application of forces because rotor yoke opposes to centrifugal force.

### 2.3.2 Permanent magnets

#### 2.3.2.1 Magnetic parameters and demagnetization curve

In electrical machines, permanent magnets have the function of producing the air gap flux without exciting any winding and they are also defined *hard magnetic materials* due to the wide hysteresis loop [15]. With reference to Fig. 2.11, the most region of interest is the second quadrant. It is possible distinguish two curves: the first one, called *intrinsic demagnetization curve*, describes the produced flux regardless of where the magnet is placed, whereas the second one, called *normal demagnetization curve*, describes the magnet's behaviour within a magnetic circuit [1]. This curve is the one used in motor design.

The demagnetization curve is described by two points:

- Remanence,  $B_r$ , that corresponds to the maximum value of flux density that the magnet can produce or, in other words, it is the flux density to magnetic field zero value.
- Coercive force,  $H_c$ , that is the negative magnetic field amplitude has to apply in order to obtain zero flux density, because  $H_c$  is defined as positive value in material datasheet.

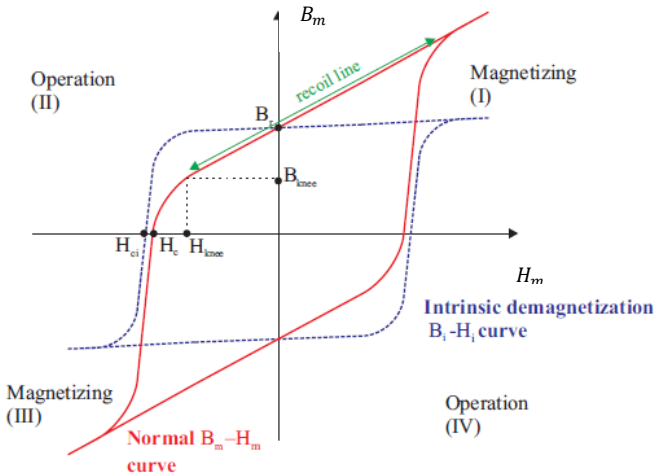


**Figure 2.11:** Permanent magnet hysteresis loop [31]

Materials like ferrite have a knee at low flux density values, whereas the curve is always linear throughout demagnetization curve in the rare-earths materials, as shown in Fig. 2.12. Magnets usually work in the linear zone, or *recoil line*, whose slope is given by the product of relative recoil permeability,  $\mu_r$ , and vacuum permeability  $\mu_0$ . For permanent magnets  $\mu_r$  is usually a value close to unity. In this zone, relation between flux density and coercive force can be approximated with the (2.13).

$$B_m = B_r + \mu_0 \mu_r H_m \quad (2.13)$$

The point  $(H_{knee}, B_{knee})$  defines the operating point limit beyond which the PM is demagnetized and a new and lower recoil line is established [15]. If the operating  $B_m$  is kept higher of  $B_{knee}$ , the magnetizing and demagnetizing are reversible processes, otherwise are irreversible, which means that PM must be magnetized again. Another important parameter is the maximum density product  $(BH)_{max}$ , which gives a measure of performance capability and it is an index of strength of the magnet.

---

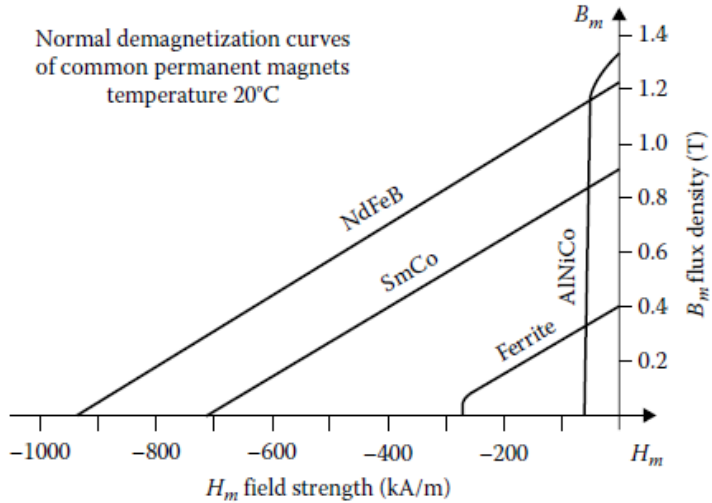


Figure 2.12: Typical demagnetization curves [13]

Performance of permanent magnets depends on the temperature. In fact, for high temperature,  $B_{knee}$  is higher, hence, magnet is easier to demagnetize. Moreover, remanence and coercivity decrease. The temperature effect is taken into account by means of the temperature coefficient of remanence and intrinsic coercivity.

$$B_r(T) = B_r \cdot (1 + \alpha_B \Delta T) \quad (2.14)$$

$$_i H_c(T) = _i H_c \cdot (1 + \alpha_H \Delta T) \quad (2.15)$$

Where  $B_r$  and  $H_c$  are given at room temperature, typically 20 °C and  $\alpha_B$  and  $\alpha_H$  are negative values.

### 2.3.2.2 Permanent-Magnets for SPM machines

Rare-earth materials, such as Samarium-Cobalt (SmCo) and Neodymium-Iron-Boron (NdFeB), are the most used magnets in SPM synchronous machines because of their high performances compared with those of ferrite type [1]. SmCo magnet is able to withstand high operating temperatures, approximately above 300 °C, with good temperature coefficients and a good resistance to corrosion [16]. Therefore, it is one of the most used one, above all in aeronautical application, also because of its excellent resistance to demagnetization. However, the brittle nature of Samarium alloys and high cost often leads to choose NdFeB magnet, since offer a good

price-to-performance ratio, although could be expensive for operating temperature up to 120 °C. In the table 2.2, main properties of rare-earth magnets are reported [17].

**Table 2.2:** Typical properties of rare-earth magnets

	$B_r$ (T)	$H_c$ (kA/m)	Curie $T$ (T)	$T_{max}$ (°C)	Density (kg/m³)	$\alpha_B$ (%/°C)	$\alpha_H$ (%/°C)
SmCo	0.85	570	775	250	8300	-0.04	-0.2
NdFeB	1.15	880	310	180	7450	-0.12	-0.7

### 2.3.2.3 Operating point

Fig. 2.13 shows a magnet inserted in a magnetic circuit, which includes an air gap.

Assuming infinite iron permeability and introducing  $H_m$  and  $H_{ag}$ , namely the PM and air gap magnetic field, respectively, it is possible to write the Ampere's law for the dashed line [13]:

$$H_m \cdot l_m + H_{ag} \cdot h_{ag} = 0 \quad (2.16)$$

Where:

- $h_{ag}$  is the air gap height.
- $l_m$  is the magnet thickness.

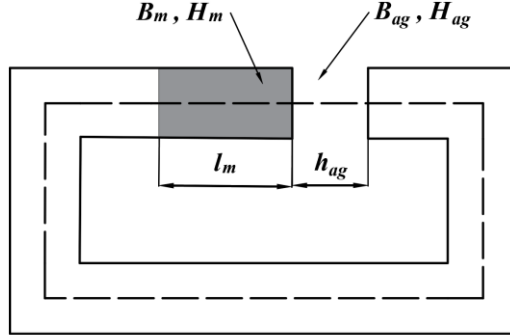


**Figure 2.13:** Magnetic circuit with PM

In addition, if absence of flux leakage is assumed, is also valid the following Gauss's law:

$$\Phi = B_m \cdot A_m = B_{ag} \cdot A_{ag} \quad (2.17)$$

Where:

- $B_m$  and  $B_{ag}$  are the flux densities in the PM and in the air gap, respectively.
- $A_m$  and  $A_{ag}$  are the cross-section areas of PM and air gap.

For the air is valid the following constitutive equation:

$$B_{ag} = \mu_0 \cdot H_{ag} \quad (2.18)$$

By linking (2.16), (2.17) and (2.18), is possible write

$$H_m \cdot l_m + \frac{B_m \cdot A_m}{\mu_0 \cdot A_g} \cdot h_{ag} = 0 \quad (2.19)$$

from which is possible obtain the *load line* equation:

$$B_m = - \left( \mu_0 \cdot \frac{l_m \cdot A_{ag}}{h_{ag} \cdot A_m} \right) \cdot H_m \quad (2.20)$$

The magnet operating point (2.21) can be found by intersecting the load line with the demagnetization curve [18], whose equation has been defined in (2.13).

$$B_m = B_r \cdot \left( \frac{l_m' \cdot \frac{A_{ag}}{A_m}}{h_{ag} + l_m' \cdot \frac{A_{ag}}{A_m}} \right) \quad (2.21)$$

Where  $l_m'$  is calculated as

$$l_m' = \frac{l_m}{\mu_r} \quad (2.22)$$

## 2.4 Electric and magnetic equations

### 2.4.1 Hypothesis

In order to obtain the electric and magnetic model of SPM synchronous machine some hypothesis are needed. In particular is assumed:

- a) Three-phase sinusoidally distributed winding.
- b) Non-salient rotor.
- c) Absence of harmonics in the MMF and magnetic field.
- d) No magnetic saturation.

Moreover, these conventions are taken:

- a) Currents and voltages expressed with the *motor convention*.
- b) Lowercase letter stands for time variable.
- c)  $p$  stands for time derivative (only in this section).

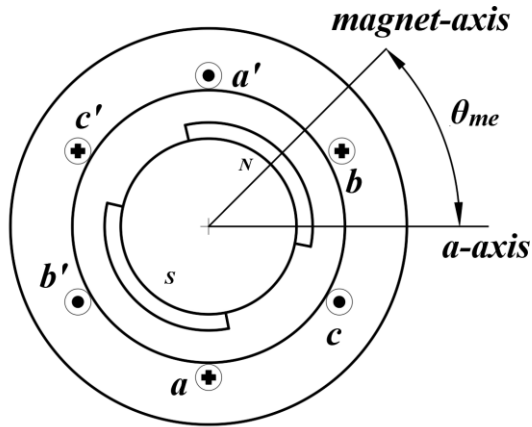


**Figure 2.14:** Windings representation

### 2.4.2 Stator reference frame

The electric model in the stator reference frame is given by the general equations of voltages:

$$v_a^s = R_s i_a^s + p \lambda_a^s$$


---

$$\begin{aligned} v_b^s &= R_s i_b^s + p\lambda_b^s \\ v_c^s &= R_s i_c^s + p\lambda_c^s \end{aligned} \quad (2.23)$$

Where:

- $v_a^s, v_b^s$  and  $v_c^s$  are the stator phase voltages.
- $i_a^s, i_b^s$  and  $i_c^s$  are the stator phase currents.
- $\lambda_a^s, \lambda_b^s$  and  $\lambda_c^s$  are the stator phase fluxes linkage.
- $R_s$  is the phase resistance assumed equal for each phase.

By assuming the absence of hysteresis and eddy currents in the core, it is possible to state that the flux linkage of each phase is equal to the sum of flux linkage due to PM and the one due to other phases:

$$\begin{aligned} \lambda_a^s &= \lambda_{a,b-c} + \lambda_{a,m} \\ \lambda_b^s &= \lambda_{b,a-c} + \lambda_{b,m} \\ \lambda_c^s &= \lambda_{c,a-b} + \lambda_{c,m} \end{aligned} \quad (2.24)$$

Moreover, for the hypothesis a) and d), equal self-inductances and mutual-inductance for each phase can be assumed. Namely,

$$L_a = L_b = L_c = L_{ss} \quad (2.25)$$

$$M_{ab} = M_{ac} = M_{bc} = -\frac{L_{ss}}{2} \quad (2.26)$$

Therefore, the magnetic model can be also written as follows:

$$\begin{aligned} \lambda_a^s &= L_a i_a^s + M_{ab} i_b^s + M_{ac} i_c^s + \lambda_{a,m} = \left( L_{ss} + \frac{L_{ss}}{2} \right) i_a^s + \lambda_{a,m} = L_s i_a^s + \lambda_{a,m} \\ \lambda_b^s &= M_{ba} i_a^s + L_b i_b^s + M_{bc} i_c^s + \lambda_{b,m} = \left( L_{ss} + \frac{L_{ss}}{2} \right) i_b^s + \lambda_{b,m} = L_s i_b^s + \lambda_{b,m} \\ \lambda_c^s &= M_{ca} i_a^s + M_{cb} i_b^s + L_c i_c^s + \lambda_{c,m} = \left( L_{ss} + \frac{L_{ss}}{2} \right) i_c^s + \lambda_{c,m} = L_s i_c^s + \lambda_{c,m} \end{aligned} \quad (2.27)$$

Where:

- $L_s$  is called *synchronous inductance*.
  - Three-phase symmetric system of currents is assumed.
-

- $\lambda_{a,m}$ ,  $\lambda_{b,m}$  and  $\lambda_{c,m}$  are the phase fluxes linkage due to permanent magnet.

As said before, for sake of simplicity, the fluxes leakage due to PM with no current are supposed sinusoidal and they can be expressed with the following equations:

$$\begin{aligned}\lambda_{a,m} &= \lambda_m \cos(\theta_{me}) \\ \lambda_{b,m} &= \lambda_m \cos\left(\theta_{me} - \frac{2\pi}{3}\right) \\ \lambda_{c,m} &= \lambda_m \cos\left(\theta_{me} - \frac{4\pi}{3}\right)\end{aligned}\quad (2.28)$$

Where:

- $\lambda_m$  is the maximum value of flux linkage by the generic phase when magnetic phase and magnet axis are aligned.
- $\theta_{me}$  is the electric rotor position, or in other words, is the offset between the magnetic field of PM and magnetic axis of phase  $a$ , as shown in Fig 2.14, and it is defined as:

$$\theta_{me} = pp\theta_m \quad (2.29)$$

Where  $pp$  is the number of pole pairs and  $\theta_m$  is the mechanical angle between the magnet- and  $a$ -axis.

Substituting equations (2.27) in (2.23), the three-phase voltage balance becomes:

$$\begin{aligned}v_a^s &= R_s i_a^s + L_s p i_a^s + e_a^s \\ v_b^s &= R_s i_b^s + L_s p i_b^s + e_b^s \\ v_c^s &= R_s i_c^s + L_s p i_c^s + e_c^s\end{aligned}\quad (2.30)$$

Where  $e_a^s$ ,  $e_b^s$  and  $e_c^s$  are the back electromotive forces (back-EMF) that can be computed as follows:

$$\begin{aligned}e_a^s &= p\lambda_{a,m} = \lambda_m \omega_{me} \cos\left(\theta_{me} + \frac{\pi}{2}\right) \\ e_b^s &= p\lambda_{b,m} = \lambda_m \omega_{me} \cos\left(\theta_{me} + \frac{\pi}{2} - \frac{2\pi}{3}\right) \\ e_c^s &= p\lambda_{c,m} = \lambda_m \omega_{me} \cos\left(\theta_{me} + \frac{\pi}{2} - \frac{4\pi}{3}\right)\end{aligned}\quad (2.31)$$


---

Where  $\omega_{me}$  is the electrical speed of the PM-axis.

The equations above can be also expressed in a more compact form by using space vectors:

$$\bar{e}^s = j\omega_{me}\bar{\lambda}_m \quad (2.32)$$

Therefore, the electric model results:

$$\bar{v} = R_s \bar{i}^s + L_s p \bar{i}^s + \bar{e}^s \quad (2.33)$$

#### 2.4.2.1 Synchronous reference frame

Another easier way to write the electric and magnetic model is to express the space vector defined in (2.29) in a rotor synchronous reference with its *d-axis* aligned with the magnet-axis and rotating at  $\omega_{me}$  speed, as shown in Fig. 2.15

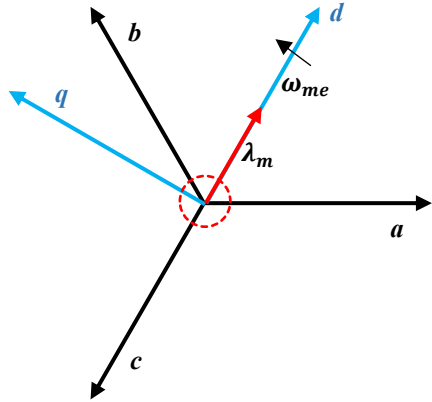


**Figure 2.15:** Synchronous rotor frame

The real and complex component of the space vector result:

$$\begin{aligned} v_d &= R_s i_d + L_d p i_d - \omega_{me} \lambda_q \\ v_q &= R_s i_q + L_q p i_q + \omega_{me} \lambda_d \end{aligned} \quad (2.34)$$

Where  $\lambda_d$  and  $\lambda_q$  are:

$$\begin{aligned} \lambda_d &= L_d i_d + \lambda_{m,d} \\ \lambda_q &= L_q i_q + \lambda_{m,q} \end{aligned} \quad (2.35)$$


---

Thanks to the hypothesis introduced above about rotor synchronous reference:

- $\lambda_{m,d}$ -amplitude is equal to  $\lambda_m$ .
- $\lambda_{m,q}$ -amplitude is zero.

Substituting (2.35) in (2.35), the electric model in  $d$ - $q$  axis can be lastly written:

$$\begin{aligned} v_d &= R_s i_d + L_d p i_d - \omega_{me} L_q i_q \\ v_q &= R_s i_q + L_q p i_q + \omega_{me} L_d i_d + \omega_{me} \lambda_m \end{aligned} \quad (2.36)$$

By means of the electric equations defined in (2.34) is possible to obtain the electromagnetic torque by proceeding with the power balance, obtainable by multiplying voltages  $v_d$  and  $v_q$  per  $i_d$  and  $i_q$ , respectively.

$$(v_d i_d + v_q i_q) = R_s (i_d^2 + i_q^2) + (i_d L_d p i_d + i_q L_q p i_q) + \omega_{me} (\lambda_d i_q - \lambda_q i_d) \quad (2.37)$$

The energy is the sum of

- Total resistance losses.
- Time variance of magnetic energy.
- Mechanical power.

Reminding that the mechanical power can be also written as

$$T = T \omega_m \quad (2.38)$$

Where  $\omega_m$  is equal to  $\omega_m = \frac{\omega_{me}}{pp}$  then, the electromagnetic torque can be compute with the following equation:

$$T = \frac{3}{2} pp (\lambda_d i_q - \lambda_q i_d) \quad (2.39)$$

However, PM machines with isotropic rotor are only supplied with current in  $q$ -axis in order to maximize the torque. Therefore, assuming steady state condition and according with what has been assumed before, the torque can be calculated as follows:

$$T = \frac{3}{2} pp \lambda_m i_q \quad (2.40)$$


---

It is important to remark that the term  $\frac{3}{2}$  has been added to the torque relation in order to maintain the power formalism between a reference to the other one.

## 2.5 Cogging torque

It can be experimentally evidenced the presence of a torque ripple also when the machine's windings are not excited, as shown in Fig. 2.16.

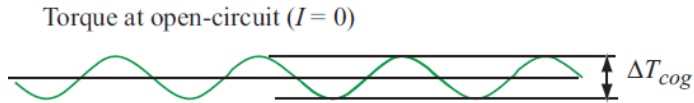


**Figure 2.16:** Cogging torque. Figure extrapolated from [11]

This ripple, also called *cogging torque*, is the result of tendency of the rotor to maximize the permeance of the fringing magnetic fields of the PM [9], or, in other words, it is the result of the variation of the reluctance seen by the PM due to slots presence [11]. To explain the reasons of this torque ripple, let's take as reference the two possible relative equilibrium positions between the full-pitched magnet and the teeth shown in Fig. 2.17.

In particular, it can be:

- Pole pair axis aligned with the center of the tooth.
- Pole pair axis aligned with the center of the slot.

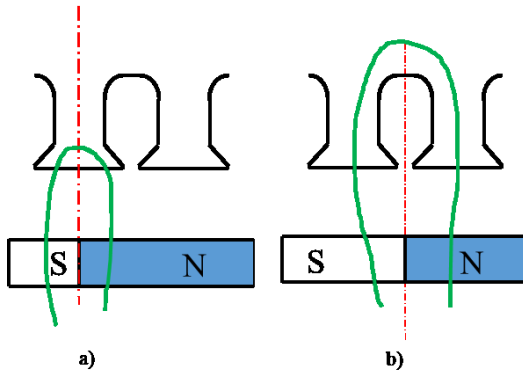


**Figure 2.17:** Equilibrium positions between pole pair axis and tooth

As can be noticed, in the first case, the magnetic field line between the edge of the north and south pole has the minimum length, while in the second one it has the maximum one [9]. Hence, as

deducible, the two situations correspond to two different states of magnetic energy stored in the air gap. Since the torque is produced when variation of the magnetic energy occurs, then

$$T_{cogg} = \frac{dW_m}{d\theta_m} \quad (2.41)$$

Where  $W_m$  is the magnetic energy stored in the air gap, as shown in Fig. 2.19.

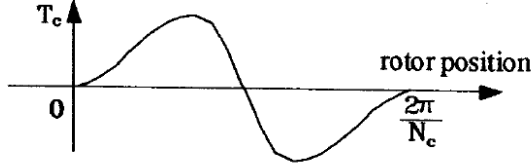


**Figure 2.18:** Typical waveform of the cogging torque ( $N_c$  stands for number of slots) [9]

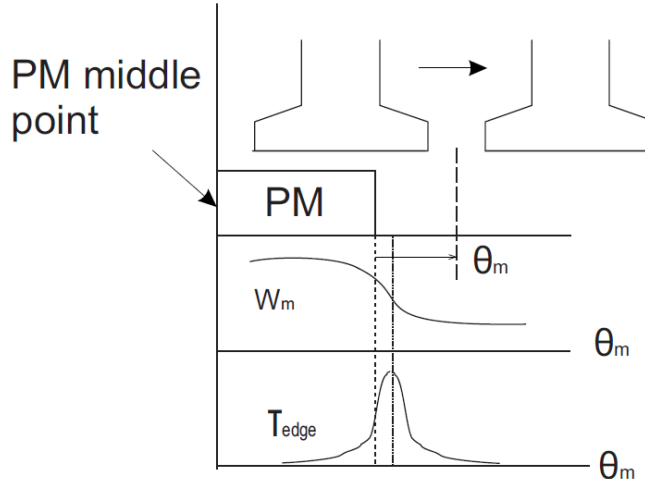


**Figure 2.19:** Magnetic energy stored in the airgap and cogging torque [31]

The number of cogging torque periods along a slot pitch can be written as

$$N_{cog} = \frac{LCM(N_s, p)}{N_s} \quad (2.42)$$

Where  $LCM(N_s, p)$  is the number of cogging torque periods during a machine revolution. Larger is  $LCM(N_s, p)$ , lower is the amplitude of the cogging torque. Hence,  $N_{cog}$  is an important design parameter to perform low cogging torque.

---

The presence of this ripple can be responsible of noise and vibrations or it may create problems to the control system, as well as determine distortion of the speed. Hence, it is needed to limit the cogging torque by accurately choosing some design parameters [9] or by adopting techniques [19] such as:

- Correct choice of the number of poles and slots.
- Skewing or stepping of the stator.
- Shifting of the PMs.
- Selection of an odd number of slots.
- Selection of an even number of PMs.
- Different number of slots and poles.
- Implementation of auxiliary slots.
- Selection of suitable slot opening.

## 2.6 SPM motor drive

### 2.6.1 MPTA

The most used control strategy for SPM motors is the MPTA (*Maximum Torque Per Ampere*) control which provides constant torque by setting the current vector aligned to the *q-axis* and in quadrature to the magnet flux linkage, hence guaranteeing the minimum winding losses.

In this operating condition, the speed, the phase voltage and the power increase until the drive maximum voltage  $V_{max}$  is achieved. The speed achieved at this point is commonly called *base speed*  $\omega_b$  or also *rated speed*.

### 2.6.2 Flux-weakening

For high speed operating conditions, instead, is necessary rotate the current vector in anti-clockwise way in order to decrease the air gap flux and keeping the voltage within the limit of the inverter. Namely, the machine works in field-weakening condition. The trajectories of the current and flux at the rated current during the field-weakening are shown in Fig. 2.20.

An ideal flux-weakening capability is obtainable if

$$\lambda_m = L_s \cdot i_1 \quad (2.43)$$

Where:

- $L_s$  is the synchronous inductance.
- $i_1$  is the rated current, previously called  $I^s$ .

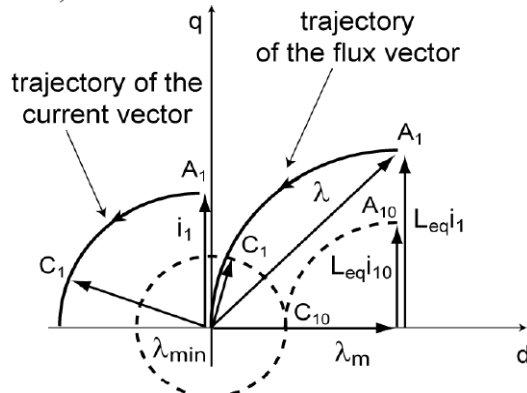


Figure 2.20: Current and flux trajectory [20]

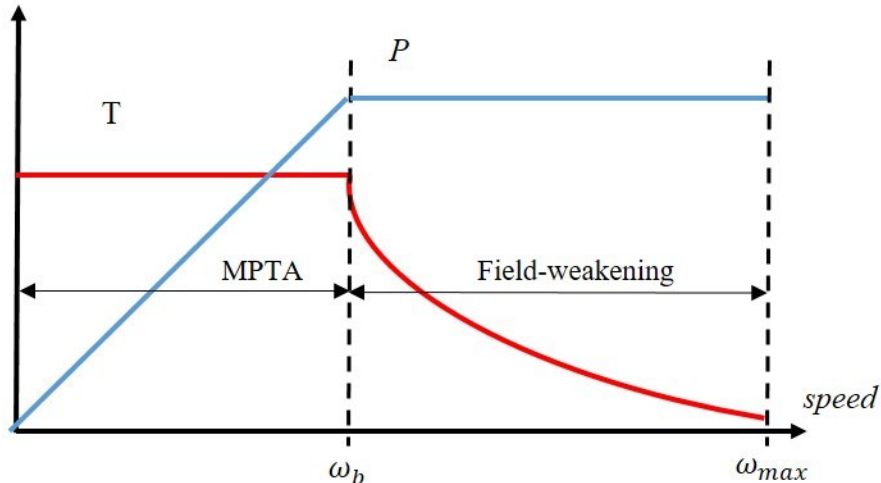


Figure 2.21: Power and torque versus speed curve

In case of optimal field-weakening capability, the torque decreases in inverse proportion to the speed, while the power remains always constant beyond the base speed, as shown in Fig. 2.21. Actually, the power is not constant beyond the base speed in real motors. This aspect can be shown by introducing the *inverter utilization ratio*, namely the ratio between the output power and the power limit, defined as

$$P_{lim} = \frac{3}{2} \cdot V_{max} \cdot i_1 \quad (2.44)$$

In case of optimal flux-weakening capability and operating at the rated current, the power tends asymptotically to the power limit, as can be seen in the Fig. 2.22. This happens because the voltage and current vector tend to be aligned while rotating the current vector, namely the power factor tends to be close to 1. If power losses are neglected, the *inverter utilization ratio* can be also

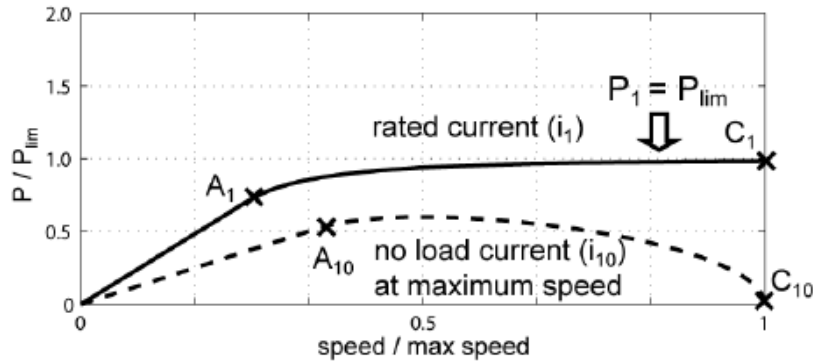


Figure 2.22: Normalized power curve [20]

interpreted as the power factor curve [20]. Therefore, the point A<sub>1</sub> corresponds to the power factor at synchronous speed and it can be calculated as

$$\cos\varphi = \frac{E^s}{V} \quad (2.45)$$

On the contrary, if we are not in the condition of optimal flux-weakening capability, the power tends to be zero, since the voltage and the current vector tend to be in quadrature.

### 2.6.3 Maximum speed

Assuming to be in steady state condition, if the speed is high enough to neglect the resistive voltage drop, then the electric equation expressed as vector is

$$\vec{V} = \vec{E}^s + j \cdot X_s \cdot \vec{I}^s \quad (2.46)$$

Where:

$$E^s = \omega_{me} \cdot \lambda_m \quad (2.47)$$

$$X_s = \omega_{me} \cdot L_s \quad (2.48)$$

Therefore, the maximum speed capability can be calculated as

$$\omega_{max} = \frac{\omega_b \cdot V_{max}}{E^s - X_s \cdot I^s} \quad (2.49)$$

as the phase voltage and the back-EMF vectors are in phase when the current is all supplied in the *d-axis*.

In case of optimal flux-weakening capability, the maximum speed is ideally infinite, on the contrary, if the condition (2.43) is not satisfied the maximum speed has a finite value. Instead, the amplitude of the flux at the maximum speed [20] is equal to:

$$\lambda_{min} = \frac{V_{max}}{\omega_{max}} \quad (2.50)$$

#### 2.6.4 Characteristic current

An index of flux-weakening capability is given by the characteristic current  $I_{ch}$  [14], defined as

$$I_{ch} = \frac{\lambda_m}{L_s} \quad (2.51)$$

The optimal flux-weakening occurs when  $I_{ch}$  is equal to the rated current. However, in SPM machines with distributed winding the characteristic current is often higher than the rated current due to low inductance, as the magnets behave as a large air gap, and high magnet flux linkage that cannot be significantly lowered without decreasing the torque as well [14]. This results in poor flux-weakening capability. For this reason, FSCW are often used when a wider constant power-range is requested. Machine with FSCW, in fact, present an higher leakage inductance due to high content of harmonics in the MMF, as explained in [11], resulting in a better field-weakening capability.

# 3 SMDT: SPM Machine Design Tool

*In this chapter, the tool SMDT will be explained in detail, in particular how the user interfaces are structured and how it can be used to design, simulate and view the obtained results.*

## 3.1 Introduction

The proposed tool for SPM synchronous machines design, called **SMDT (SPM Machine Design Tool)** does not use any particular empirical formulas derived from designer experience or from standard procedures, but there are simply used some classical electromagnetic formulas well known also by beginner designers. Basically, by increasing machines dimensions progressively, in particular diameters and active length, these formulas are looped until the target torque is achieved. Once rotor and stator main dimensions, slots shape and winding features are determined, the tool also calculates the machine main parameters such as the stator resistance, phase inductance, leakage inductance and so on. These parameters are useful to have an idea about the costs of the machine and getting an initial magnetic structure for the FEMs.

At the beginning of design stage, the designer has to define some design specifications, such as dimensional constraints, material stress indexes, the used materials for the core, winding and magnets and other target data. Therefore, it has been decided to also create a graphical interface (GUI) in order to provide a fast and easy handling of input and output data. The tool has been developed in MATLAB® environment. A comprehensive guide about creating GUI with MATLAB® can be found in [21].

The tool is structured in two user interfaces: the first one is dedicated to input data, whereas the second one is dedicated to results visualization and FEM simulations.

---

## 3.2 Input user interface

As shown in Fig.3.1, the first window is divided in different panels, each one called with a name related to the kind of property, parameter or data that the designer should enter manually or let tool calculates, as later explained. As can be noticed the window is made up of different types of user controls: editable cells, with which the designer can introduce the value of some parameters, push-buttons to execute commands, check-buttons to activate or disable functions or pop-up menus that allow choosing among different options.

The panels and their basic functions are briefly introduced in the following list:

- **Rated data:** the user can enter the nominal values for the motor, such as the rated voltage, rated frequency, rated torque.
- **Stress indexes:** this panel is dedicated to specification of the material solicitations, such as flux density, current density and linear current density.
- **Geometry:** this panel allows to specify the general geometry properties of the motor and the slot dimensional constraints, such as the shape and enclosure dimensions
- **Winding:** the user decides the type of winding and its main properties like the number of phases, working temperature and so on.
- **Materials:** the designer is free to select the materials for the magnets, winding and the core, as well as specify dimensional properties, for example the magnet thickness.  
The core material can be chosen from the default library or it can be loaded, and once the flux densities are fixed, it is also possible visualize the magnetic field and flux density distribution.
- **Core properties:** this panel shows the average magnetic field and specific losses in the rotor and stator core and teeth taking into account of flux density imposed and materials chosen.

**SMDT (SPM MACHINE DESIGN TOOL)**

POLITECNICO DI TORINO

**GEOMETRY**

**GENERAL PROPERTIES**

- Airgap height: 0 mm
- Shaft diameter: 0 mm
- Ratio L/D: 0
- Type of rotor: Internal
- Slot opening: 0 mm
- Link height: 0 mm
- Edge height: 0 mm
- Filling coeff.: 0
- Friction Torques in %: 0 %
- Voltage drop in %: 0 %
- Cos φ: 0
- Rated power: 0 kW

**RATED DATA**

- Phase rate voltage: 0 V
- Rated torque: 0 Nm
- Rated frequency: 0 Hz
- N. poles: 0
- Rated power: 0 kW

**SLOTS**

- Slot type: Rectan..
- Number of phases: 3
- Wind. Temp.: 0 °C

**CARTER COEFFICIENT**

- Wind. Temp.: 0 °C

**CORE**

- Conductor material: Cu
- Electr. Conductivity: 0 Ms/m

**WINDING**

- Magnet height: 0 mm
- % magnet pitch: 0
- Specific weight: 0 kg/m<sup>3</sup>
- Br @ working temp.: 0 T
- Hc @ 20°: 0 A/m
- Working T [°C]: 0 °C
- Temp.Coeff.of Br: 0 %/°C
- μr: 0

**PROJECT**

- Import material:
- Select material:

**ROTOR**

- Teeth magn. field: 0 A/m
- Yoke magn. field: 0 A/m
- Magnetic shaft:  Yes

**RESET**

- Yoke spec. losses: 0 W/kg
- Yoke magn. field: 0 A/m
- Yoke spec. losses: 0 W/kg
- Yoke magn. field: 0 A/m

**STRESS INDEXES**

- Teeth spec. losses: 0 W/kg
- Yoke spec. losses: 0 W/kg
- Yoke magn. field: 0 A/m
- Yoke spec. losses: 0 W/kg

**GEOMETRY**

**MATERIALS**

**MAGNET**

**CORE**

**WINDING**

**PROJECT**

**ROTOR**

**RESET**

**STRESS INDEXES**

**GEOMETRY**

**MATERIALS**

**MAGNET**

**CORE**

**WINDING**

**PROJECT**

**ROTOR**

**RESET**

**STRESS INDEXES**

Figure 3.1: GUI for design specification and materials

### 3.2.1 Rated data

----- RATED DATA -----		
Phase rate voltage	0	V
Rated torque	0	Nm
Rated frequency	0	Hz
N. poles	0	-
Cos $\Phi$	0	-
Voltage drop in %	0	%
Friction Torque in %	0	%
Rated power	0	kW

Figure 3.2: Rated data panel

With reference to Fig. 3.2, the rated data to enter are the following:

- The rated voltage  $V_r$ , that corresponds to the rms-value of phase voltage and it is useful to calculate the number of conductors in series per phase. Defined  $V_{LL}$  as line-to-line voltage,  $V_r$  is equal to  $V_r = V_{LL} \cdot \frac{1}{\sqrt{3}}$ .
- The target rated torque  $T_r$ , which is the most important parameter since it is the target of the project.
- Number of poles  $p$  and rated frequency  $f_r$ . Their values are chosen in base of the mechanical rated speed and solution that is to be reached in terms of size. For instance, compact solutions are usually preferred in automotive and aeronautical field. This means having a number of poles high enough to guarantee a thin stator and rotor yoke. However, the disadvantage of a high  $p$  is the reduction of magnetising inductance and a consequentially field-weakening capability decrease, whereas the advantage is length reduction of end-windings [1]. The information of number of poles and frequency is also important to estimate the iron losses.
- Friction torque  $T_{fr}$  is defined as a percentage of the rated torque and represents the torque caused by frictional force. It has to be taken into account in the design stage because rated torque can be different from target torque.
- Power factor  $\cos\varphi$ , voltage drop  $d_v$  and rated power, actually, are not input data but are computed afterwards. They have been placed in the input user interface just in order to have all rated data in the same panel.

### 3.2.2 Stress indexes

The stress indexes have to be defined at the beginning are:

- Maximum teeth flux density,  $B_{ts,max}$ .
- Maximum stator yoke flux density,  $B_{ys,max}$ .
- Maximum rotor yoke flux density,  $B_{yr,max}$ .
- Rms current density,  $J_s$ .
- $K_{s,max} \cdot J_s$ .

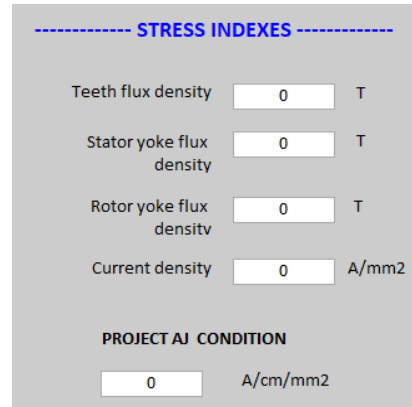


**Figure 3.3: Stress indexes panel**

The values of these parameters determine the project output and the motor performances. It is possible to state that there is not just one possible choice of these parameters, but obviously some choices lead to better solutions than others, for example in terms of thermal behaviour. The selection usually depends on designer's experience and they are strictly related to the cooling and insulation technology, but general guidelines can be found in literature [4], [22]. In fact, there are empirical variation range that can be used in the first steps of designing. Fig. 3.4 shows some recommended values of flux density in different zones of well-designed machines.

In our case, namely SPM machines, it is possible to take as reference the lower values of the ranges reported in the columns regarding non-salient synchronous machines. From the economic point of view, for example, a good choice for the air gap flux density may be about the half of magnet remanence, usually close to 0.5-0.6 T [22].

The same things can be said for the current density and linear current density. The Fig. 3.5 reports some recommended values. Instead of imposing the linear current density, the tool allows to impose the product between linear current density and current density.

	Flux density $B/T$			
	Asynchronous machines	Salient-pole synchronous machines	Nonsalient-pole synchronous machines	DC machines
Air gap	0.7–0.90 ( $\hat{B}_{\delta 1}$ )	0.85–1.05 ( $\hat{B}_{\delta 1}$ )	0.8–1.05 ( $\hat{B}_{\delta 1}$ )	0.6–1.1 ( $B_{\max}$ )
Stator yoke	1.4–1.7 (2)	1.0–1.5	1.1–1.5	1.1–1.5
Tooth (apparent maximum value)	1.4–2.1 (stator) 1.5–2.2 (rotor)	1.6–2.0	1.5–2.0	(compensating winding) 1.8–2.2 (armature winding)
Rotor yoke	1–1.6 (1.9)	1.0–1.5	1.3–1.6	1.0–1.5
Pole core	—	1.3–1.8	1.1–1.7	1.2–1.7
Commutating poles	—	—	—	1.3

Figure 3.4: Recommended design flux densities [22]

	Asynchronous machines	Sailent-pole synchronous machines or PMSMs	Nonsalient-pole synchronous machines			DC machines
			Indirect cooling		Direct water cooling	
$A/kA/m$	30–65	35–65	30–80	90–110	150–200	25–65
$J/A/mm^2$	Stator winding 3–8	Armature winding 4–6.5	Air 3–5	Hydrogen 4–6	Armature winding 7–10	Armature winding 4–9
$J/A/mm^2$	Copper rotor winding 3–8	Field winding: 2–3.5				Pole winding 2–5.5
$J/A/mm^2$	Aluminium rotor winding 3–6.5	Multi-layer 2–4	Field winding 3–5	3–5	6–12	Compensating winding 3–4
		Single-layer	With direct water cooling, in field windings $13–18 A/mm^2$ and $250–300 kA/m$ can be reached			

Figure 3.5: Recommended values for current density and linear current density [22]

### 3.2.3 Geometry

With this panel is possible to define the most important dimensional constraints, such as:

- Shaft diameter,  $D_{sh}$ .
- Air gap height,  $h_{ag}$ .
- Aspect ratio,  $\lambda$ .
- Slot shape: rectangular or trapezoidal.
- Enclosure dimensions,  $w_o$ ,  $h_{11}$ ,  $h_{12}$ .
- Slot fill factor,  $K_c$ .

With regard to the air gap height selection, unlike the induction motors (IM) there are fewer limits. Air gap height,  $h_{ag}$ , depends on the rated power, but usually it is reasonable keeping air gap height as low as possible in order to limit magnetization current.

Since in SPM machines the magnetization is entrusted to PMs, the choice is freer. The chosen is usually within a range of 1-3 mm [1]. However, a large air gap could lead a decrease of magnetising inductance that means a decrease of field-weakening capability, in addition to the needed of more magnetic material to have the same flux density in the air gap, resulting in higher costs. Therefore, keeping the air gap height as small as possible for high speed applications is recommended, although is less constrained than induction machines.

The aspect ratio  $\lambda$  is defined as the ratio between the active core length and air gap diameter.

$$\lambda = \frac{L_{core}}{D_{ag}} \quad (3.1)$$

The choice about it means selecting the shape of the motor: disc-shaped or barrel-shaped. In automotive or aeronautical applications,  $\lambda$  is usually imposed lower than zero to obtain compact solutions, often required in these fields. The choice of  $\lambda$  also determines the back-EMF, as it is directly proportional to the coil area. However, the choice can depend on factors such as the cooling method, space available or performance requirements [23]. The designer has to choose the slot fill factor  $K_c$  and slot shape. It can be trapezoidal or straight rectangular (rounded slots are not introduced in this version of the tool). The slot geometry can be depend on motor power

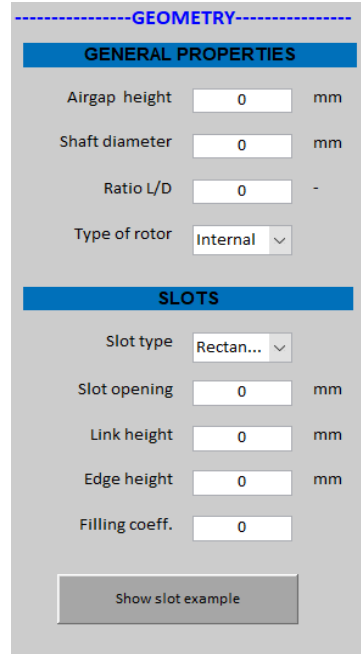
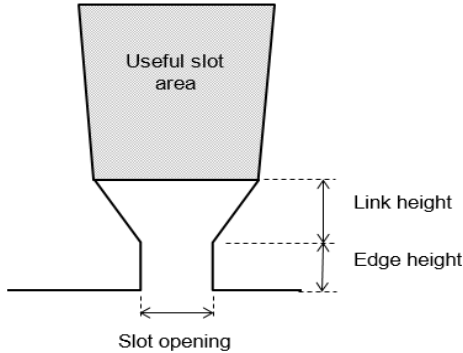


Figure 3.6: Geometry panel



**Figure 3.7:** Slot example

or torque. Secondly, it is necessary to impose some preliminary enclosure dimensions. With reference to Fig. 3.7, the slot opening  $w_o$ , the edge height  $h_{11}$  and link height  $h_{12}$  have to be defined, where  $h_1 = h_{11} + h_{12}$ . The values are freely imposed, but they should be verified and tested with a subsequent Finite-Element analysis.

### 3.2.4 Winding

With this panel is possible to define the type of the winding and set some parameters:

- Type of winding: distributed or concentrated.
- Number of slots per pole per phase,  $q$ .
- Number of slots that reduce the polar pitch,  $N_{rac}$ .
- Winding temperature,  $T_{wdg}$ .
- Carter's coefficient,  $K_{car}$ .

In case of distributed winding is also possible building the winding with a double layer and setting the number of slots

$N_{rac}$  that reduce the polar pitch. With reference to Fig. 3.9,  $n_r$  stands for  $N_{rac}$  and *passo polare* stands for polar pitch. In addition, also it is important to define the winding operating temperature that it is taken into account for the conductor resistivity evaluation. Carter's coefficient has to be assumed, but it can be analytically evaluated at the end of the designing with the (2.4). In this version of the tool only three-phase winding is regarded, for this reason the cell *Number of phase* is not editable.

**Figure 3.8:** Winding panel

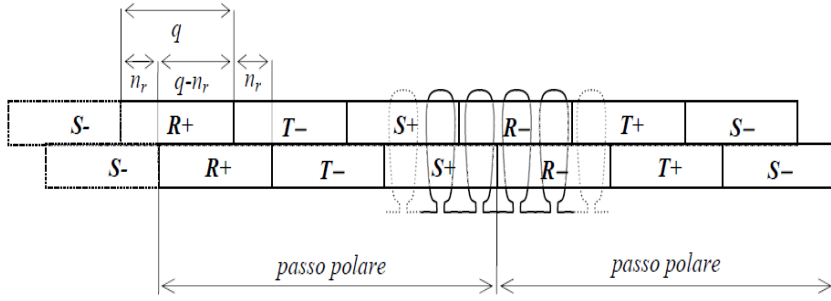


**Figure 3.9:** Example of winding with double layer

### 3.2.5 Materials

This panel is used for setting the material used. With regard to permanent magnet, it is possible to choose among rare earth materials (NdFeB, SmCo) from FEMM's database or to set manually each important parameter for designing and simulating, such as:

- Magnet height (or thickness),  $l_m$ .
- Magnet pitch (expressed as percentage),  $\alpha_m$ .
- Magnet specific weight,  $\gamma_{mg}$ .
- Remanence at the working temperature,  $B_r$ .

Since is assumed to work only in the linear zone of the normal demagnetization curve, namely on the recoil line,  $B_r$  and  $H_c$  reported in the panel are assumed as the limit points of a straight line. By setting the temperature coefficient of remanence (with sign) and the magnet working temperature, the remanence is calculated with the (2.14) and the coercivity at the working temperature is derived. Actually, the coercivity could be different than one calculated in this way, since at high temperature also rare earth magnets present a knee, but for the reason above this aspect is neglected. With regard to core material, it is possible to import the material from .mat file in table form with size of 24x3, or, alternatively, select a material from tool's database. In addition, it is possible to specify if the shaft is magnetic and define the stacking factor  $K_{fill}$  in order to take into account of insulation thickness between laminations. The table on the left reports the magnetic field and the specific losses for different values of flux density, whereas the second one on the right reports the flux density and the magnetic field in the yokes, along 90 electrical degrees.

**MATERIALS**

**MAGNET**

Select from FEMM database   Insert manually

Magnet height	<input type="text" value="0"/>	mm	Br @20°	<input type="text" value="0"/>	T
% magnet pitch	<input type="text" value="0"/>	-	Hc @20°	<input type="text" value="0"/>	A/m
Specific weight	<input type="text" value="0"/>	kg/m <sup>3</sup>	Working T (°C)	<input type="text" value="0"/>	°C
Br @working temp.	<input type="text" value="0"/>	T	Temp.Coeff.of Br	<input type="text" value="0"/>	%/°C
Hc @working temp.	<input type="text" value="0"/>	A/m	μr	<input type="text" value="0"/>	-
Electr. Conductivity	<input type="text" value="0"/>	MS/m			

**WINDING**

Conductor material

**CORE**

Import material   Select material Lamination filling factor

Magnetic shaft  Yes

**Magnetic field - Flux density distribution**

	[B]	[H]	[W/kg]				
1							
2							
3							
4							
5							
6							
7							
8							

	Alfa	BGS(alfa)	BGR(alfa)	HGS(a)
1				
2				
3				
4				
5				
6				
7				
8				

Figure 3.10: Materials panel

### 3.2.6 Core properties and push buttons

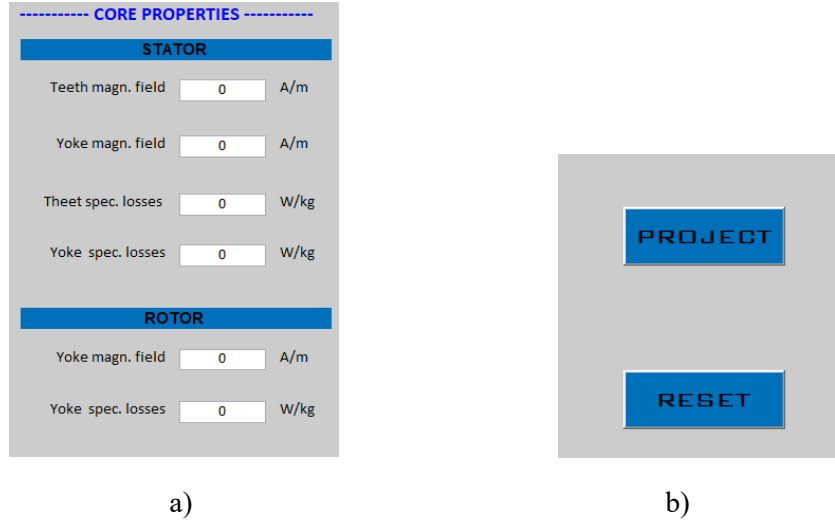


**Figure 3.11:** a) Core properties panel b) Project/Reset buttons

The panel *Core properties*, shown in the Fig. 3.11.a, reports the mean values of the magnetic field in the teeth and yokes and the specific losses calculated by interpolating the stress indexes imposed and the third column of the table on the left.

The tool also has two buttons, shown in Fig. 3.11.b:

- **Project:** this button calls the “Project” function, where the source code of the sizing algorithm is written.
- **Reset:** this button resets all parameters and functions of the input user interface when designer wants to start a new project.

## 3.3 Output user interface

The output user interface, illustrated in Fig. 3.12, shows all parameters calculated with the tool. It is composed only of editable cells where the results are loaded. In addition, the menu bar present two buttons:

- **File:** with this option is possible saving the results as *.xls* or *.mat* file.
- **Open FEMM simulation tool:** it allows to open *FEA-t* (*Finite-Element Analysis tool*) dedicated to FEM simulations, as Fig. 3.13 shows.

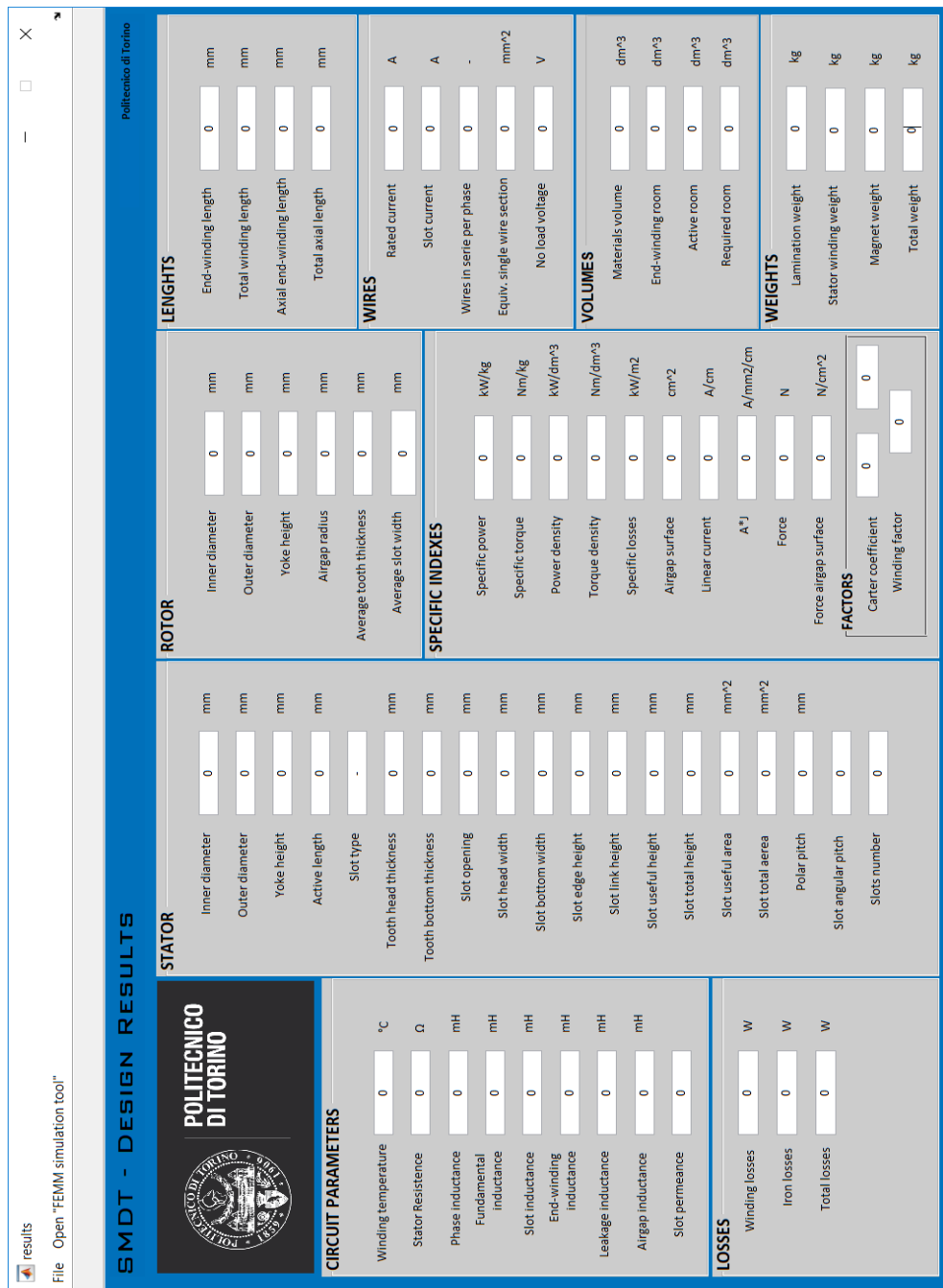


Figure 3.12: GUI for the results visualization

## 3.4 Finite-element Analysis tool

### 3.4.1 Introduction

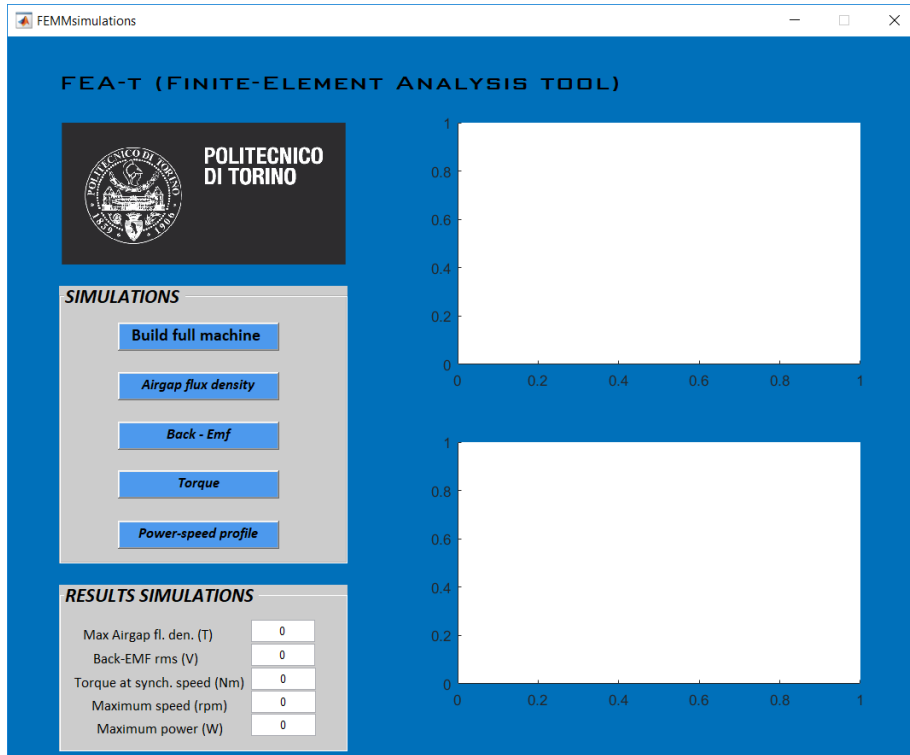


Figure 3.13: GUI for FE analysis

The tool proposed also provides the possibility to validate the project output by doing an in-depth electromagnetic analysis by means of FEMM. FEMM is a Finite-Element method software able to solve electromagnetic and electrostatic problems at low frequency, but, unlike other same-kind software, such as CEDRAT Flux®, does not have any model of motors stored in its database. Hence, the drawing is made from scratch by using Octave FEMM [24], a MATLAB® toolbox that allows for working with FEMM through additional MATLAB® functions useful to accomplish modelling and analysing tasks.

In particular, the evaluation of the analytically-obtained machine is made by means of an own-developed program, embedded in the tool, which allows to automatically draw the machine in FEMM environment starting from obtained geometry dimensions. Furthermore, the program also sets the materials on the basis of those previously selected by the designer, as well as permitting

to analyse the machine's behaviour in terms of air gap flux density, back-EMF at no-load, torque at the synchronous speed and power in state of field-weakening.

### 3.4.2 Machine geometry and materials set up

With reference to 3.13, the program *FEA-t* permits to do Finite-Element analysis, as also said before. It is made up of five buttons, editable cells and two windows where the results are shown. The buttons are:

- Build full machine.
- Air gap flux density.
- Back-EMF.
- Torque.
- Power-speed profile.

Each button refers to the type of action the designer is intentioned to take.

The first button permits to only draw the analytically-obtained machine, without perform any Finite-Element analysis. In particular, the *FEA-t* draws a slot and a magnet and they are copied  $N_s$  and  $p$  times, respectively. It has been decided to draw the full machine, instead of only one pole, in order to allow the designer to evaluate the magnetic field in different points of the machine as he prefers. Fig. 3.14 shows examples of a FEMM drawing of a motor with outer and inner rotor.

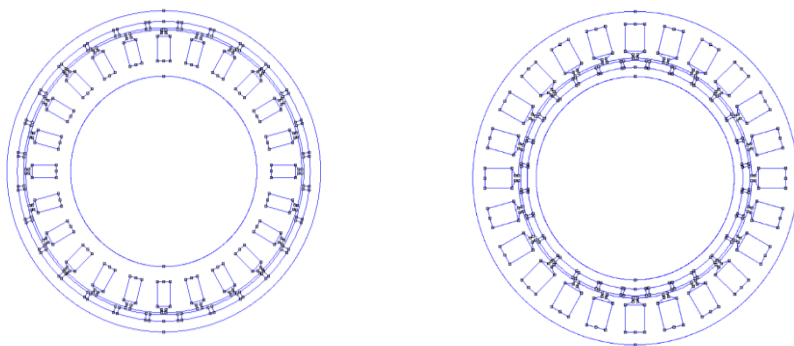


**Figure 3.14:** Outer-rotor motor and inner-rotor motor in FEMM

Materials are created from scratch on basis of the parameters defined in the input user interface and they are successively stored into FEMM library. *FEA-t* also takes into account of field direction for the magnets, B-H curve for the core and the winding layout. In particular, for

distributed winding is used the well-known layout  $A\bar{C}B$ , as illustrated in the Fig. 3.15, taking into account of  $q$  slots per pole per phase. On the contrary, the layout must be defined a priori for the FSCW, since it is difficult creating an algorithm able to directly lay the winding out, because of the large number of options can be implemented to maximize the value of winding factor. In addition, the winding arrangement is really different from those more conventional. The designer is hence invited to define the layout as he likes before proceeding with FEMM modelling.

In this version of *FEA-t*, only single layer technology can be modelled for distributed winding and FSCW, as modelling of more complicated solutions goes beyond the purpose of this thesis. As last step, the boundary conditions are set up. When one of the other buttons is clicked, FEMM starts to process the magnetic problem by using Maxwell's equations in order to obtain the magnetic field distribution within the machine's domain.

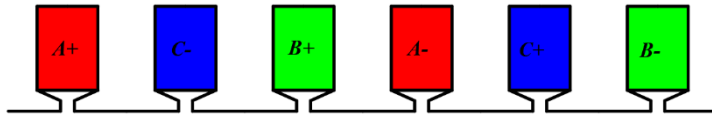


**Figure 3.15:** Distributed winding layout

### 3.4.3 Air gap flux density

Air gap flux density is evaluated along the entire mechanical angle and along one pole pair by set a line contour at mid-height of the air gap. The analysis's purpose is, above all, ensures that the peak value of air gap flux density obtained with FEMM is as close as possible to  $B_g$  calculated with the (4.1) by the tool, as afterwards described. Furthermore, it is useful to show the slots presence effect on the air gap flux density waveform.

### 3.4.4 Back-EMF

The back-EMF rms-value is obtained by progressively rotating the machine by a determined angle and by producing multiple field solutions, since FEMM is only able to solve static problems.

Considering just one phase, for example the phase A, the algorithm computes the flux linkage with this phase by following this procedure:

- Solving and analysing the problem.

- Selection of the slots filled with the phase A+ and calculation of magnetic vector integral  $A_{a+}$ .
- Selection of the slots filled with the phase A- and calculation of magnetic vector integral  $A_{a-}$ .
- Calculation of one-phase flux linkage as

$$\Lambda = N_{ph} \cdot \frac{A_{a+} - A_{a-}}{S} \quad (3.2)$$

Where  $S$  is the slot cross-section mean value multiplied for the number of slot filled with the phase A+ (or A-) and  $N_{ph}$  is the number of turns per phase.

- Rotation of the rotor and repetition of previous steps until a pole pair is covered.

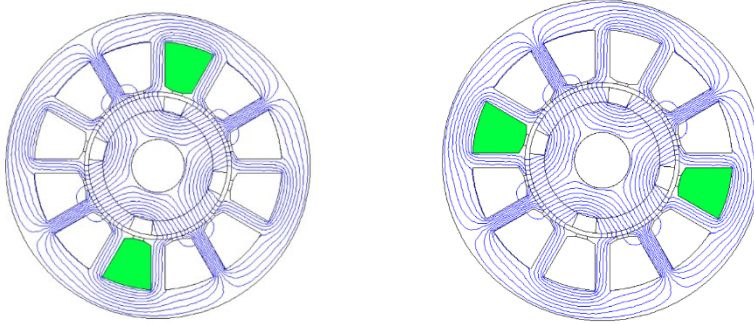


**Figure 3.16:** Selection of the slots

To evaluate the induced voltage  $E_o$  is necessary derive the temporal variation of flux linkage with respect of time.

$$E_o = - \frac{d\Lambda}{dt} \quad (3.3)$$

The relation (3.3) can be also written as

$$E_o = - \frac{d\Lambda}{d\theta_{me}} \cdot \frac{d\theta_{me}}{dt} = - \frac{d\Lambda}{d\theta_{me}} \cdot \omega_{me} = - \frac{d\Lambda}{d\theta_{me}} \cdot pp \cdot \omega_m \quad (3.4)$$

Where:

- $\omega_{me}$  and  $\omega_m$  are the electrical and the mechanical speed expressed in rad/s, respectively.
- $pp$  is the number of pole pairs.

By assuming constant speed, once the derivative of flux linkage is obtained, back-EMF can be simply evaluated by multiplying it for the mechanical speed. In the proposed algorithm, the rated mechanical speed is used as reference and it is calculated as

$$\omega_m = \omega_{m,r} = \frac{2 \cdot \pi \cdot f_r}{pp} \quad (3.5)$$

### 3.4.5 Torque

The calculation of the torque has to be intended as the torque at the synchronous speed. It is evaluated by simulating the machine's behaviour in rated working operation, namely by rotating the current vector in synchronous way with the rotor position and feeding the machine according to the axis in quadrature. The first thing to be done is to line up the rotor with the axle of the phase A, as shown in Fig. 3.17.

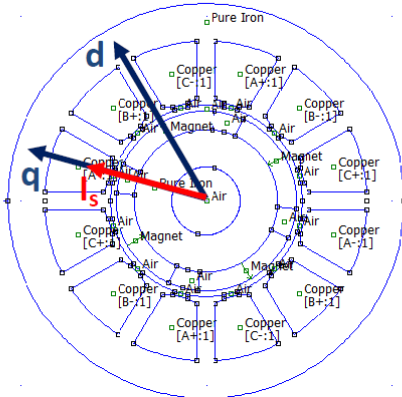


**Figure 3.17:** Alignment of the rotor with the phase A

Since the current along the *d-axis* does not produce contributions of torque in this type of machine, the current is assigned along the axle in quadrature. Namely, with reference to Fig. 3.18 and the system of currents (3.6) and (3.7),  $\varphi = \pi/2$  is imposed for each current's phase.

$$i_a(t) = \hat{I} \cdot \cos(\omega_{me}t + \varphi) \\ \text{Anti-clockwise} \quad i_b(t) = \hat{I} \cdot \cos\left(\omega_{me}t + \varphi - \frac{2\pi}{3}\right) \quad (3.6)$$


---

$$i_c(t) = \hat{I} \cdot \cos\left(\omega_{me}t + \varphi - \frac{4\pi}{3}\right)$$

**Clockwise**

$$i_a(t) = \hat{I} \cdot \cos(\omega_{me}t + \varphi)$$

$$i_b(t) = \hat{I} \cdot \cos\left(\omega_{me}t + \varphi + \frac{2\pi}{3}\right) \quad (3.7)$$

$$i_c(t) = \hat{I} \cdot \cos\left(\omega_{me}t + \varphi + \frac{4\pi}{3}\right)$$

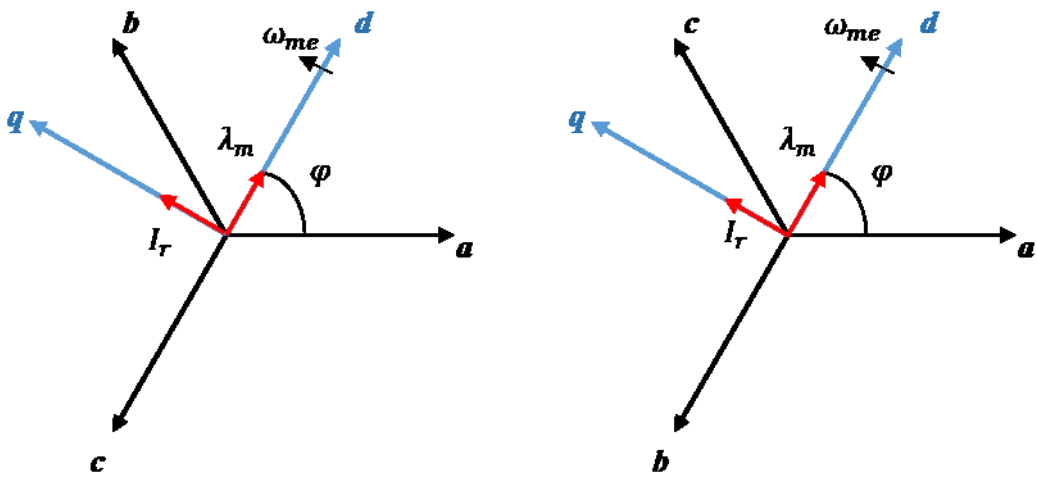


Figure 3.18: Anti-Clockwise and clockwise arrangement of the winding

The procedure to obtain the torque of the machine is:

- Determination the suitable current for each phase in base of the (3.7).
- Imposition of the currents.
- Solving and analysing the problem.
- Get the torque with the MST (*Maxwell's Stress Tensor*).
- Rotation of the rotor and repetition of previous steps until 180° mechanical degrees are covered.

### 3.4.6 Power-speed curve

With this button the designer has the possibility to determine the power-speed curve over the base speed and the speed limit beyond which the base power is no longer maintained.

---

As explained in the Chapter 2, the current phasor is rotated in anti-clockwise way from  $\varphi = \pi/2$  to  $\varphi = \pi$ . For each step, the resulting torque is obtained with the MST method until all the current is supplied in the *d-axis* and hence the torque results zero.

# 4 Analytical design procedure

*This chapter is the heart of this work. It concentrates on the algorithm on which SMDT is based and it provides a full explanation about the well-known analytical equations used to compute geometrical dimensions and machine main features for inner-rotor and outer-rotor motor.*

## 4.1 Introduction

Design a new SPM machine involves taking into account a large number of factors that they could be summarized as follows [23]:

- Economic factor: the first target of designing a new machine is to have minimum costs as much as possible, both in terms of material and manufacturing.
- Special requirements: in some applications, such as in aeronautical field, dimensional constraints and reliability dominate the design stage. It is not different in automotive application, where performance and reliability are the cornerstones of the entire design process.
- Material properties: the economic factor affects the material choice and, consequently, the physical properties of materials affect the performance and machine volume.
- Standard specifications: electrical and mechanical rated data are usually subject to standard specifications, such as the rated frequency or phase-to-phase voltage.

Depending of which factor is considered more important, a large number of solutions could be obtained. Each solution differs from the others ones in base of the parameters have been chosen, in terms of geometrical constraints and material solicitations. Of course, some solutions are better than other ones, but the performances could be similar. By means of the tool developed, the design process can be summarized with the flowchart illustrated in the Fig. 4.1.

---

One input data are entered in the user interface, design process starts by clicking on the button “Project”. As already mentioned, the algorithm proposed is based on the progressive growth of the diameters: for each steps, lamination geometry dimensions are evaluated and checked according to stress indexes and geometrical constraints. When the iterative procedure ends, the results need to be validate with FEA and the feasibility has to be tested, otherwise design specifications have to be changed.

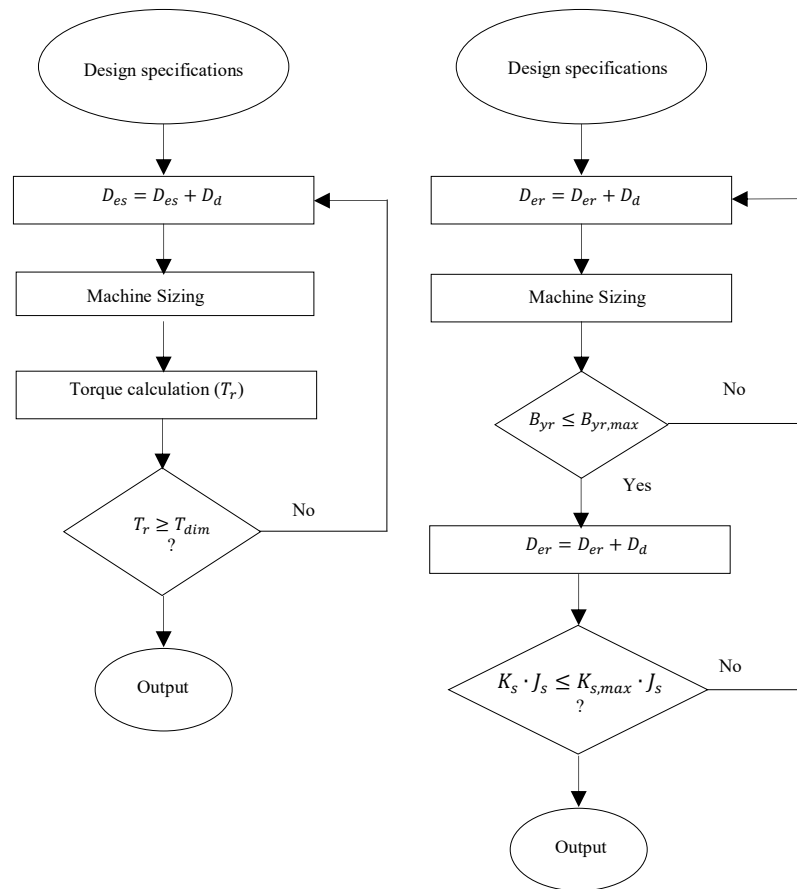


**Figure 4.1:** Sizing algorithm for outer- and inner-rotor motor

## 4.2 Iterative sizing procedures

### 4.2.1 Air gap flux density

In the design process, one of the most important parameter, that has to be evaluated first, is the peak value of the fundamental air gap flux density. As said in the Chapter 2, a PM usually works in the second quarter of its B-H plane of hysteresis loop and the operating point at no-load is defined as the intersection between demagnetization curve and load line.

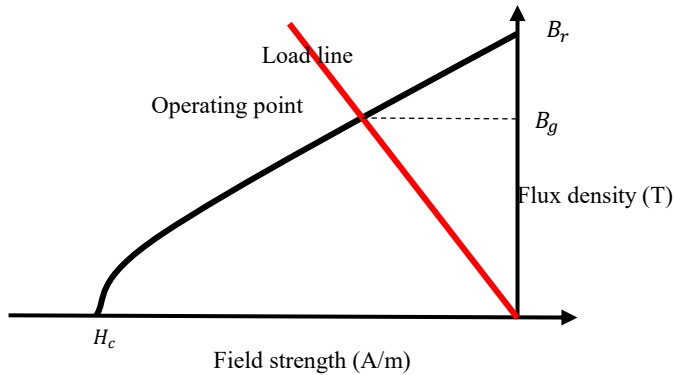


**Figure 4.2:** Operating point of the PM

The working point  $B_g$  can be written as

$$B_g = B_r \cdot \frac{l_m / \mu_r}{(K_{car} \cdot h_{ag} + l_m / \mu_r)} \quad (4.1)$$

Where:

- $B_r$  is the remanence at working temperature.
- $\mu_r$  is the relative permeability of the magnet.
- $l_m$  is the magnet thickness.
- $h_{ag}$  is the geometrical air gap.
- $K_{car}$  is Carter's coefficient.

This formula, compared with the (2.17), also includes the effect of stator slots on air gap flux density.

---

Therefore, as result of permanent magnet presence, the air gap total height is

$$h'_{ag} = h_{eq} + l_m / \mu_r \quad (4.2)$$

By assuming the flux density perfectly rectangular-shaped above the magnet, the peak value of the air gap flux density  $B_g$  and its fundamental space component  $B_{1g}$  can be computed as follows:

$$B_{1g} = \frac{4}{\pi} \cdot B_g \cdot \sin(\alpha) \quad (4.3)$$

Where  $\alpha$  is the half of the magnet angle defined in electrical degrees.

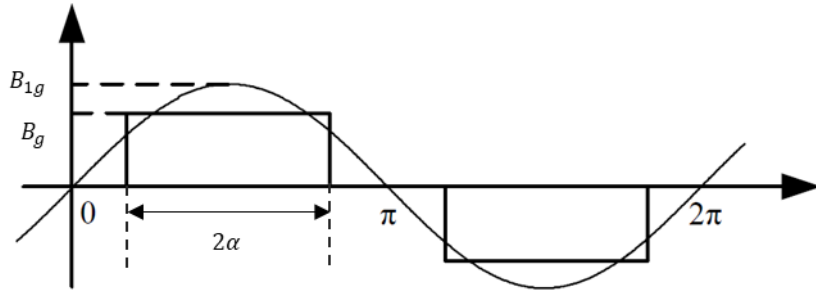


Figure 4.3: Airgap flux density

Usually the coverage angle  $2\alpha$  is chosen lower than  $180^\circ$  because the flux in the zone of transition between north and south does not cross the air gap and it is not linked by the winding arranged in the stator slots, but it travels directly from one pole to the other one. This fraction of flux is not involved in the torque generation, therefore a PM with a full pitch is merely a waste of material as well as an additional cost [1]. In fact, the cost is directly proportional to angle coverage, but the amplitude of fundamental flux density is not. It raises, but not so than how much cost increases. For instance, by increasing the pole angle from  $120^\circ$  to  $180^\circ$ , the magnet volume and the cost increase by 50%, but the maximum value of fundamental flux density increases only by 14%. It is not convenient and for these reasons  $2\alpha$  is usually within a range of  $110^\circ$ - $160^\circ$  [25], as shown in Fig. 4.3.

The half of magnet angle can be also expressed as function of the magnet width  $w_m$ :

$$\alpha = \frac{w_m \cdot p}{(D_{is} - 2 \cdot h_{ag})} = \frac{\alpha_m}{2} \quad (4.4)$$

Therefore, the maximum value of fundamental air gap flux density is

$$B_{1g} = \frac{4}{\pi} \cdot B_g \cdot \sin\left(\alpha_m \cdot \frac{\pi}{2}\right) \quad (4.5)$$

After the air gap flux density computation, the target torque calculation is done by including the friction torque  $T_{fr}$ , defined as percentage of rated torque:

$$T_{dim} = T_r \cdot (1 + T_{fr}/100) \quad (4.6)$$

Once the air gap flux density is computed, the iterative routine starts. The routine is structured in two stages for the both inner-rotor motor and outer-rotor motor:

- Rotor lamination design.
- Stator lamination design.

#### 4.2.2 Sizing routine for inner-rotor machine

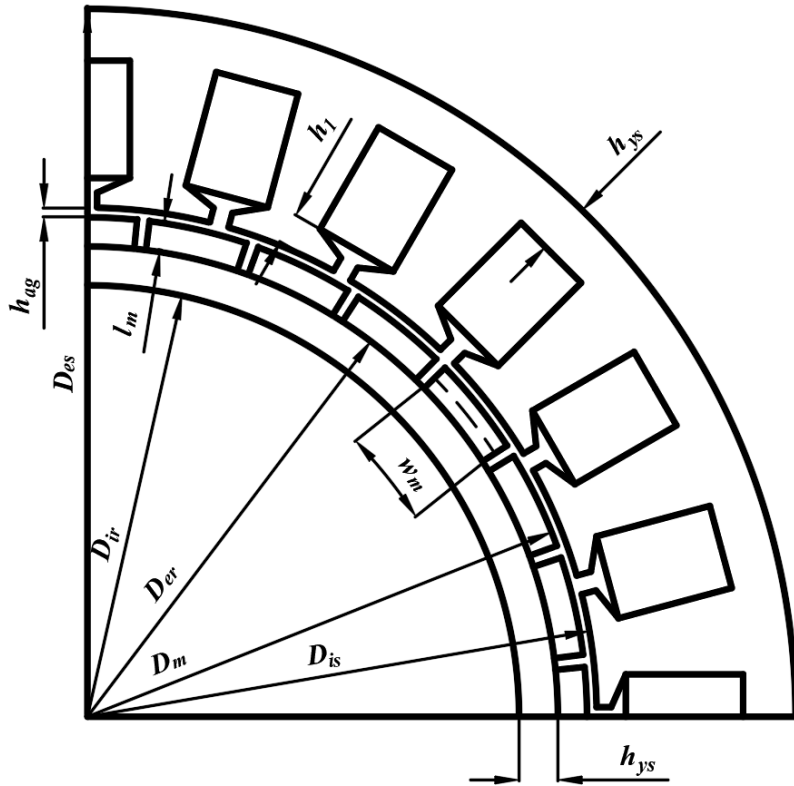


**Figure 4.4:** Cross-section of a SPM synchronous machine with inner rotor

##### 4.2.2.1 Rotor lamination design

The rotor internal diameter  $D_{ir}$  is set equal to zero, if the shaft is made of magnetic material, or is set equal to the minimum shaft diameter  $D_{sh}$ , whereas the external diameter  $D_{er}$  is set a little bit greater than  $D_{sh}$ . In particular, being  $D_d$  the iterative step, the external diameter is computed as first attempt as

$$D_{er} = D_{sh} + D_d \quad (4.7)$$

Knowing the magnet thickness  $l_m$ , the diameter at the height of the magnet surface  $D_m$  and the stator internal diameter  $D_{is}$  are calculated with the following equations:

$$D_m = D_{er} + 2 \cdot l_m \quad (4.8)$$


---

$$D_{is} = D_m + 2 \cdot h_{ag} \quad (4.9)$$

At this point it is possible to define the polar pitch  $\tau_p$  and the magnet length  $w_m$ , necessary to compute the flux passing through the yokes.

$$\tau_p = \frac{\pi \cdot D_{is}}{p} \quad (4.10)$$

$$w_m = \tau_p \cdot \alpha_m \quad (4.11)$$

Subsequently, the active length  $L_{core}$  is computed with the following relation:

$$L_{core} = \lambda \cdot (D_m + h_{ag}) \quad (4.12)$$

As shown in Fig. 4.5, the flux created by the magnet passes through the air gap and the teeth and then it splits in two equal quantities.

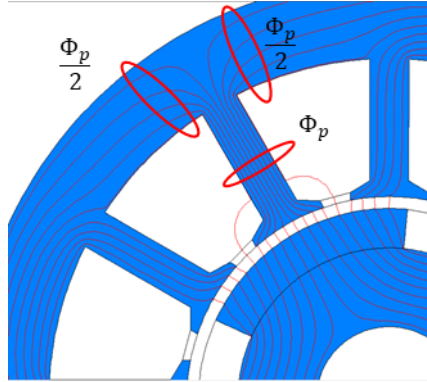


**Figure 4.5:** Flux per pole

Therefore, the peak value of flux per pole and its fundamental space harmonic are

$$\phi_p = w_m \cdot L_{core} \cdot B_g \quad (4.13)$$

$$\phi_{1p} = \frac{2}{\pi} \cdot \tau_p \cdot L_{core} \cdot B_{1g} \cdot \quad (4.14)$$

By supposing the absence of leakage flux, the rotor flux density is computed as

$$B_{yr} = \frac{\frac{\phi_p}{2}}{\frac{(D_{er} - D_{ir})}{2} \cdot L_{core} \cdot K_{fill}} \quad (4.15)$$

If the actual  $B_{yr}$  is greater than the maximum rotor flux density permitted, then the rotor external diameter is progressively increased by  $D_d$  until  $B_{yr,max}$  is achieved. Subsequently, once the rotor flux density admissible is respected, the rotor yoke thickness and internal diameter are calculated:

$$h_{yr} = \frac{\frac{\phi_p}{2}}{B_{yr,max} \cdot L_{core} \cdot K_{fill}} \quad (4.16)$$

$$D_{ir} = D_{er} - 2 \cdot h_{yr} \quad (4.17)$$

It is important to remark that is used  $B_{yr,max}$  instead of the actual rotor flux density  $B_{yr}$  because has been taken a small margin in case of  $B_{yr}$  results slightly greater than  $B_{yr,max}$ .

At the end of this first phase, the algorithm returns the rotor preliminary geometry that guarantees a rotor flux density equal or lower than the maximum imposed one.

#### 4.2.2.2 Stator lamination design

The target of this second stage is getting the stator yoke geometry, included the slot shape and yoke height. Starting by the relation of electromagnetic torque (4.18), the slot useful area is calculated.

$$T_r = \frac{2 \cdot \pi}{4} \cdot B_{1g} \cdot K_s \cdot {D_{h1}}^2 \cdot L_{core} \quad (4.18)$$

Where  $D_{h1}$  is the diameter at the height of the enclosure slot given by

$$D_{h1} = D_{is} + 2 \cdot h_1 \quad (4.19)$$

By reversing the (4.18),  $K_s$ , namely the fundamental linear current density, can be obtained as

$$K_s = \frac{4 \cdot T_r}{\sqrt{2} \cdot \pi \cdot B_{1g} \cdot L_{core} \cdot {D_{h1}}^2} \quad (4.20)$$

$K_s$  can be also calculated with the following formula:

---

$$K_s = \frac{I_s \cdot N_s \cdot K_{avv}}{\pi \cdot D_{h1}} \quad (4.21)$$

Where:

- $K_{avv}$  is the winding factor calculated with the formulas introduced in the Chapter 2.
- $I_s$  is the total slot current.

The latter can be computed in function of the current density  $J_s$  and the overall conductor material area  $A_{cu}$ . Namely

$$I_s = A_{cu} \cdot J_s \quad (4.22)$$

Using the equations (4.21) and (4.22) is possible to derive  $A_{cu}$  and then the slot useful area  $A_{us}$  that includes the slot fill factor  $K_c$  imposed as constraint by the designer.

$$A_{us} = \frac{A_{cu}}{K_c} \quad (4.23)$$

The flux passing through the stator yoke, as well as the rotor yoke flux, is half of the flux per pole and it can be written as

$$\frac{\phi_p}{2} = B_{ys,max} \cdot L_{core} \cdot h_{ys} \cdot K_{fill} \quad (4.24)$$

Where  $h_{ys}$  is the stator yoke thickness.

Introducing the coefficient  $i_{bgs}$  given by

$$i_{bgs} = \frac{B_g}{B_{ys,max} \cdot K_{fill} \cdot p} \quad (4.25)$$

and combining (4.24) with (4.25), the stator yoke thickness can be calculated as follows:

$$h_{ys} = i_{bgs} \cdot \alpha_m \cdot \frac{D_{is} \cdot \pi}{2} \quad (4.26)$$

Subsequently, the slot dimensions are calculated. Since the slots can be rectangular-shaped or trapezoidal-shaped, the maximum value of the tooth flux density is achieved where the flux passage cross-section is narrower. For rectangular slot, the cross-section is constant along the

tooth length, hence the flux density too, whereas, in the trapezoidal slot, the maximum value of tooth flux density is achieved in proximity of the head, namely where the slot width is wider and tooth width is narrower.

About the tooth top width is mandatory make some remarks about the type of winding used for the stator. In fact, an important difference must be made between distributed winding and fractional-slot concentrated winding. In the first case, the number of slots per pole per phase  $q$  is usually greater than one, so the width of the magnet is usually larger than the slot pitch. This consideration permits us to assume that all the flux created by the magnet passes through the teeth. In this case, the slot top width expression assumes this form:

$$w_{tt} = i_{bds} \cdot \tau_s \quad (4.27)$$

Where  $i_{bds}$  is a coefficient given by:

$$i_{bds} = \frac{B_g}{B_{ts,max} \cdot K_{fill}} \quad (4.28)$$

The slot pitch  $\tau_s$  is calculated by the following equations:

$$\tau_s = \frac{D_{is} \cdot \pi}{N_s} \quad (4.29)$$

However, in the case of FSCW,  $q$  is lower than one and the hypothesis that all the flux crosses the tooth could be not valid. In this kind of winding arrangement, the total slots number is minor of the number of magnet poles and the tooth width could be wider than pole coverage length. With reference to Fig. 4.6, if this happens the shunting effect on the flux occurs: in fact, not all the magnetic field lines entirely cross the tooth to reach the yoke, but some of them travel into the tooth's head going directly to the other pole, without passing across the stator yoke. This quote of flux is leakage flux and it must be limited.

The algorithm allows to correct the slot top width by setting it a little bit lower than one

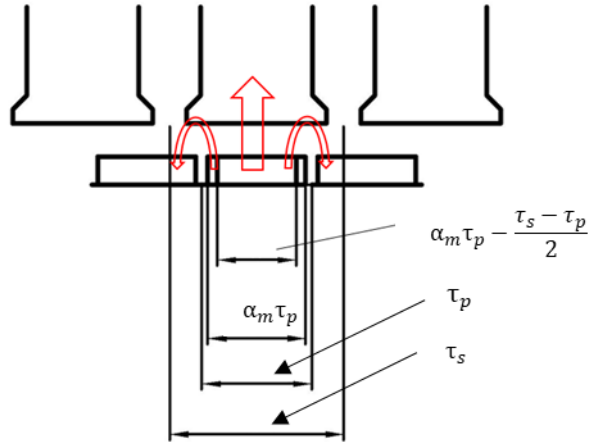


**Figure 4.6:** Shunt effect of the magnetic field lines

determined with the (4.27) [26]. To be more specific, if the stator slot pitch is greater than the magnet width in proximity of  $D_m$ , the top tooth width is calculated as

$$w_{tt} = i_{bds} \cdot \frac{D_m \cdot \pi}{p} \cdot \alpha_m \quad (4.30)$$

Once the tooth top width is calculated, the other dimensions can be derived.

The slot width can be obtained by using the equation (4.31),

$$w_{st} = \frac{D_{h1} \cdot \pi}{N_s} - w_{tt} \quad (4.31)$$

In order to getting the other dimensions of the slot, is necessary taking into account the shape of the slot.

### Rectangular slot

With reference to Fig. 4.7, the useful height of the slot and its bottom width are easily deducible since the slot area is rectangular and top width is known.

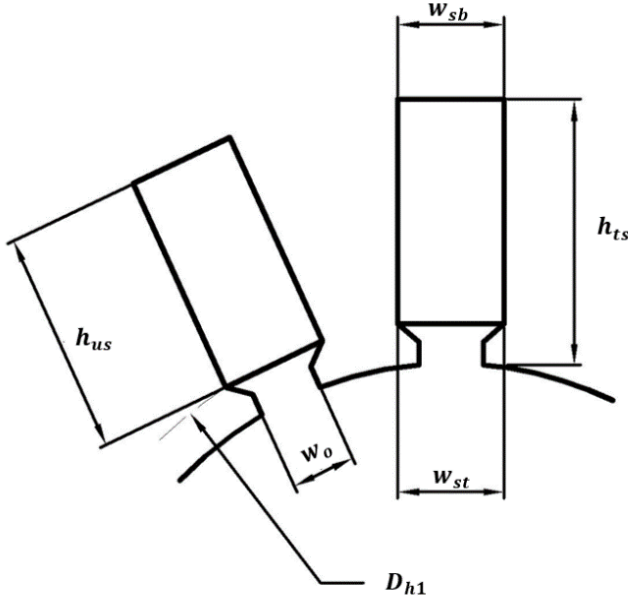


**Figure 4.7:** Rectangular slot in SPM machines with inner rotor

In particular, the bottom width is the same of the top one, as reported in (4.32).

$$w_{sb} = w_{st} \quad (4.32)$$

The slot height is calculated as

$$h_{us} = \frac{A_{us}}{w_{sb}} \quad (4.33)$$

### Trapezoidal slot

By using the definition of trapezoidal area, the trapezoidal slot area can be calculated with the following expression:

$$A_{us} = \frac{w_{st} + w_{sb}}{2} \cdot h_{us} \quad (4.34)$$


---

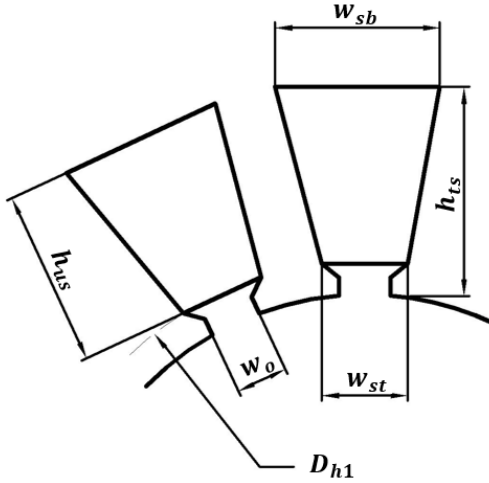


**Figure 4.8:** Trapezoidal slot in SPM machines with inner rotor

If the slot is trapezoidal, then the tooth is rectangular-shaped as it has a constant width along the radius. Therefore, since  $w_{tb}$  is also known, then  $w_{sb}$  can be easily computed as:

$$w_{sb} = \tau'_s - w_{tb} \quad (4.35)$$

Where  $\tau'_s$  is

$$\tau'_s = \frac{\pi \cdot (D_{h1} + 2 \cdot h_{us})}{N_s} = \frac{\pi \cdot D_{h1}}{N_s} + \frac{2 \cdot h_{us} \cdot \pi}{N_s} \quad (4.36)$$

Hence, by linking (4.32), (4.35) and (4.36),  $w_{sb}$  can be evaluated as

$$w_{sb} = w_{st} + \frac{2 \cdot h_{us} \cdot \pi}{N_s} \quad (4.37)$$

Substituting the equation (4.37) in the (4.34), the latter can be reversed and expressed as a function of  $h_{us}$ :

$$h_{us} = \frac{-w_{st} + \sqrt{w_{st}^2 + \frac{4 \cdot \pi \cdot A_{us}}{N_s}}}{\frac{2 \cdot \pi}{N_s}} \quad (4.38)$$

#### 4.2.2.3 Sizing conclusion

In order to conclude the stator sizing, other dimensions are derived from the last equations. In particular the slot total height it can be calculated as

$$h_{ts} = h_{us} + h_1 \quad (4.39)$$

The slot total area includes also the opening slot and it can be written as

$$A_{ts} = A_{us} + w_o \cdot h_{11} + \frac{(w_o + w_{st})}{2} \cdot h_{12} \quad (4.40)$$

Since the slot dimensions are known, also the tooth dimensions can be calculated, in particular the tooth bottom width and the tooth top width:

$$w_{tt} = \frac{\pi \cdot D_{h1}}{N_s} - w_{st} \quad (4.41)$$

$$w_{tb} = \frac{\pi \cdot (D_{is} + 2 \cdot h_{ts})}{N_s} - w_{sb} \quad (4.42)$$

At the final of this stage, the algorithm returns all the stator lamination dimensions.

#### 4.2.2.4 Exit condition

The exit condition of the iterative procedure depends on the  $K_s \cdot J_s$  product. This choice can be explained by noticing the behaviour of the algorithm at the first iterations. In fact, at the beginning, the peak value of fundamental flux density, hence the flux per pole too, is very small due to small diameters, so the algorithm returns a value very high of  $K_s \cdot J_s$  to fulfil the target torque. Hence, the solution would converge to tapered slots, as shown in Fig. 4.9 , if the rated torque was very high. In order to avoid such solution, the product between the linear current density  $K_s$  and current density  $J_s$  is checked at each step and compared with the maximum value admissible.



Figure 4.9: Tapered slots [26]

The  $K_{s,max} \cdot J_s$  product is a design constraint and its value is chosen by taking into account of the type of cooling system used for the motor. In table 4.1 typical values of  $K_{s,max} \cdot J_s$  are shown.

**Table 4.1:** Typical values of  $K_{s,max} \cdot J_s$

Cooling method	$K_{s,max} \cdot J_s$ A <sup>2</sup> /cm/mm <sup>2</sup>
Air cooling	1000 - 2000
Liquid cooling	3000 - 4000

The algorithm stops looping when  $K_s \cdot J_s$  is smaller than  $K_{s,max} \cdot J_s$ .

### 4.2.3 Sizing routine for outer-rotor machine

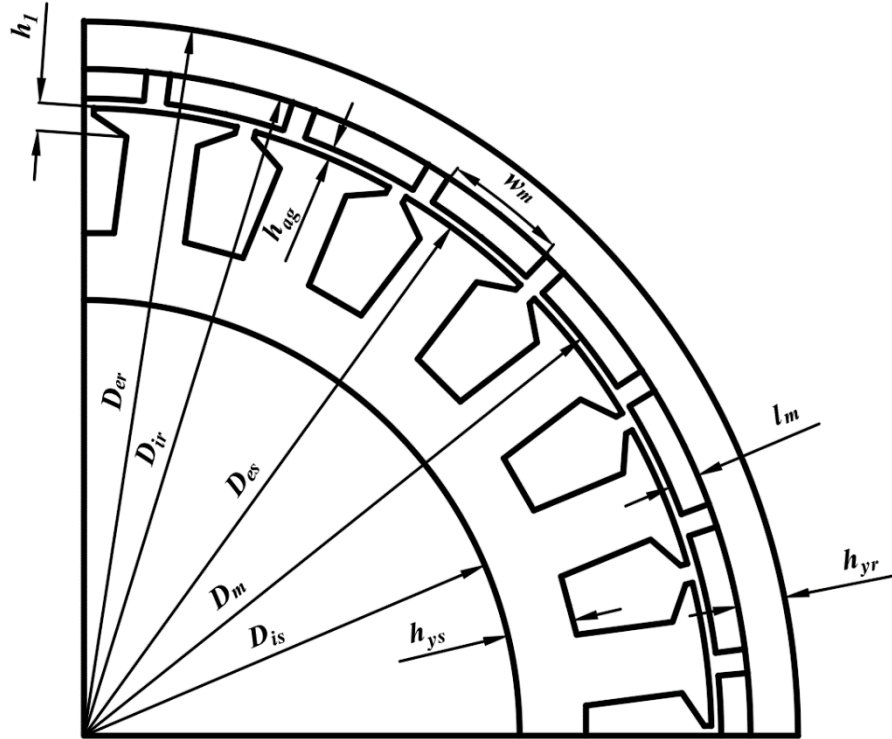


**Figure 4.10:** Cross-section of a SPM synchronous machine with outer rotor

#### 4.2.3.1 Stator lamination design

At the beginning, the stator internal diameter is set equal to zero, if the shaft is made of magnetic material, or is set equal to the shaft diameter. The stator external diameter is obtained by taking into account of the stress indexes chosen for the stator yoke.

Namely, it can be written as

$$D_{es} = \frac{D_{sh}}{1 - 2 \cdot i_{bgs} \cdot \alpha_m \cdot \frac{\pi}{Z}} \quad (4.43)$$

Subsequently, the iterative procedure starts: firstly  $D_{es}$  is set a little bit greater than diameter calculated in (4.43), as first attempt.

$$D_{es} = D_{es} + D_d \quad (4.44)$$

Since  $D_{es}$  is known, the other diameters of the machine are derived.

$$D_m = D_{es} + 2 \cdot h_{ag} \quad (4.45)$$

$$D_{ir} = D_m + 2 \cdot l_m \quad (4.46)$$

$$L_{core} = \lambda \cdot (D_{es} + h_{ag}) \quad (4.47)$$

Where:

- $D_m$  is the diameter in proximity of the surface of the magnet.
- $D_{ir}$  is the rotor internal diameter.
- $L_{core}$  is the stack length.

Neglecting the flux leakage is possible to compute the flux per pole and its fundamental amplitude by using the equations (4.13) and (4.14), where the polar pitch is defined, in this case, as

$$\tau_p = \frac{\pi \cdot D_{es}}{p} \quad (4.48)$$

Once the polar pitch and the most important diameters are determined, the algorithm provides also the stator yoke and slot dimensions. As said before, the flux that flows into the stator yoke is equal to half of the flux per pole created by the magnet. Considering the stress index coefficient  $i_{bgs}$  written in (4.25), the stator yoke thickness can be expressed with the following relation:

$$h_{ys} = i_{bgs} \cdot \alpha_m \frac{D_{es} \cdot \pi}{2} \quad (4.49)$$

Now, we introduce the slot pitch:

$$\tau_s = \frac{\pi \cdot D_{es}}{N_s} \quad (4.50)$$

As explained for inner-rotor motor sizing, the tool also provides a procedure able to correct the tooth dimension in order to limit the shunt effect of the magnetic field lines close to the teeth.

To be more specific, if the slot pitch  $\tau_s$  is smaller than the magnet width at  $D_m$ , then the tooth top width is computed with the following equation:

$$w_{tt} = i_{bds} \cdot \frac{\pi \cdot D_{es}}{N_s} \quad (4.51)$$

Where  $i_{bds}$  is defined in (4.28).

On the contrary, if the slot pitch is higher than magnet width, the tooth top width is computed with the following formula:

$$w_{tt} = i_{bds} \cdot \alpha_m \cdot \frac{\pi \cdot (D_{es} + 2 \cdot h_{ag})}{p} \quad (4.52)$$

It is necessary to consider the slot shape selected by the designer for other dimensions designing, as made for inner-rotor structure.

### Trapezoidal slot

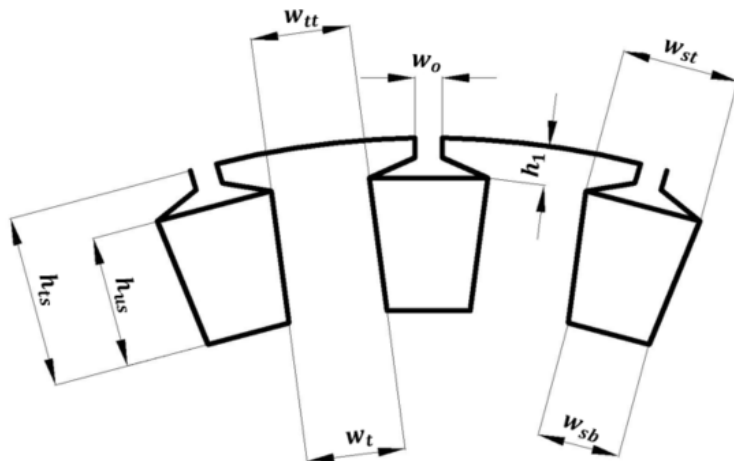


**Figure 4.11:** Trapezoidal slot in SPM machines with outer rotor

In case of trapezoidal slot for outer-rotor machine is important to remark that once the stator external diameter and yokes thickness are determined, then the space available for the slot is limited.

Regarding trapezoidal slot shape, the algorithm can lead the solution converging to triangular shape. If this situation occurs, the diameter at the slot bottom is called *critical diameter*  $D_{crit}$  and it is calculable with the following relation:

$$D_{crit} = \frac{w_{tt}}{\sin(\beta_c/2)} \quad (4.53)$$

Where  $\beta_c$  is the slot angular pitch can be calculated as

$$\beta_c = \frac{2 \cdot \pi}{N_s} \quad (4.54)$$

With reference at Fig. 4.12, if  $D_{sh} + 2 \cdot h_{ys} > D_{crit}$ , then the slot bottom width is evaluated with the (4.55):

$$w_{sb} = (D_{sh} + 2 \cdot h_{ys} - D_{crit}) \cdot \tan\left(\frac{\beta_c}{2}\right) \quad (4.55)$$

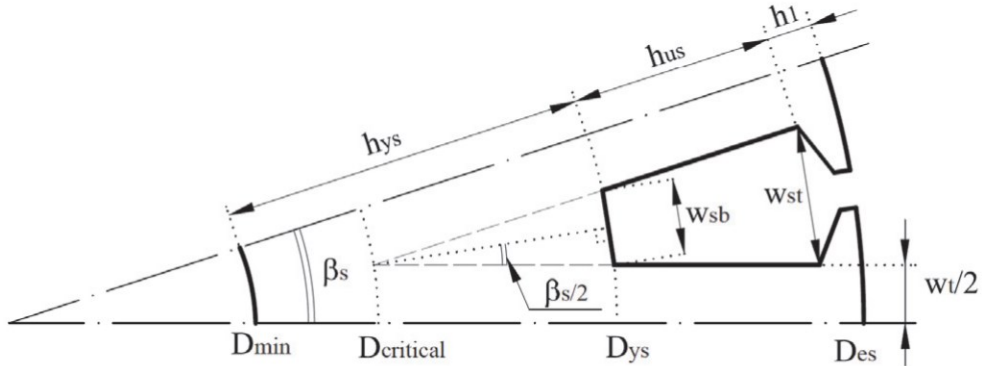


Figure 4.12: Critical diameter [26]

On the contrary, in case of  $D_{cr} > D_{sh} + 2 \cdot h_{ys}$ , triangular slots are obtained. Hence, the algorithm sets the slot bottom width equal to zero (4.56) and stator yoke height is recalculated (4.57).

$$w_{sb} = 0 \quad (4.56)$$

$$h_{ys} = \frac{D_{cr} - D_{sh}}{2} \quad (4.57)$$

Instead, the slot top width is calculated by using the (4.58).

$$w_{st} = (D_{es} - 2 \cdot h_1 - D_{crit}) \cdot \tan\left(\frac{\beta_c}{2}\right) \quad (4.58)$$

### Rectangular slot

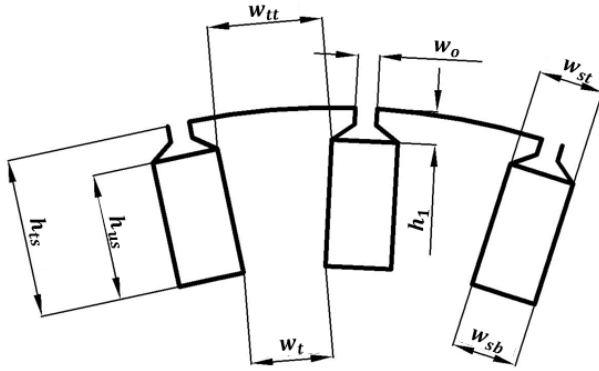


**Figure 4.13:** Rectangular slot in SPM machines with outer rotor

For rectangular slots, the algorithm provides an optimization procedure to get the best rectangular area available. As Fig. 4.14 illustrates, it can be noticed that is possible obtaining a large number of different rectangular areas.

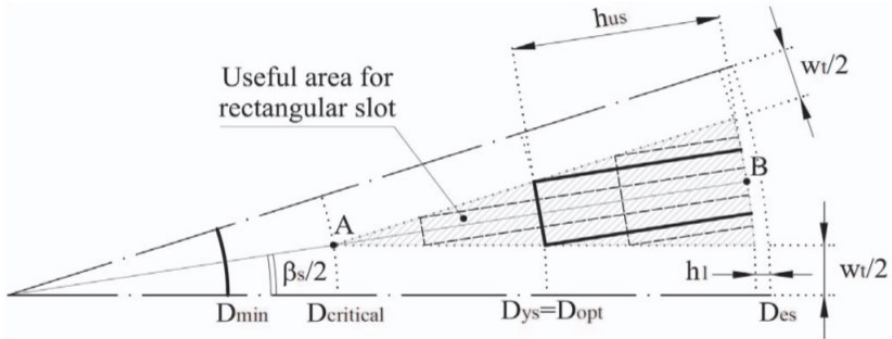


**Figure 4.14:** Best area available in a triangular slot [26]

The best solution depends on which aspect designer is intentioned to focus on. For instance, maximum slot area could be preferred in order to limit the copper losses for high power density applications or, alternatively, deep slots could be preferred to increase the flux leakage to enhance field-weakening capability, commonly poor in SPM synchronous machines because of small magnetizing inductance [27].

In particular, the algorithm provides a solution which aims to obtain the maximum slot area.

In (4.59), the optimal diameter  $D_{opt}$  at which corresponds the optimal stator yoke height is introduced.

---

$$D_{opt} = \frac{D_{es} + D_{crt}}{2} - h_1 \quad (4.59)$$

$$h_{ys} = h_{ys,opt} = \frac{D_{opt} - D_{sh}}{2} \quad (4.60)$$

Hence, the slot bottom width and slot top width can be calculated as follows:

$$w_{sb} = (D_{sh} + 2 \cdot h_{ys} - D_{crit}) \cdot \tan\left(\frac{\beta_c}{2}\right) \quad (4.61)$$

$$w_{st} = w_{sb} \quad (4.62)$$

Subsequently, also the slot useful height and slot useful area are computed for both trapezoidal and rectangular slot:

$$h_{us} = \frac{D_{es} - D_{sh} - 2 \cdot (h_1 + h_{ys})}{2} \quad (4.63)$$

$$A_{us} = h_{us} \cdot \left(\frac{w_{sb} + w_{st}}{2}\right) \quad (4.64)$$

As regards other stator and rotor dimensions, they can be easily derived from previous equations. Firstly the slot dimensions, such as the total slot height and the total slot area, are calculated. Then, the top and tooth bottom width are computed as

$$w_{tb} = \frac{\pi \cdot (D_{es} - 2 \cdot h_{ts})}{N_s} - w_{sb} \quad (4.65)$$

$$w_{tt} = \frac{\pi \cdot (D_{es} - 2 \cdot h_1)}{N_s} - w_{st} \quad (4.66)$$

#### 4.2.3.2 Exit condition

Once the slot useful area is determined, the torque obtainable is derived. Preliminarily, the overall conductor material area is computed taking into account of the slot fill factor (4.67) and then the linear current density is calculated (4.68).

$$A_{cu} = K_c \cdot A_{us} \quad (4.67)$$

$$K_s = \frac{K_{avv} \cdot J_s \cdot N_s \cdot A_{cu}}{\pi \cdot D_m} \quad (4.68)$$

Then, the electromagnetic torque can be calculated as

$$T_r = \frac{\sqrt{2} \cdot \pi}{4} \cdot B_{1g} \cdot K_s \cdot L_{core} \cdot D_m^2 \quad (4.69)$$

The exit condition for this iterative procedure, unlike the inner-rotor motor design procedure, is the torque obtained. If  $T_r$  is lower than  $T_{dim}$ , then the stator external diameter is progressively increased until the target torque is achieved.

#### 4.2.3.3 Rotor lamination design

At the final of the design process, the rotor dimensions are determined. In particular, for the yoke rotor thickness  $h_{yr}$  the equation used for the inner rotor (4.16) is also used for the outer-rotor. Hence, since the yoke thickness is known, the rotor external diameter can be obtained as

$$D_{er} = D_{ir} + 2 \cdot h_{yr} \quad (4.70)$$

For outer rotor design procedure  $K_s \cdot J_s$  is a design output and it is not constrained by the designer, but is mandatory verify if its value is suitable for cooling system selected for such application. In order to have an idea about losses and power and torque density resulting from the project, the algorithm also provides the length of the winding, volume and weight of materials used for motor designing.

## 4.3 Stator winding length

The winding length is evaluated by taking into account the type of winding selected by the designer. In fact, distinction between distributed and FSCW is necessary to evaluate correctly how much the average coil is long. First of all, the estimation of the slot average width  $w_{as}$  at mid-height of the slot is done, as we assume a coil placed at the middle of the slot.

For machines with inner rotor,  $w_{as}$  is compute with the following formula:

$$w_{as} = \frac{\pi \cdot (D_{is} + h_{ts})}{N_s} - w_{at} \quad (4.71)$$

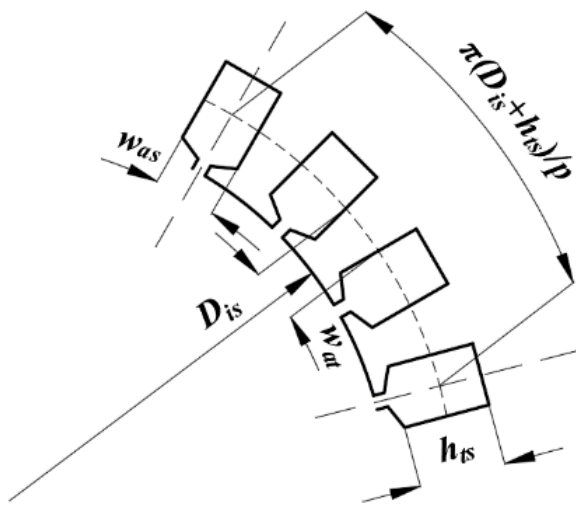


**Figure 4.15:** Slots model in SPM machines with inner rotor

Where  $w_{at}$  is the average tooth width obtainable as

$$w_{at} = \frac{w_{tt} + w_{tb}}{2} \quad (4.72)$$

Instead, for machine with outer rotor,  $w_{as}$  can be written as follows:

$$w_{as} = \frac{\pi \cdot (D_{es} - h_{ts})}{N_s} - w_{at} \quad (4.73)$$

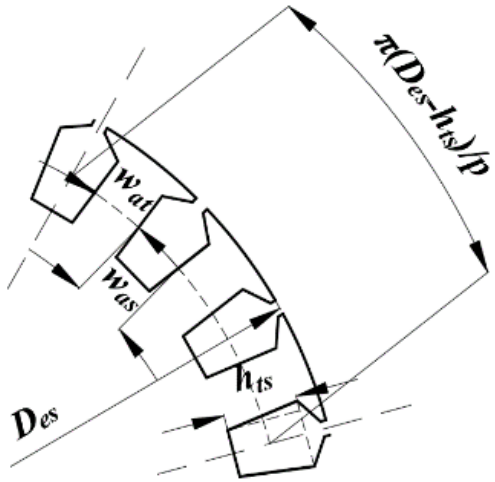


Figure 4.16: Slots model in SPM machines with outer rotor

#### 4.3.1 Distributed winding

With reference to the winding model illustrated in the Fig. 4.17, the maximum end-winding length for inner-rotor motor is estimated as

$$L_{ew} = K_{racc} \cdot \left( \frac{\pi \cdot (D_{is} + h_{ts})}{p} + w_{as} \right) \cdot \frac{\pi}{2} \quad (4.74)$$

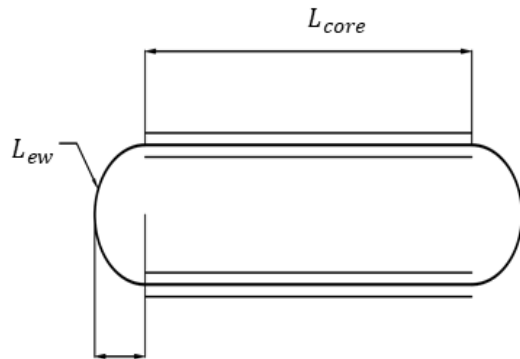


Figure 4.17: Winding model

Whereas for outer-rotor motor is used the (4.75).

$$L_{ew} = K_{racc} \cdot \left( \frac{\pi \cdot (D_{es} - h_{ts})}{p} + w_{as} \right) \cdot \frac{\pi}{2} \quad (4.75)$$

Where  $K_{racc}$  is the pitch factor defined as

$$K_{racc} = 1 - \frac{N_{rac}}{3 \cdot q} \quad (4.76)$$

Considering the front and back side of the winding and the active winding placed into the slots, the winding total length can be computed as

$$L_w = 2 \cdot (L_{core} + L_{ew}) \quad (4.77)$$

### 4.3.2 Fractional-Slot Concentrated Winding

For FSCW winding type, the end-winding length can be determined with the (4.78).

$$L_{ew} = \frac{\left( \frac{\pi \cdot w_{min}}{2} + \frac{\pi \cdot w_{max}}{2} \right)}{2} \quad (4.78)$$

Where  $w_{min}$  and  $w_{max}$  are the maximum and the minimum distance between two slots, respectively.

For inner-rotor machines  $w_{min}$  and  $w_{max}$  can be written as

$$w_{min} = w_{tt} \quad (4.79)$$

$$w_{max} = 2 \cdot w_{sb} + w_{tb} \quad (4.80)$$

Instead, for outer-rotor machines, they can be computed with the following formulas:

$$w_{min} = w_{tb} \quad (4.81)$$

$$w_{max} = 2 \cdot w_{st} + w_{tt} \quad (4.82)$$

As done for the distributed winding, the winding total length, assumed as a mean value, can be evaluated with the (4.77).

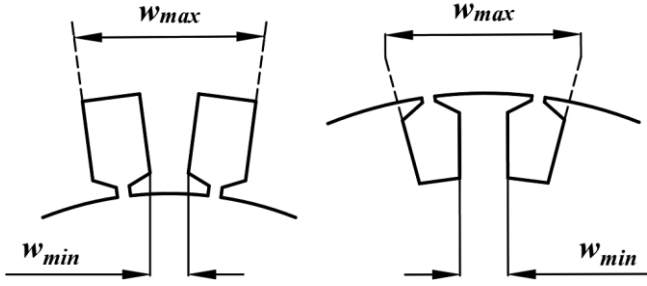


**Figure 4.18:** Minimum and Maximum end-winding lengths in FSCW

The algorithm also estimates the end-winding axial length, in order to have an idea about the machine axial encumbrance. Specifically, it is evaluated with the (4.83) for distributed winding, whereas (4.84) is used for FSCW for both inner- and outer-rotor machines.

$$L_{ew,ax} = \frac{L_{ew}}{\pi} \quad (4.83)$$

$$L_{ew,ax} = \frac{L_{ew}}{2} \quad (4.84)$$

## 4.4 Total volume and weight of the machine

Considering the geometrical dimensions resulting by the design, volumes and weights of the machine can be easily evaluated for the both types of motor.

Firstly, the teeth volume is evaluated: the entire teeth volume is ideally equal to the total volume of iron till the slot height, at which the air volume related to slots volume is subtracted, as written in (4.85).

$$V_{teeth} = (\pi \cdot h_{ts} \cdot D_{a,s} - N_s \cdot A_{ts}) \cdot L_{core} \cdot K_{fill} \quad (4.85)$$

Where  $D_{a,s}$  is the diameter at mid-height of the slot that can be calculated with the (4.86) for the inner rotor motor or with the (4.87) for the outer-rotor motor.

$$D_{a,s} = D_{is} + h_{ts} \quad (4.86)$$

$$D_{a,s} = D_{es} - h_{ts} \quad (4.87)$$

Then, the stator and rotor yokes volume are calculated as

$$V_{yr} = \pi \cdot h_{yr} \cdot D_{a,yr} \cdot L_{core} \cdot K_{fill} \quad (4.88)$$

$$V_{ys} = \pi \cdot h_{ys} \cdot D_{a,ys} \cdot L_{core} \cdot K_{fill} \quad (4.89)$$

Where  $D_{a,yr}$  and  $D_{a,ys}$  are intended as the diameters at mid-height of the yokes.

For inner-rotor machine are equal to

$$D_{a,yr} = D_{er} - h_{yr} \quad (4.90)$$

$$D_{a,ys} = D_{es} - h_{ys} \quad (4.91)$$

Whereas, for outer-rotor machine they are computed as

$$D_{a,yr} = D_{er} - h_{yr} \quad (4.92)$$

$$D_{a,ys} = D_{is} + h_{ys} \quad (4.93)$$

Therefore, the iron total volume is calculated summing all the iron volumes previously obtained.

$$V_{ir} = V_{teeth} + V_{ys} + V_{yr} \quad (4.94)$$

As regards the magnet total volumes it is possible to use the formula (4.95), for inner-rotor motor or (4.96) for outer-rotor motor.

$$V_{mg} = \pi \cdot \alpha_m \cdot (D_m - l_m) \cdot l_m \cdot L_{core} \quad (4.95)$$

$$V_{mg} = \pi \cdot \alpha_m \cdot (D_m + l_m) \cdot l_m \cdot L_{core} \quad (4.96)$$

As result of the previous results, the total winding volume is obtained as

$$V_{cu} = N_s \cdot A_{us} \cdot K_C \cdot (L_{core} + L_{ew}) \quad (4.97)$$

Then, the total volume of active materials is calculated summing all volumes resulting from the previous calculations.

$$V_{tot} = V_{cu} + V_{mg} + V_{ir} \quad (4.98)$$

Furthermore, also the weights of the winding, magnets and core are calculated by taking into account of the respective specific weights.

$$W_{cu} = \gamma_{cu} \cdot V_{cu} \quad (4.99)$$

$$W_{ir} = \gamma_{ir} \cdot V_{ir} \quad (4.100)$$

$$W_{mg} = \gamma_{mg} \cdot V_{mg} \quad (4.101)$$

In conclusion, the total weight of the materials is obtained by summing all the weights previously estimated.

$$W_{tot} = W_{cu} + W_{ir} + W_{mg} \quad (4.102)$$

## 4.5 Loss models

Losses estimation allows having an idea about the energy conversion efficiency. In fact, by assuming to neglect the frictional and stress losses, it is possible to define the efficiency as

$$\eta = \frac{P_{out}}{P_{out} + P_{ir} + P_{cu}} \quad (4.103)$$

In SPM machines, winding losses represents the highest contributor on total losses and the core losses are the second largest [1]. As known, core losses refer to the sum of two phenomena: eddy-current and hysteresis, which are proportional to the frequency and to the flux density.

The specific losses can be written as

$$p_{ir}(B, f) = p_{hys} + p_{eddy} = k_{hys} \cdot B^{\beta_{st}} \cdot f + k_{eddy} \cdot B^2 \cdot f^2 \cdot \delta \quad (4.104)$$

Where:

- $B$  is the peak value of the flux density.
- $f$  is the frequency expressed in Hz.
- $\delta$  is the lamination thickness in mm.
- $k_{hys}$  and  $k_{eddy}$  are the hysteresis and eddy-current constant, respectively. Typical values are shown in the table 4.2.

Table 4.2: Typical values of  $k_{hys}$  and  $k_{eddy}$ . Table extracted from [28]

Material	$k_{hys}$	$k_{eddy}$
Iron lamination	0.048	-
Iron lam. 1.5 % silicon	0.047	0.00092
Iron lam. 3 % silicon	0.038	0.00064
Iron lam. 4 % silicon	0.029	0.00050

The manufacturer often provides the specific losses  $C_p$  calculated at 50 Hz and 1 T with the assumption of sinusoidal magnetic field.

In this case, in order to evaluate the total specific losses is used the following formula:

$$P_{ir} = C_p \cdot W \cdot K_w \cdot B^2 \cdot \left(\frac{f_r}{50}\right)^{1.25} \quad (4.105)$$

Where

- $W$  is the material weight regarded.
- $K_w$  is the *working factor*, namely a factor that takes into account of workings on the laminations that usually increase the losses.

The both experienced and beginner designers usually have two methods to predict core losses: using analytical expressions, as those introduced before, or using manufacturer's measured losses presented in form of tables or curves.

In the algorithm proposed, the second method has been preferred and the specific iron losses measured in W/kg evaluated for different flux density peak values and for different operating frequencies are already known.

Therefore, *SMDT* firstly provides a core losses prediction by interpolating table data in order to obtain the specific losses at the rated frequency. Then, interpolation is made for the peak values of flux density defined as constraints for the stator yoke and tooth. However, it is important to remark that in this way the overall losses represent the maximum value that could occur since the design output guarantees actual flux densities lower than those maximum imposed. They are so overestimated. With these considerations in mind, once specific losses are known by interpolation process, the expression of the total losses can be written:

$$P_{ir} = \gamma_{ir} \cdot (V_{ys} \cdot C_{ys} + V_{teeth} \cdot C_{teeth}) \quad (4.106)$$

Where  $C_{ys}$  and  $C_{teeth}$  are specific losses of the teeth and of stator, respectively. The rotor are neglected since can be regarded always lower than stator ones.

In conclusion, winding losses are calculated too. In particular, they can be estimated with the following relation:

$$P_{cu} = \rho_{cu} \cdot J_s^2 \cdot V_{cu} \quad (4.107)$$

Where  $\rho_{cu}$  represents the resistivity of conductive material at winding operating temperature  $T_{wdg}$ .

## 4.6 Equivalent circuit parameters

An estimation of the most important machine parameters such as the stator resistance or leakage reactance is indispensable to have an idea about electric and magnetic behaviour of the machine designed. In this section, all formulas to compute them are presented.

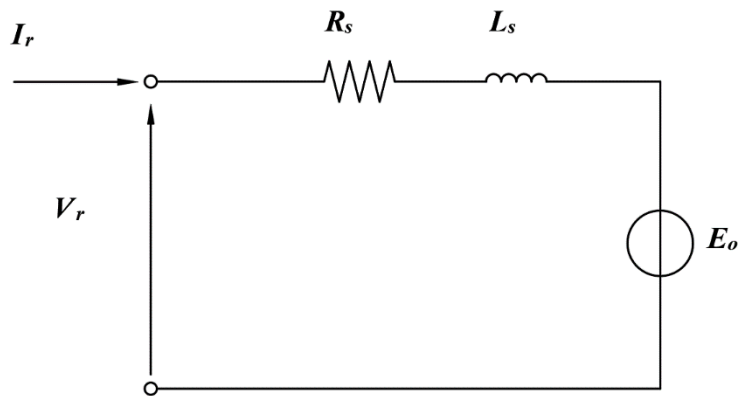


**Figure 4.19:** One-phase equivalent circuit

With reference to Fig. 4.19 which illustrates the equivalent circuit of a single-phase, the phase voltage at steady state can be written as

$$\vec{V}_r = R_s \cdot \vec{I}_r + j\omega L_s \cdot \vec{I}_r + \vec{E}_0 \quad (4.108)$$

The rms-value of the voltage induced in a winding phase due to the fundamental harmonic of flux per pole  $\phi_{1p}$  can be calculated as

$$E_o = \frac{2 \cdot \pi}{\sqrt{2}} \cdot f_r \cdot K_{avr} \cdot \phi_{1p} \cdot \frac{Z_{ph}}{2} \quad (4.109)$$

Where  $Z_{ph}$  is the number of conductors in series per phase. As deducible,  $Z_{ph}$  is unknown at this point, therefore, its computation is postponed to the section 4.6.4.

#### 4.6.1 Stator resistance

The winding losses calculated before can be modelled by introducing the one-phase stator resistance  $R_s$  into the equivalent circuit. One phase, whatever the winding arrangement is, can be considered made up of  $Z_{ph}$  conductors in series per phase. The cross-section of each conductor is calculated according to equation (4.110):

$$A_{wire} = \frac{A_{cu}}{N_{cs}} \quad (4.110)$$

Where:

- $A_{cu}$  is the actual area destined to conductive material.
- $N_{cs}$  is the number of conductors per slot, obtainable with the relation (4.111).

$$N_{cs} = \frac{Z_{ph} \cdot 3}{N_s} \quad (4.111)$$

It is important to bear in mind that only three-phase winding is considered in this case.

Said that, one-phase stator resistance can be obtained with the following:

$$R_s = \rho_{cu} \cdot \frac{Z_{ph} \cdot \left(\frac{L_w}{2}\right)}{A_{wire}} \quad (4.112)$$

Where  $\rho_{cu}$  is the resistivity of conductor material selected and evaluated at the operating winding temperature  $T_{wdg}$ .

## 4.6.2 Synchronous inductance for distributed winding

The synchronous inductance can be calculated as reported in [2].

Namely, it can be written as

$$L_s = L_m + L_{sl} + L_{ec} \quad (4.113)$$

Where:

- $L_m$  is the main inductance.
- $L_{sl}$  is the slot leakage inductance.
- $L_{ec}$  is the end-connection (end-winding) leakage inductance

### 4.6.2.1 Main inductance

The main inductance can be theoretically written as reported in Appendix A, namely as

$$L_m = \frac{3}{2} \cdot \sum_{h=6k+1} \left( \frac{Z_{ph} \cdot K_{avv,h}}{h \cdot \pi \cdot pp} \right)^2 \cdot \frac{1}{\mathfrak{R}_t} \quad (4.114)$$

As can be noticed, the main inductance is the sum of a large number of harmonics resulting from all space harmonics of MMF. However, just the fundamental one is considered useful for the electromechanical energy conversion since other ones rotate at different speeds than the synchronous one and, furthermore, can negatively affect the correct operation of the machine.

Therefore, it is possible to state that  $(L_m - L_{m,1})$  can be interpreted as the air gap leakage inductance  $L_\sigma$  with negative contribute at torque production, where  $L_{m,1}$  can be obtained by replacing  $h = 1$  into the (4.114). Namely,

$$L_{m,1} = \frac{3}{2} \cdot \left( \frac{Z_{ph} \cdot K_{avv,h}}{\pi \cdot pp} \right)^2 \cdot \frac{1}{\mathfrak{R}_t} \quad (4.115)$$

$$L_\sigma = L_m - L_{m,1} \quad (4.116)$$

In case of distributed winding with reduced pitch, the main inductance is calculated as

$$L_m = \frac{4 \cdot Z_{ph}^2}{p^2} \frac{20q^3 + 2q \cdot (2 - 3N_{rac}^2) + N_{rac}(N_{rac}^2 - 1)}{144q^3} \cdot \frac{\mu_0 \cdot \pi \cdot D_{ag} \cdot L_{core}}{2 \cdot h_{eq}} \quad (4.117)$$


---

Therefore, the tool calculates the main inductance for distributed winding by using the 4.117. If the pitch is not reduced, then  $N_{rac}$  is equal to zero.

#### 4.6.2.2 Slot leakage inductance

The slot leakage inductance is evaluated basing on the definition of magnetic energy stored in the slot.

$$E_s = \frac{1}{2} \cdot \lambda_s \cdot L_{core} \cdot I_s^2 \quad (4.118)$$

Where:

- $\lambda_s$  is the slot leakage coefficient, expressed in H/m.
- $I_s$  is the slot current.

Let's take the slot illustrated in the Fig. 4.20 as model of reference and let's define the average slot width  $w_{ave}$  which ideally divides the useful slot area in two layers with the same area and the same number of conductors  $\frac{N_{cs}}{2}$  and carrying the current  $I_{A1}$  and  $I_{A2}$ , respectively.

Hence,  $w_{ave}$  and the heights  $h_{1s}$  and  $h_{2s}$  of each area are calculated as

$$w_{ave} = \sqrt{\frac{w_{sb}^2 + w_{st}^2}{2}} \quad (4.119)$$

$$h_{1s} = \frac{w_{sb} + w_{ave,s}}{w_{sb} + 2 \cdot w_{ave+w_{st}}} \cdot h_{us} \quad (4.120)$$

$$h_{2s} = h_{us} - h_{1s} \quad (4.121)$$

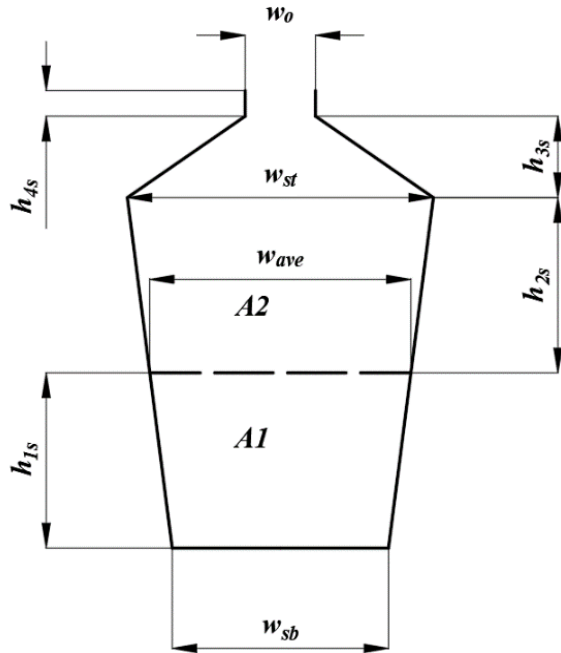


**Figure 4.20:** Slot layers

Including the opening of the slot, the total slot area can be therefore thought as divided in four sub-areas of which heights and bases are known.

Average width of each area and respective deformation coefficient are calculated as follows:

**Table 4.3:** Heights and average width of layers

Area	Average width	Height	Deformation coefficient
Area 1 (A1)	$w_{A1} = \left  \frac{w_{sb} + w_{ave}}{2} \right $	$h_{1s}$	$\alpha_1 = \left  \frac{w_{sb} - w_{ave}}{2 \cdot w_{A1}} \right $
Area 2 (A2)	$w_{A2} = \left  \frac{w_{st} + w_{ave}}{2} \right $	$h_{2s}$	$\alpha_2 = \left  \frac{w_{ave} - w_{st}}{2 \cdot w_{A2}} \right $
Area 3 (A3)	$w_{A3} = \left  \frac{w_o + w_{st}}{2} \right $	$h_{3s}$	$\alpha_3 = \left  \frac{w_{st} - w_o}{2 \cdot w_{A3}} \right $
Area 4 (A4)	$w_{A4} = \left  \frac{w_o + w_o}{2} \right $	$h_{4s}$	$\alpha_4 = 0$

In this particular case, the total magnetic energy stored can be written also as:

$$E_s = E_{A1} + E_{A2} + E_{A1A2} \quad (4.122)$$


---

Where:

$$E_{A1} = \frac{1}{2} \cdot L_{core} \cdot \lambda_1 \cdot I_{A1}^2 \quad (4.123)$$

$$E_{A2} = \frac{1}{2} \cdot L_{core} \cdot \lambda_2 \cdot I_{A2}^2 \quad (4.124)$$

$$E_{A1A2} = L_{core} \cdot \lambda_{12} \cdot I_{A1} \cdot I_{A2} \quad (4.125)$$

Replacing (4.130), (4.131) and (4.132) in the (4.129), it is possible to write

$$E_s = \frac{1}{2} [\lambda_1 \cdot I_{A1}^2 + \lambda_2 \cdot I_{A2}^2 + 2 \cdot \lambda_{12} \cdot I_{A1} \cdot I_{A2}] \cdot L_{core} \quad (4.126)$$

Where  $\lambda_1, \lambda_2$  and  $\lambda_{12}$  represent the slot leakage coefficients measured in H/m.

$$\lambda_1 = K_{t1}(\alpha_1) \cdot \frac{h_{1s}}{w_{A1}} + K_{t0}(\alpha_2) \cdot \frac{h_{2s}}{w_{A2}} + K_{t0}(\alpha_3) \cdot \frac{h_{3s}}{w_{A3}} + K_{t0}(\alpha_4) \cdot \frac{h_{4s}}{w_{A4}} \quad (4.127)$$

$$\lambda_2 = K_{t1}(\alpha_2) \cdot \frac{h_{2s}}{w_{A2}} + K_{t0}(\alpha_3) \cdot \frac{h_{3s}}{w_{A3}} + K_{t0}(\alpha_4) \cdot \frac{h_{4s}}{w_{A4}} \quad (4.128)$$

$$\lambda_{12} = K_{t01}(\alpha_2) \cdot \frac{h_{2s}}{w_{A2}} + 2 \cdot K_{t0}(\alpha_3) \cdot \frac{h_{3s}}{w_{A3}} + 2 \cdot K_{t0}(\alpha_4) \cdot \frac{h_{4s}}{w_{A4}} \quad (4.129)$$

Where the coefficients  $K_{t0}, K_{t1}, K_{t01}$  are given by the equations reporter in Appendix B.

It is important to highlight that in case of rectangular slot, the slot leakage coefficients are integers and they can be obtained with the support of the curves shown Fig. 4.21 by setting  $\alpha = 0$ .

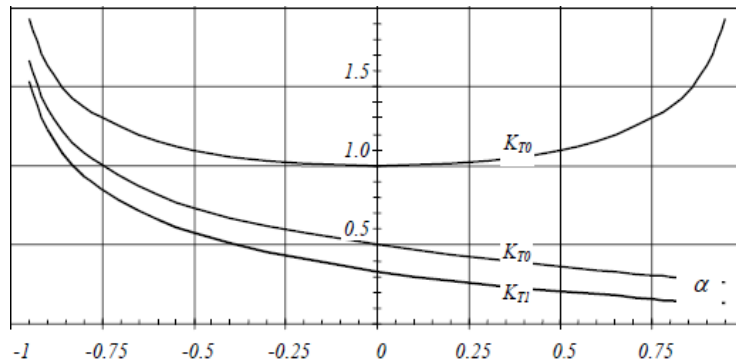


Figure 4.21:  $K_{t0}, K_{t1}, K_{t01}$  [30]

Assuming a reduced winding pitch equal to  $N_{rac}$  slots and assuming layers with the same number of conductors, in according with what has been explained in App. B, the phase leakage inductance can be written as

$$L_{sl} = \mu_0 \cdot \frac{Z_{ph}^2}{p \cdot q} \cdot \frac{\lambda_1 + \lambda_2 + \lambda_{12} \cdot \left(2 - \frac{N_{rac}}{q}\right)}{4} \quad (4.130)$$

#### 4.6.2.3 End-winding leakage inductance

The end-winding leakage inductance is difficult to estimate since it mostly depends on the geometry of connections that could varies case by case. For this reason, designers usually use formulas deriving from experiments or from their own experience.

Therefore, also in the algorithm proposed an empirical formula is used [2].

$$L_{ec} = (0.44 \div 0.52) \cdot \mu_0 \cdot p \cdot \left(\frac{Z_{ph}}{p}\right)^2 \cdot L_{ew} \quad (4.131)$$

#### 4.6.3 Synchronous inductance for FSCW

The equations (4.117), (4.130) and (4.131) are only valid in case of three-phase distributed winding. Instead, analytical methods to calculate the synchronous inductance for FSCW can be found in literature [29]. However, the same equations used for distributed winding are also used for FSCW in this version of the tool by the addition of a correction factor  $k_{corr}$  properly chosen within a range of 1.5-2.

Hence, the synchronous inductances is calculated as

$$L_s = L_{m,1} + L_{leak} \quad (4.132)$$

Where  $L_{leak}$  is the overall leakage inductance, including the air gap inductance which we are not able to calculate.

$$L_{leak} = (L_{sl} + L_{ec}) \cdot k_{corr} + (k_{corr} - 1) \cdot L_{m,1} \quad (4.133)$$

Hence, the air gap leakage inductance can be derived as

$$L_\sigma = L_s - L_{m,1} - L_{sl} - L_{ec} \quad (4.134)$$

#### 4.6.4 Number of conductor in series per phase

As deducible by the respective equations, the stator resistance, synchronous inductance, back EMF and also of the rated current (4.135), are all proportional to the number of conductor in series per phase  $Z_{ph}$ .

$$I_r = \frac{I_s}{N_{cs}} \quad (4.135)$$

Namely, it is possible write

$$E_o = K_1 \cdot Z_{ph} \quad (4.136)$$

$$L_s = K_2 \cdot Z_{ph}^2 \quad (4.137)$$

$$I_r = \frac{K_3}{Z_{ph}^2} \quad (4.138)$$

$$R_s = K_4 \cdot Z_{ph}^2 \quad (4.139)$$

Where

$$K_1 = \frac{\pi}{\sqrt{2}} \cdot f_r \cdot K_{avv} \cdot \Phi_{1p} \quad (4.140)$$

$$K_2 = K_{m,1} + K_{sl} + K_{ec} \quad (4.141)$$

$$K_3 = I_s * \frac{N_c}{3} \quad (4.142)$$

$$K_4 = \rho_{cu} \cdot \frac{L_{ew}}{2 \cdot q \cdot p \cdot A_{cu}} \quad (4.143)$$

Where  $K_{m,1}$  is equal to (4.144) for the distributed winding,

$$K_{m,1} = \frac{3}{2} \cdot \left( \frac{Z_{ph} \cdot K_{avv,h}}{\pi \cdot pp} \right)^2 \frac{\mu_0 \cdot \pi \cdot D_{ag} \cdot L_{core}}{2 \cdot h_{eq}} \quad (4.144)$$

or equal to (4.145) for FSCW.

$$K_{m,1} = k_{corr} \cdot \frac{3}{2} \cdot \left( \frac{Z_{ph} \cdot K_{avv,h}}{\pi \cdot pp} \right)^2 \cdot \frac{\mu_0 \cdot \pi \cdot D_{ag} \cdot L_{core}}{2 \cdot h_{eq}} \quad (4.145)$$

And

$$K_{sl} = \frac{\mu_0}{p \cdot q} \cdot \frac{\lambda_1 + \lambda_2 + \lambda_{12} \cdot \left( 2 - \frac{N_{rac}}{q} \right)}{4} \quad (4.146)$$

$$K_{ec} = (0.44 \div 0.52) \cdot \mu_0 \cdot p \cdot \left( \frac{1}{p} \right)^2 \cdot L_{ew} \quad (4.147)$$

Now, it is possible to write

$$V_r^2 = (R_s \cdot I_r + E_o)^2 + (j\omega L_s \cdot I_r)^2 \quad (4.148)$$

Then,  $Z_{ph}$  can be obtained as

$$Z_{ph} = \frac{V_r}{\sqrt{(K_1 + K_3 \cdot K_4)^2 + (K_2 + K_3)^2}} \quad (4.149)$$

Once  $Z_{ph}$  is determined, all the equivalent circuit parameters can be calculated.

# 5 Prototype design and Finite-Element validation

*Throughout this chapter the design of a SPM synchronous machine design for aeronautical application is presented and then validated by means of FEA in order to compare the analytical results obtained with the SMDT with those obtained by means of FEMM.*

## 5.1 Introduction

In order to validate the results obtained with the sizing tool, a prototype SPM synchronous machine for aeronautical applications has been analytically designed with *SMDT* and then it has been analysed with *FEMM*. In the following sections, firstly some design choices are explained, then the design results are shown and, lastly, analytical results are compared with those obtained with *FEMM* simulations. In particular, critical flux densities are checked and compared with those imposed as constraints and then the motor has been tested in the both no-load and load operating condition in order to compare back-EMF and torque at the synchronous speed with the target values.

### 5.1.1 Design specifications and target data

The motor has to be directly connected to a low-pressure turbine, whose shaft's rated speed is 2400 rpm. On basis of this value and the theoretical aspects introduced in the previous chapters, the number of poles and rated frequency have been chosen equal to 28 and 560 Hz, respectively. With regard to the winding layout, FSCW has been chosen as technology and the number of slots per pole per phase has been set equal to 0.286, in order to obtain a compact solution and reduced

---

winding losses. As result of these choices, stator with 24 slots and fundamental winding factor equal to 0.966 are obtained in according with the table (2.1).

The motor must be able to provide 40 Nm at the synchronous speed that corresponds to the maximum value of torque achieved when the rated current is all applied along the axis in quadrature.

The cooling method basically consists in a fan generating air flow that passes through some inlet holes and gets out through an outlet window by crossing the air gap, as Fig. 5.1 illustrates. Because of this unconventional cooling system and in order to minimize the cogging torque, the air gap height has been chosen equal to 2 mm. Actually, to make the cooling easier, higher values of air gap height and a lower number of poles would be preferred. However, the air gap height and number of poles have been properly chosen in order to increase the rotor losses (ideally achievable by decreasing the air gap height and by increasing the number of poles), hence allow further laboratory analysis about the machine, but also seeking a trade-off with the iron losses limitation. With regard to stress indexes is possible refer to what reported in previous chapters.

In the table 5.1 are shown the design specifications.

**Table 5.1:** Design specifications

Rated data	
Phase rated voltage	119.4 V
Rated Torque	40 Nm
Rated Frequency	560 Hz
N. poles	28
Geometry constraints	
Air gap height	2
Shaft diameter	178 mm
Ratio L/D	0.165
Slot shape	Rectangular
Slot opening	2 mm
Link slot height	3 mm
Edge slot height	3 mm
Slot fill factor	0.456

Winding properties	
Type of winding	FSCW – single layer
N. slots per pole and phase	0.286
Reduced pitch as n. of slot	0
Fundamental winding factor	0.966
Operating temperature	150 °C
Stress indexes	
Teeth flux density	1.27 T
Stator yoke flux density	0.67 T
Rotor yoke flux density	0.94 T
Current density	4 A/mm <sup>2</sup>
K <sub>s</sub> ·J	1500 A <sup>2</sup> /cm/mm <sup>2</sup>

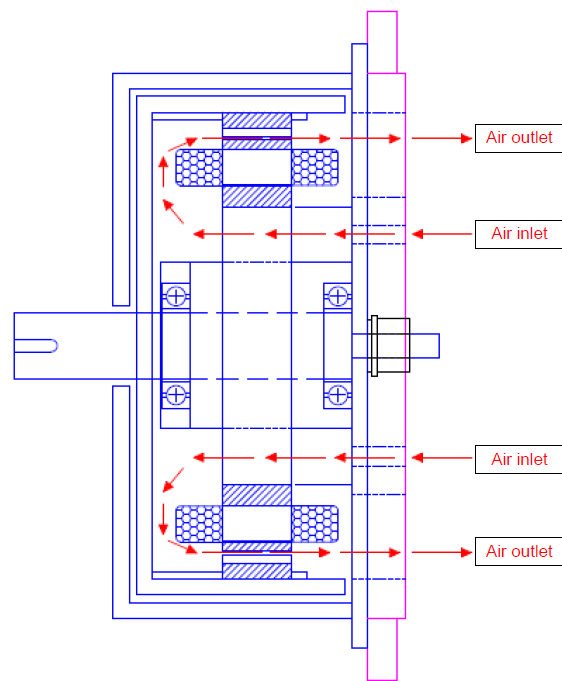


**Figure 5.1:** Air flowing inside the motor [32]

## 5.1.2 Material properties

### 5.1.2.1 Winding

Copper is used as conductor material and Litz wires are adopted in order to limit the skin effect and proximity effect, as the motor is used for high-frequency applications. In this kind of wires, each strands is electrically insulated from others.

### 5.1.2.2 Core

In aerospace applications, high values of power density are required. Therefore, soft magnetic materials with high saturation are usually preferred. Cobalt-iron alloy represents one of the best materials in terms of saturation and specific losses, since are comparable with those of the silicon-iron alloys, which have the lowest ones.

However, cobalt-iron alloy are made up of a high content of cobalt, which makes these type of alloy really expensive. For this reason, non-oriented thin electrical silicon steel has been chosen for this project. In particular, the material selected is *COGENT NO20*, whose saturation is remarkably lower than the *VACOFLUX 50* one, a Co-Fe alloy with 50 % cobalt content. However, specific losses are comparable at rated frequency, as Fig. 5.2 illustrates.

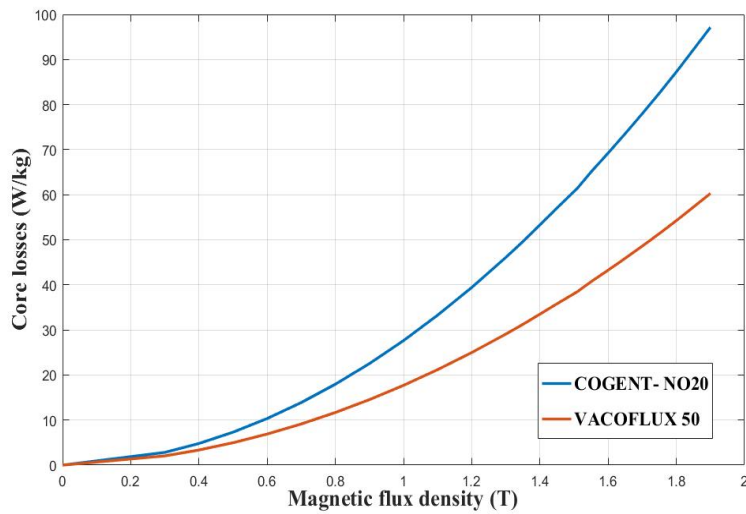
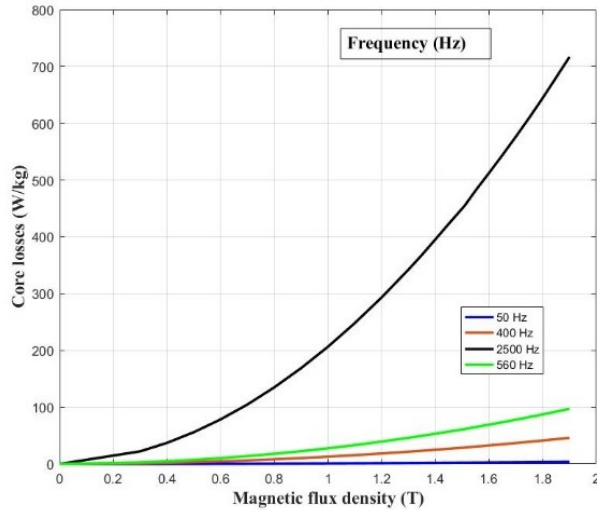


Figure 5.2: COGENT NO20 and VACOFLUX 50 specific losses at 50 Hz

To obtain the specific losses of *COGENT NO20* at the rated frequency, measures at 50, 400 and 2500 Hz provided by manufacturer have been interpolated at the rated frequency equal to 560 Hz, as shown in Fig 5.3.



**Figure 5.3:** COGENT NO20 specific losses at different frequencies

The Fig. 5.4, instead, shows the B-H curve of *COGENT N20*. The stacking factor is assumed equal to 0.93.

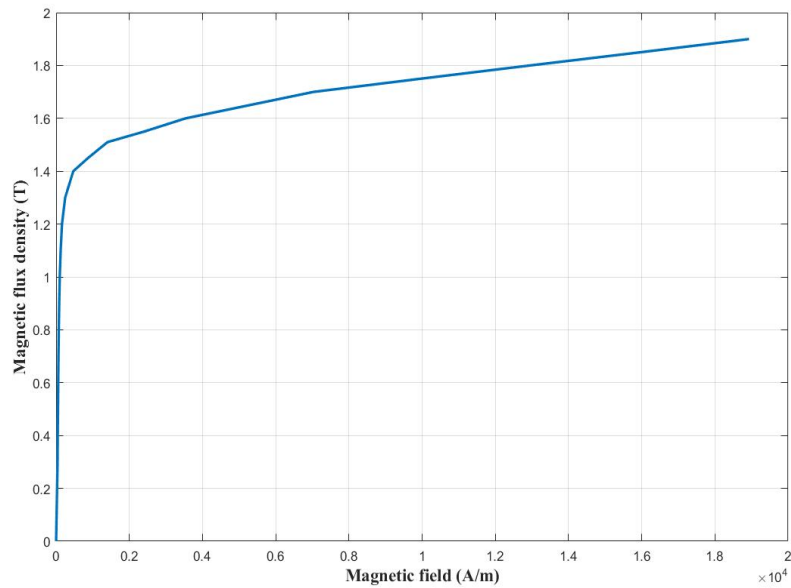


**Figure 5.4:** B-H curve of COGENT NO20

---

### 5.1.2.3 Magnet

With the considerations introduced in the Chapter 2 in mind, the NdFeB N25EH magnet has been chosen. It is characterized by these properties:

**Table 5.2:** N25EH properties

Magnet type	N25EH
Magnetic remanence ( $B_r$ )	0.98
Coercive force ( $H_c$ )	732-764 kA/m
Relative permeability ( $\mu_r$ )	1.02
Temperature coefficient of $B_r$	-0.11 %/°C
Temperature coefficient of $H_c$	-0.60 %/°C
Working temperature ( $T_{magn}$ )	≤200 °C

In the design procedure the temperature effect at load operating operation has been considered. Since the rotor is external and winding temperature is assumed equal to 150 °C, therefore to assume 120 °C as magnet operating temperature is a reasonable choice. Each magnet has a height equal to 6 mm and angular polar pitch equal to 160°.

In the table 5.3, the specifications of the materials used are shown.

**Table 5.3:** Materials used properties

Magnet: NdFeB N25EH	
Operating temperature	120°
Magnetic remanence	0.9 T
Specific weight	7400 kg/m <sup>3</sup>
Magnet height	6 mm
Magnet arc	160°
Iron: COGENT NO20	
Lamination stack coefficient	0.93
Specific weight	8120 kg/mm <sup>3</sup>

### 5.1.3 Design results

Once input data have been defined, the design procedure starts and provides the results of the project. In the table 5.4, lamination geometry dimensions are illustrated, whereas in Fig. 5.5 the physical model is shown.

**Table 5.4:** Prototype dimensions

<b>Main dimensions</b>	
Stator internal diameter	178 mm
Stator external diameter	264 mm
Stator yoke height	14 mm
Rotor internal diameter	280 mm
Rotor external diameter	300 mm
Rotor yoke height	10 mm
Air gap radius	133 mm
Active length	44 mm
<b>Tooth dimensions</b>	
Tooth head thickness	21 mm
Tooth bottom thickness	15 mm

<b>Slot dimensions</b>	
Slot opening	4 mm
Slot head width	12 mm
Slot bottom width	12 mm
Slot edge height	3 mm
Slot link height	3 mm
Slot useful height	23 mm
Slot total height	29 mm
Slot useful area	274.6 mm <sup>2</sup>

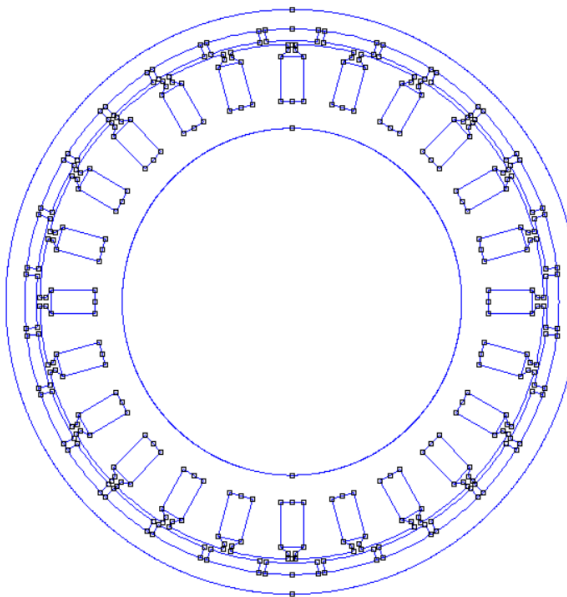


**Figure 5.5:** FEMM model of the machine.

In the table 5.5 resulting winding properties, weights, volumes, losses, equivalent circuit parameters and inductance are shown.

**Table 5.5:** Prototype additional features

Winding	
Number of conductors in series per phase	128
Equivalent wire cross-section	7.8 mm <sup>2</sup>
Winding total length	181 mm
End-winding length	47 mm
Axial end-winding length	22.5 mm
Total axial winding length	88.8 mm

Weights	
Laminations weight	10.4 kg
Stator winding weight	2.4 kg

Magnets weight	1.5 kg
Total weight	14.4 kg

Volumes	
Materials volume	1.8 dm <sup>3</sup>
End-winding room	0.2 dm <sup>3</sup>
Active room	2.2 dm <sup>3</sup>
Required room	4.1 dm <sup>3</sup>

Equivalent circuit	
Phase rated voltage	119.4 V
No-load voltage	105.8 V
Rated current	31 A
Stator resistance	0.039 Ω
Phase inductance	0.4808 mH

Inductance	
Fundamental inductance	0.0342 mH
Slot inductance	0.1993 mH
End-winding inductance	0.0152 mH
Leakage inductance	0.4466 mH
Airgap inductance	0.2321 mH

Factor	
Slot fill factor	0.456
Winding factor	0.966
Carter's coefficient	1.034

#### 5.1.4 FEMM analysis

By following the simulation setups introduced previously, the machine with dimensions described in the table 5.1, 5.4 and 5.5 is analysed.

---

#### 5.1.4.1 No-load operation

One of the most important target of no-load operating condition simulation is to investigate the maximum values of flux density obtained in the teeth, yokes and air gap in order to compare them with those imposed as constraints, as already said before. In the Fig. 5.6, obtained flux density distribution by FEMM is shown.

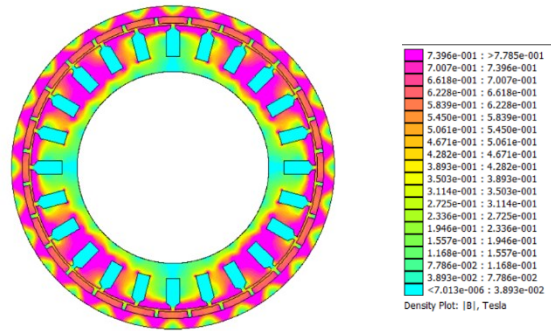


Figure 5.6: Magnetic field distribution

#### Air gap flux density

The air gap flux density of one pole pair and of half motor are illustrated in Fig.7 and Fig.8. As can be seen, the Fig. 5.7 exhibits a waveform pretty different with respect to a rectangular waveform. The slotting effect is remarkable resulting in a great harmonic content, shown in Fig. 5.9

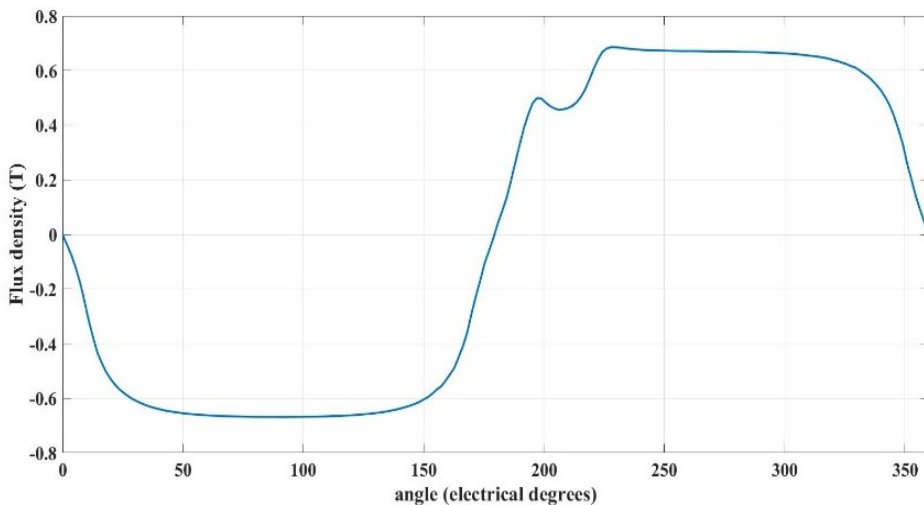
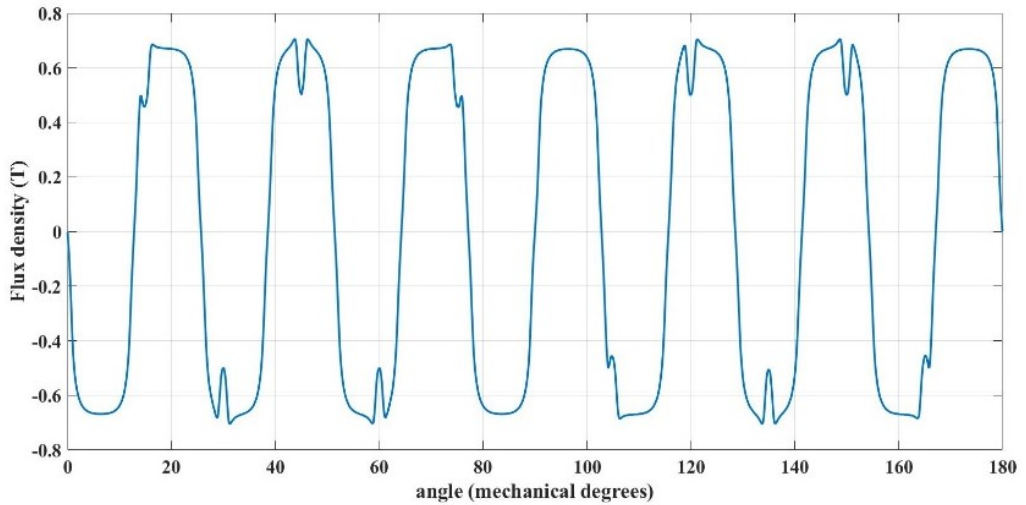
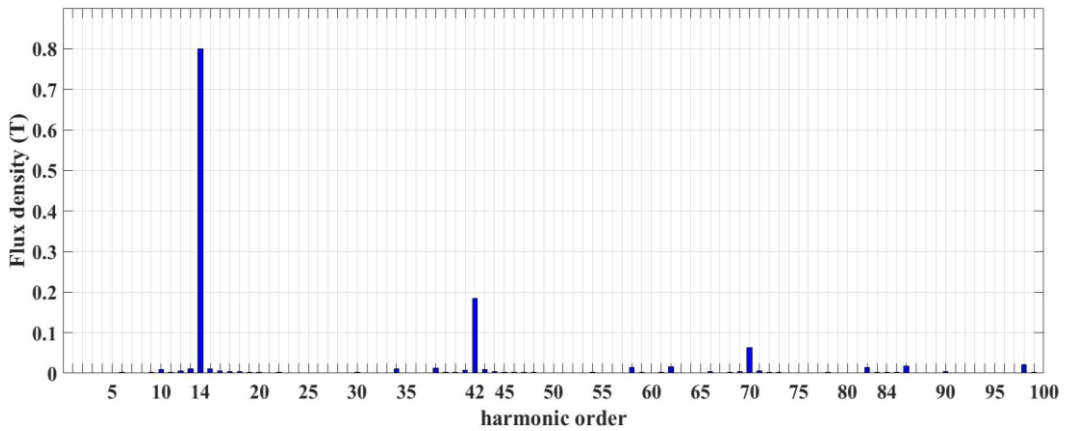


Figure 5.7: Air gap flux density along on pole pair



**Figure 5.8:** Air gap flux density along half motor



**Figure 5.9:** Harmonic content of the air gap flux density

In the table 5.6 the peak value of the air gap flux density and its fundamental harmonic are compared with those expected with the tool. It can be observed that the fundamental amplitude obtained with FEMM is lower than one obtained with *SMDT*. It is probably due to the fact that the flux density waveform is considered perfectly rectangular in the algorithm during the design procedure. On the contrary, it is possible noticed that the waveform shown in Fig. 5.7 presents a weakening in proximity of the magnet's tips, caused by magnetic field lines that do not flow inside the teeth so resulting in flux leakage, as the Fig. 5.10 illustrates.

**Table 5.6:** Peak value of the airgap flux density

	Tool	FEMM
Air gap flux density	0.66 T	0.69 T
Fundamental air gap flux density	0.83 T	0.8 T

The Fig. 5.10 also shows the presence of the zigzag flux, namely the flux that flows from a pole to another pole through the tooth tip. This happens at certain rotor positions because of the similar number of slots and poles that characterizes the machines with FSCW. As can be seen, the tangential component of the flux density is maximum, while the radial component is minimum.

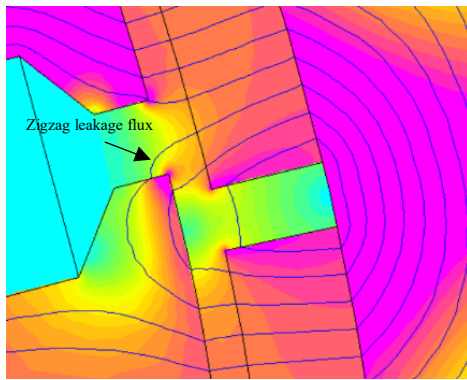


**Figure 5.10:** Zigzag leakage flux

### Yokes and teeth flux density

The table 5.7 shows the maximum values of flux densities imposed as constraints for yoke and teeth and those obtained with FEA. Of course, magnetic saturation in the critical points, such as in the teeth's tips, has been taken into account in the evaluation of the values.

**Table 5.7:** Maximum values of flux density in the critical points of the machine

	Tool	FEMM	$\Delta\%$
Teeth	1.27 T	1.3 T	- 2.3 %
Stator yoke	0.67 T	0.69 T	- 3 %
Rotor yoke	0.94 T	0.97 T	- 3 %

Anyway, the percentage errors shown in the table 5.7 point out a reasonable trade-off between the constraints defined for designing and the actual values obtained with FEMM analysis. Furthermore, it is important to remark that, although all FE values are greater, they are not critical

---

in terms of magnetic saturation since low stress indexes have been chosen in accordance with the pole number choice about the iron losses limitation.

### Back-EMF

In the Fig. 5.11 the induced voltages and phase-A harmonic spectrum are shown. In this case the motor is forced to rotate at 2400 rpm, namely the rated speed, for one electrical revolution. As expected, only the first and third harmonic are the most remarkable, whereas the others can be considered negligible. In table 5.8, the obtained rms-value of the back-EMF is compared with the expected one by *SMDT*.

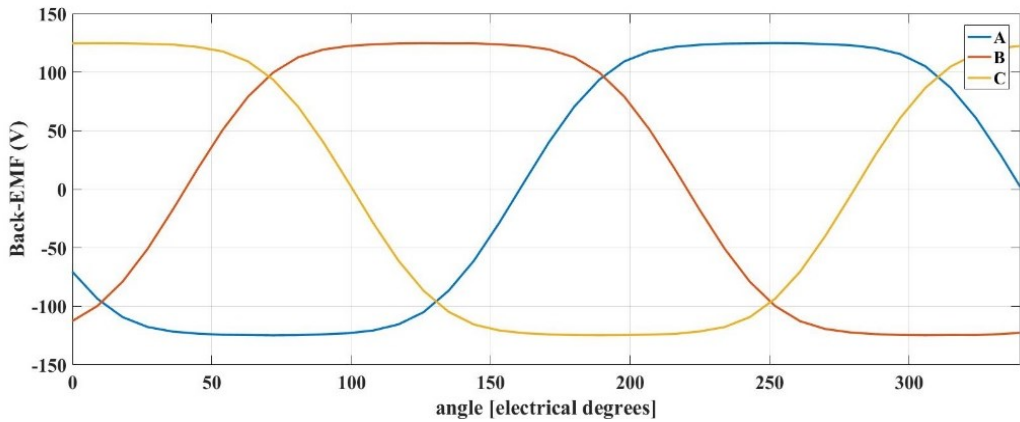


**Figure 5.11:** Back-EMF obtained with FEA

**Table 5.8:** Comparison between tool and FEMM resulting back-EMF.

	Tool	FEMM	$\Delta\%$
Back – EMF (rms)	105.8 V	104.4 V	+ 1.3 %

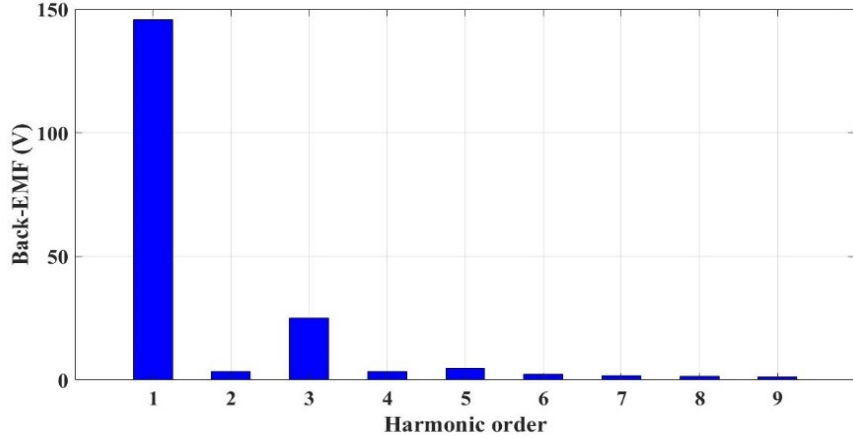


Figure 5.12: Harmonic spectrum of the back-EMF

### Cogging torque

The Fig. 5.13 shows the cogging torque waveform along one pole pair. For this motor, the total number of periods calculated with the (2.42) is 168, then we expect 12 periods along one pole pair, being 14 the number of pole pairs. This can be proved with the harmonic spectrum shown in Fig. 5.14, from which is possible noticed that the harmonic order with the maximum amplitude is equal to the number of cogging torque periods along one pole pair.

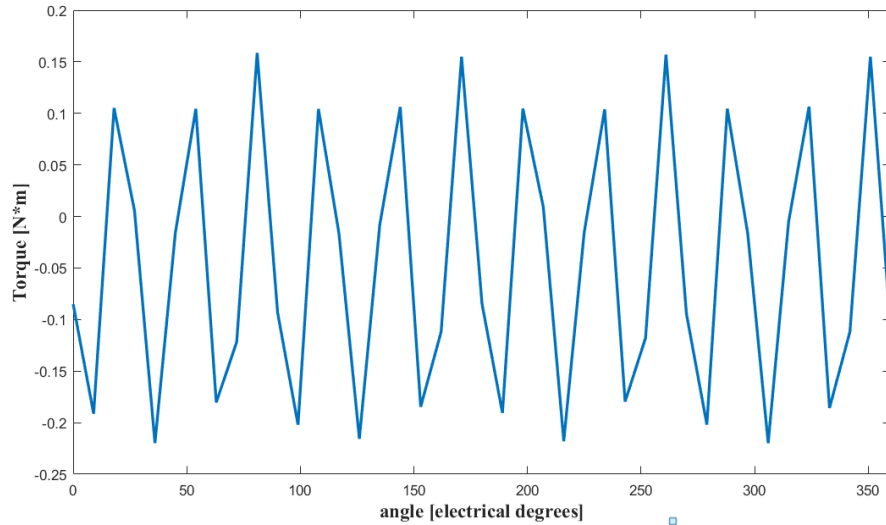
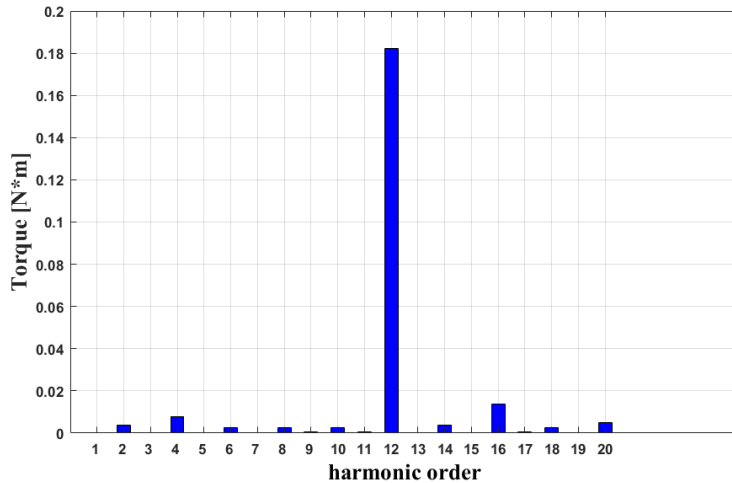


Figure 5.13: Cogging torque along one pole pair

---



**Figure 5.14:** Harmonic spectrum of the cogging torque along one pole pair

The amplitude of the 12<sup>th</sup>- harmonic is equal to 0.19 Nm, whereas the cogging torque periodicity is equal to  $360/168 = 2.14^\circ$ .

#### 5.1.4.2 Load working operation

##### Torque at synchronous speed

The Fig. 5.15 shows the torque performed by the machine when it is rotated of an electrical round. The average torque performed is 38.1 Nm with a ripple equal to 1.8 Nm peak-to-peak. The table 5.9 shows up the comparison between the target torque and the torque obtained with the FEA.

**Table 5.9:** Comparison between the obtained values of the torque

	Target	FEMM	$\Delta\%$
Torque	40 Nm	38.1 Nm	+ 5 %

In the table 5.10, instead, cogging torque and the overall torque ripple are compared to the mean value of the resulting torque by FEMM.

**Table 5.10:** Cogging torque and torque ripple compared to the average torque.

	Amplitude	$\Delta\%$
Cogging torque	0.19 Nm	0.5 %
Torque ripple	1.8 Nm	4.7 %

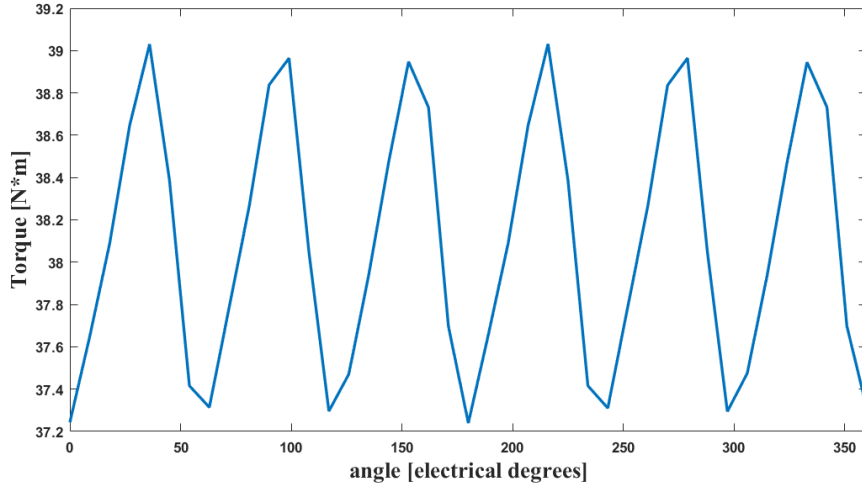


**Figure 5.15:** Torque at the synchronous speed

### Field-weakening working operation

As explained in the Chapter 2, SPM machine are often preferred for applications needing wide constant-power speed range due to their higher leakage inductance. To evaluate the flux-weakening capability of this machine we can calculate the characteristic current.

Being:

- $E_o = 104.4$  the back-EMF.
- $\omega_b = 2\pi 560$  rad/s, the base speed.

Then, the rms-value of magnet flux linkage is

$$\lambda_m = \frac{E_o}{\omega_b} = \frac{104.4}{2\pi 560} = 0.0297 \text{ Wb} \quad (5.1)$$

This value can be also obtained by calculating the rms-value of the resulting flux linkage curve from Finite-Element analysis at no-load. The Fig. 5.16 shows the magnet flux linkage with the phase A.

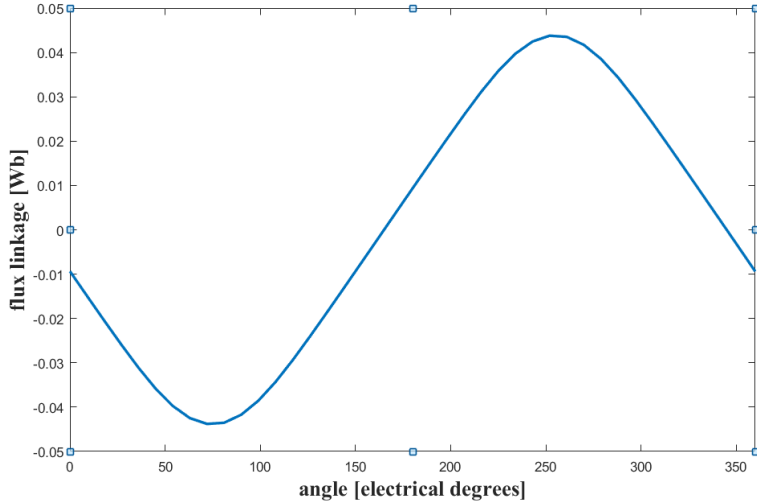


**Figure 5.16:** Magnet flux linkage

The resulting rms-value is 0.0294 Wb. Therefore, by using the value of phase inductance obtained by analytical design, the rms-value of characteristic current is equal to

$$I_{ch} = \frac{\lambda_m}{L_b} = \frac{0.0297}{0.4808} = 61.7 \text{ A} \quad (5.2)$$

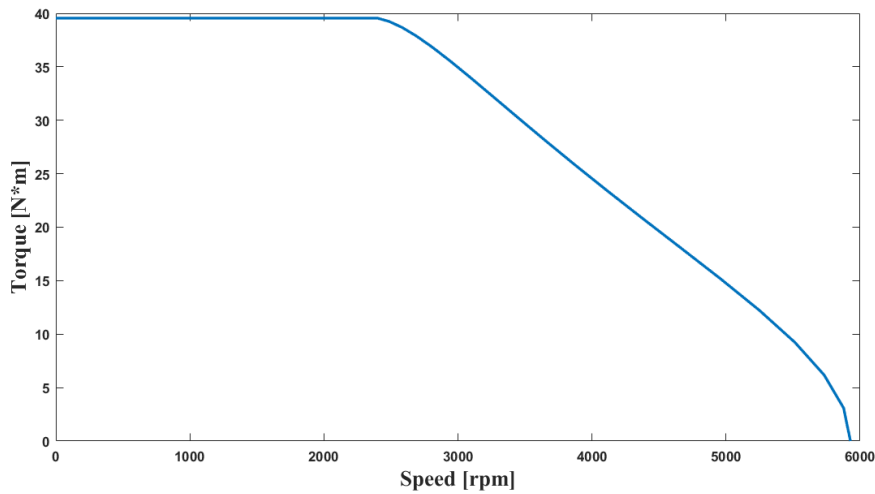


**Figure 5.17:** Torque versus speed

Being  $I_{ch} > I_r$ , the flux-weakening capability is not optimal and the constant-power speed range is not infinite.

This can be shown up by having a look at the curve of torque and power shown in Fig. 5.17 and 5.18, respectively.

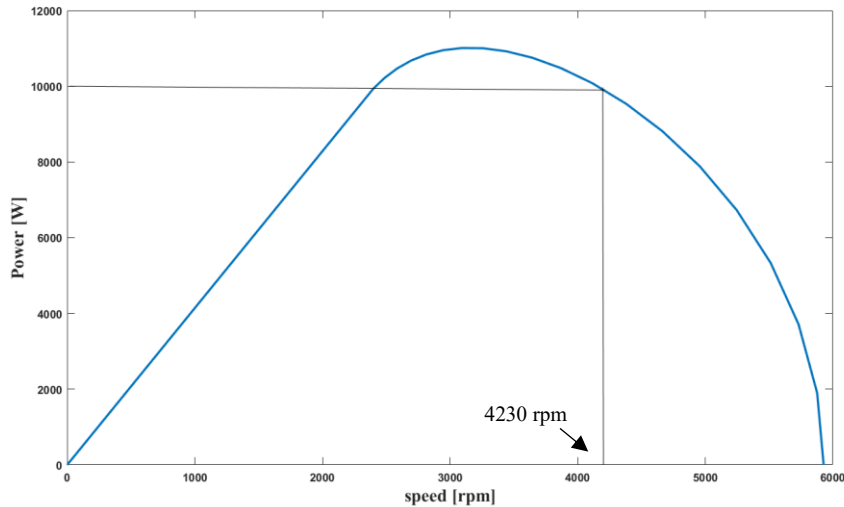


**Figure 5.18:** Power versus speed

The speed for which the base power is maintained is about 4230 rpm, while the maximum speed capability is 5928 rpm against the theoretical value calculated with the (2.49) and equal to 6248 rpm.

# 6 Conclusions and future work

## 6.1 Conclusions

The design of a new SPM machine with a geometry different from standard solutions may be a difficult task and time-consuming if carried out with the only support of analytical or FEM commercial software, such as SPEED or CEDRAT Flux®. For this reason, *SMDT*, a design tool to make designing faster, has been developed and through this thesis presented. *SMDT* is based on analytical and self-consistent equations and it allows to have a preliminary sizing of the machine. Basically, once some design specifications are defined by the user, the algorithm progressively increases the motor dimensions, diameters and active length, until the target torque is achieved, according to the material solicitations imposed as constraints at the beginning of the designing. *SMDT* outputs the lamination dimensions, materials weight and volume, equivalent circuit parameters and rated data. *SMDT* also provides an additional tool for electromagnetic Finite-Element analysis and results validations in terms of rated torque, back-EMF and constant power-range.

A SPM motor for aeronautical applications has been taken as case study to validate the algorithm implemented, then, some electromagnetic analysis have been performed to highlight the tool's potential and validate the results. The results obtained with *SMDT*, when compared with those obtained through the tool, are very satisfactory, as the percentage differences on induced voltage and torque are within a range of 1-5 %. Satisfactory results are also obtained in terms of resulting magnetic stresses in the yokes, teeth and air gap. Therefore, the obtained results allows to state that *SMDT* is a very useful tool for obtaining a preliminary sizing of the machine. However, the project is not the definitive one, as it needs to be optimized and improved and, in this regard, FEMs surely provides the necessary support.

---

## 6.2 Future work

Hereby, some suggestions on possible future work are presented:

- In order to obtain a higher flexibility on using *SMDT*, the implementation of a function able to design machines with FSCW with double layer without acting on source code is deeply suggested.
- *FEA-t* does not allow to set the winding layout as designer prefers, above all for FSCW motors. In fact, in this cases, the phases disposition into the slots has to be directly defined in the source code within the function “*Winding\_structure*”. Moreover, double layer for both winding types it cannot be modelled on FEMM. An additional function which allows to set and model machines with the user’s winding layout could be implemented.
- Machines with skewed stator perform a lower cogging torque. An improvement in *SMDT* and *FEA-t* algorithm able to design and analyse machines with skewed stator is suggested.
- *FEA-t* provides several FE analysis, but the simulation properties, such as the mesh size, cannot be set as designer prefers. Therefore, an option allowing to set the simulations properties and perform additional analysis, like *d-axis* inductance or iron, mechanical and magnet losses, could be added and implemented.
- *SMDT* could be integrated with an optimization algorithm which takes in account of weight and costs.

# Appendix A: Calculation of magnetizing inductance

Let's assume to have a regular three-phase distributed winding fed by a symmetrical three-phase system of sinusoidal currents.

$$\begin{aligned} i_1(t) &= \hat{I} \cdot \cos(\omega t) \\ i_2(t) &= \hat{I} \cdot \cos\left(\omega t - \frac{2\pi}{3}\right) \\ i_3(t) &= \hat{I} \cdot \cos\left(\omega t - \frac{4\pi}{3}\right) \end{aligned} \quad (\text{A.6.1})$$

Assuming that the iron permeability is infinite, hence the core influence is neglected, then the three-phase magneto-motive force (MMF) rotating along the air gap is given by the following relation:

$$A_3(\alpha, t) = \frac{3}{2} \cdot \hat{I} \sum_{h=6k+1} \frac{Z_{ph} \cdot K_{avv,h}}{h \cdot \pi \cdot pp} \cdot \sin(hpp\alpha - \omega t) \quad (\text{A.6.2})$$

Where the amplitude of the  $h^{th}$  order harmonic can be expressed as

$$A_{3h} = \frac{3}{2} \cdot \frac{Z_{ph} \cdot K_{avv,h}}{h \cdot \pi \cdot pp} \cdot \hat{I} \quad (\text{A.6.3})$$

The peak value of the  $h^{th}$  order harmonic of the flux density generated along the air gap can be hence expressed as

$$B_{3h} = \frac{3}{2} \cdot \frac{Z_{ph} \cdot K_{avv,h}}{h \cdot \pi \cdot pp} \cdot \frac{\mu_o}{h_{eq}} \cdot \hat{I} \quad (\text{A.6.4})$$

Where  $h_{eq}$  is the equivalent air gap height defined in (4.2). It is important to remark that the Carter coefficient  $K_{car}$  is an average value, but to be more rigorous the harmonic Carter coefficient  $K_{c,h}$  should be taken into account, whose value is different for each harmonic of flux density, however this is disregarded. The flux leakage with the phase 1 can be hence written as

$$\lambda_1(t) = \frac{3}{2} \cdot \hat{I} \cdot \sum_{h=6k+1} \left( \frac{Z_{ph} \cdot K_{avv,h}}{h \cdot \pi \cdot pp} \right)^2 \cdot \frac{1}{\mathfrak{R}_t} \cdot \cos(\omega t) \quad (\text{A.6.5})$$

Where  $\mathfrak{R}_t$  is the equivalent air gap reluctance.

$$\mathfrak{R}_t = \frac{h_{eq}}{\mu_o \cdot \pi \cdot D_{ag} \cdot L_{core}} \quad (\text{A.6.6})$$

With this theoretical considerations in mind, the main inductance of phase 1 can be obtained as

$$L_m = \frac{\lambda_1}{i_1} \quad (\text{A.6.7})$$

It is possible to state that equation (A.7) is also valid for the other winding phases, considering the respective current.

Namely,

$$L_m = \frac{\lambda_1}{i_1} = \frac{\lambda_2}{i_2} = \frac{\lambda_3}{i_3} \quad (\text{A.6.8})$$

Therefore,

$$L_m = \frac{3}{2} \cdot \sum_{h=6k+1} \left( \frac{Z_{ph} \cdot K_{avv,h}}{h \cdot \pi \cdot pp} \right)^2 \cdot \frac{1}{\mathfrak{R}_t} \quad (\text{A.6.9})$$

## Appendix B: Calculation of slot leakage inductance

The slot leakage inductance evaluation is made by studying the magnetic energy stored into the slot. With reference to Fig. B.1, the presence of a massive conductor placed into a slot and infinite iron permeability are assumed. Let's assume to divide the slot in several layers trapezoidal-shaped whose elementary height  $\Delta h$  and the upper and lower base,  $w_1$  and  $w_2$ , respectively, are well-known for each one of them.

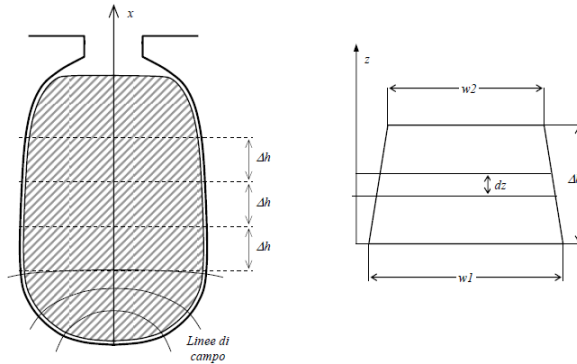


**Figure B.1:** Trapezoidal slot and its subdivisions.

Considering one layer and by introducing the coordinate  $x$ , the width of the slot is given by the function  $w(x)$ :

$$w(x) = w_{ave} \cdot \left[ (1 - \alpha) + 2 \cdot \alpha \cdot \frac{x}{\Delta h} \right] \quad (\text{B.1})$$

Where  $w_{ave}$  and  $\alpha$  are the average layer width and the slope of the layer wall, respectively.

$$w_{ave} = \frac{w_b + w_t}{2} \quad (B.2)$$

$$\alpha = \frac{w_2 - w_1}{2 \cdot w_{ave}} \quad (B.3)$$

The coefficient  $\alpha$  is within a range of [-1,1]:

- Positive values of  $\alpha$  occur when the layer has its top width greater than bottom width, vice versa for negative values.
- “0” occurs when the layer is rectangular-shaped.
- “-1” or “+1” occurs when the layer degenerates into a triangular layer, for example in the triangular slots.

The magnetic field at the  $x$ -coordinate is given by:

$$H(x) = \frac{I_o + \int_0^x J \cdot w(\zeta) \cdot d\zeta}{w(x)} \quad (B.4)$$

Where  $I_o$  refers to the total current below the layer considered. Replacing (B.1) in (B.4), magnetic field expression becomes

$$H(\xi) = \frac{I_o + I_1[(1 - \alpha) + \alpha \cdot \xi^2]}{w_{ave} \cdot [(1 - \alpha) + 2 \cdot \alpha \cdot \xi]} \quad (B.5)$$

Where  $I_1$  is the current flowing through the layer considered,

$$I_1 = J \cdot \Delta h \cdot w_{ave} \quad (B.6)$$

And  $\xi$  is

$$\xi = \frac{\Delta h}{w_{ave}} \quad (B.7)$$

The magnetic energy stored into the slot can be generally written as

$$E_s = \frac{1}{2} \cdot L_{core} \cdot \mu_o \cdot \int_0^h H(x)^2 \cdot w(x) \cdot dx \quad (B.8)$$

Replacing (B.5) into (B.8), the previous equation can be rewritten also as

$$E_s = \frac{1}{2} \cdot L_{core} \cdot \mu_o \cdot \frac{\Delta h}{w_{ave}} \int_0^1 \frac{(I_o + I_1[(1-\alpha) + \alpha \cdot \xi^2])^2}{[(1-\alpha) + 2 \cdot \alpha \cdot \xi]} d\xi \quad (\text{B.9})$$

Which, if solved, becomes:

$$E_s = \frac{1}{2} \cdot L_{core} \cdot \mu_o \cdot \frac{\Delta h}{w_{ave}} [K_{t0}(\alpha) \cdot I_o^2 + K_{t1}(\alpha) \cdot I_1^2 + 2 \cdot K_{t01}(\alpha) \cdot I_o \cdot I_1] \quad (\text{B.10})$$

Where the coefficients  $K_{t0}, K_{t1}, K_{t01}$  are given by the following equations:

$$K_{t0} = \frac{1}{2\alpha} \log \left( \frac{1+\alpha}{1-\alpha} \right) \quad (\text{B.11})$$

$$K_{t1} = \frac{1}{16\alpha^2} \left( \frac{(\alpha-1)^4}{2\alpha} \log \left( \frac{1+\alpha}{1-\alpha} \right) - \alpha^2 + 4\alpha - 1 \right) \quad (\text{B.12})$$

$$K_{t01} = \frac{1}{4\alpha} \left( 1 - \frac{(\alpha-1)^2}{2\alpha} \log \left( \frac{1+\alpha}{1-\alpha} \right) \right) \quad (\text{B.13})$$

### Full pitch winding

In case of full-pitched winding, the one-phase magnetic energy stored in the slots can be calculated with the equations (B.14) and (B.15):

$$E_{s,w} = p \cdot q \cdot \left( \frac{1}{2} \cdot \lambda_s \cdot L_{core} \cdot I_s^2 \right) \quad (\text{B.14})$$

$$E_{s,w} = \frac{1}{2} \cdot L_{sl} \cdot I_i \quad (\text{B.15})$$

Where

$$I_s = \frac{Z_{ph}}{p \cdot q} \cdot I_i \quad (\text{B.16})$$

Therefore, the slot leakage inductance is given by

$$L_{sl} = \frac{Z_{ph^2}}{p \cdot q} \cdot \lambda_s \cdot L_{core} \quad (\text{B.17})$$

### Double layer with reduced pole pitch

Assuming that the layers carry the current  $I_{L1}$  and  $I_{L2}$ , respectively, then the magnetic energy stored in the slot can be evaluated with the following formula:

$$E_L = E_{L1} + E_{L2} + E_{L1L2} \quad (\text{B.18})$$

Where

$$E_{L1} = \frac{1}{2} \cdot L_{core} \cdot \lambda_1 \cdot I_{L1}^2 \quad (\text{B.19})$$

$$E_{L2} = \frac{1}{2} \cdot L_{core} \cdot \lambda_2 \cdot I_{L2}^2 \quad (\text{B.20})$$

$$E_{L1L2} = L_{core} \cdot \lambda_{12} \cdot I_{L1} \cdot I_{L2} \quad (\text{B.21})$$

Assuming a three-phase symmetrical system of sinusoidal currents, it is possible to write for a generic layer:

$$i_{L,1} + i_{L,2} + i_{L,3} = 0 \quad (\text{B.22})$$

$$i_{L,1} \cdot i_{L,2} + i_{L,2} \cdot i_{L,3} + i_{L,1} \cdot i_{L,3} \quad (\text{B.23})$$

$$= -\frac{1}{2} \cdot (i_{L,1}^2 + i_{L,2}^2 + i_{L,3}^2)$$

$$i_{L,1} + i_{L,2} + i_{L,3} = 0 \quad (\text{B.24})$$

In case of winding with a reduced pitch of  $N_{rac}$ , only  $p \cdot (q - N_{rac})$  slots carry the same phase current in the both layers, whereas layers carry different phase currents in  $q - N_{rac}$  slots.

Then, one-phase overall slot magnetic energy can be also expressed in this form

$$\begin{aligned} E_{s,w} = L_{core} & \left[ \frac{1}{2} \cdot p \cdot (q - N_{rac}) \cdot (\lambda_1 + \lambda_2 + 2 \cdot \lambda_1 \cdot \lambda_2) \cdot (i_{L,1}^2 + i_{L,2}^2 + i_{L,3}^2) \right. \\ & + \frac{1}{2} \cdot p \cdot N_{rac} \cdot (\lambda_1 + \lambda_2) \cdot (i_{L,1}^2 + i_{L,2}^2 + i_{L,3}^2) - \frac{1}{2} \cdot p \cdot N_{rac} \\ & \left. \cdot 2 \cdot \lambda_{1,2} \cdot (i_{L,1} \cdot i_{L,2} + i_{L,2} \cdot i_{L,3} + i_{L,1} \cdot i_{L,3}) \right] \end{aligned} \quad (\text{B.25})$$

Simplifying, (B.25) can be also written as

$$E_{s,w} = \frac{1}{2} \cdot p \cdot q \cdot L_{core} \cdot \left( \lambda_1 + \lambda_2 + \lambda_{12} \cdot \left( 2 - \frac{N_{rac}}{q} \right) \right) \quad (\text{B.26})$$

$E_{s,w}$  can be alternatively written as

$$E_{s,w} = \frac{1}{2} \cdot L_{sl} \cdot (i_1^2 + i_2^2 + i_3^2) \quad (\text{B.27})$$

From which is possible to obtain  $L_{sl}$ .

$$L_{sl} = \mu_o \cdot \frac{Z_{ph}^2}{p \cdot q} \cdot \frac{\lambda_1 + \lambda_2 + \lambda_{12} \cdot \left( 2 - \frac{N_{rac}}{q} \right)}{4} \quad (\text{B.28})$$

# Bibliography

- [1] D. HANSLEMAN, Brushless permanent magnet motor design, Lebano, Ohio: Magna Physics Publishing, Motor Division of Fisher Technology, 2006.
  - [2] A. BOGLIETTI, A. CAVAGNINO and M. LAZZARI, “Computational Algorithms for Induction-Motor Equivalent Circuit Parameter Determination: Resistances and Leakage Reactance”, *IEEE Trans Ind. Electron.*, vol. 58, no. 9, pp. 3723-3731, 2011.
  - [3] R. AMENDOLA, *Calcoli magnetici su macchine elettriche a magneti permanenti*, Torino: Bachelor's thesis, Politecnico di Torino,, 2013.
  - [4] I. BOLDEA and S. A. NASAR, The induction machines design handbook, Second ed., CRC Press, 2009.
  - [5] A. M. EL-REFAIE, “Fractional-Slot Concentrated-Winding Synchronous Permanent Magnet Machines: Opportunities and Challenges”, *IEEE Trans. Ind. Electron.*, vol. 57, no. 1, pp. 107-121, 2010.
  - [6] J. CROS and P. VIAROUGE, “Synthesis of high performance PM motors with concentrated winding”, *IEEE Trans Energy Convers.*, vol. 17, no. 2, pp. 248-253, 2002.
  - [7] M. V. CISTELECAN, M. POPESCU and M. POPESCU, “Study of the number of slots/pole combinations for low speed permanent magnet synchronous generator”, *IEEE Int. Electric machines and Drives Conf.*, vol. 2, pp. 1616-1620, 2007.
  - [8] F. MEIER and J. SOULARD, “PMSMs with Non-Overlapping Concentrated Windings: Design Guidelines and Model References”, *Ecologic Vehicles and Renewable Energies, Monaco, Germany*, March 26-29, 2009.
  - [9] Z. Q. ZHU and D. HOWE, “Influence of design parameters on cogging torque in permanent magnet machines”, *IEEE Trans. on Energy Conversion*, vol. 15, no. 4, pp. 407-412, 2000.
-

## Bibliography

---

- [10] N. BIANCHI, S. BOLOGNANI and E. FORNASIERO, “A general approach to determine the rotor losses in three-phase fractional-slot PM machines”, *IEEE Int. Electric Machines and Drives Conf.*, vol. 1, pp. 634-641, 2007.
- [11] F. MEIER, *Permanent-Magnet Synchronous Machines with Non-Overlapping Concentrated Windings for Low-Speed Direct-Drive Applications*, Stockholm: Doctoral thesis, Royal Institute of Technology, 2008.
- [12] S. E. SKAAR, Ø. KRØVEL and R. NILSSEN, “Distribution, coil-span and winding factors for PM machines with concentrated windings”, [Online]. Available: <http://www.elkraft.ntnu.no/eno/Papers2006/icem-skaar-krovel-nilssen06.pdf>. [Accessed 22 august 2017].
- [13] B. M. WILAMOSKI and J. D. IRWIN, *The industrial Electronics Handbook, Power Electronics and Motor Drives*, CRC Press, 2009.
- [14] A. M. EL- REFAIE and T. M. JAHNS, “Optimal flux weakening in surface PM machines using fractional-slot concentrated windings”, *IEEE Trans. Ind. Appl.*, vol. 41, no. 3, pp. 790-799, 2005.
- [15] J. F. GIERAS and M. WING, *PERMANENT MAGNET MOTOR TECHNOLOGY - Design and applications*, Second ed., New York: Marcel Dekker, Inc., 2002.
- [16] “Types of Permanent Magnets”, MAGCRAFT, [Online]. Available: <https://www.magcraft.com/types-of-permanent-magnets>. [Accessed 23 August 2017].
- [17] N. BIANCHI, M. BARCARO and S. BOLOGNANI, “Electromagnetic and Thermal Analysis of Permanent Magnet Synchronous Machines”, in *Finite Element Analysis - From Biomedical Applications to Industrial Developments*, InTech, 2012.
- [18] M. LAZZARI, “Macchina a corrente continua”, in *Dispense di macchine elettriche*, Torino, Appunti on-line, Politecnico di Torino, 2011, p. 62.
- [19] A. VAGATI, Slide di azionamenti elettrici, Torino: Politecnico di Torino, 2015.
- [20] G. PELLEGRINO, A. VAGATI, P. GUGLIELMI and B. BOAZZO, “Performance comparison between Surface Mounted and Interior PM motor drives for Electric Vehicle application”, *IEEE Trans Ind. Electron.*, vol. 59, no. 2, pp. 803-3011, 2012.

## Bibliography

---

- [21] “Desktop Tools and Development Environment”, The MathWorks Inc., [Online]. Available: [http://www.mathworks.com/help/pdf\\_doc/matlab/buildgui.pdf](http://www.mathworks.com/help/pdf_doc/matlab/buildgui.pdf). [Accessed 22 08 2017].
- [22] J. PYRHÖNEN, T. JOKIKEN and V. HRABOVCOVÁ, Design of Rotating Electrical Machines, Second ed., John Wiley & Sons, Ltd, 2008.
- [23] Y. DUAN, *Method for design and optimization for Surface- Mount Permanent machines and Induction machines*, Georgia: Doctoral thesis, Georgia Institute of Technology, 2010.
- [24] D. MEEKER, Finite Element Method Magnetics: OctaveFEMM, Version 1.2, User's Manual, 2010.
- [25] C. SADARANGANI, Electrical machines - Design and analysis of induction and permanent magnet motors, Sweden: Division of Electrical Machines and Power Electronics, School of Electrical Engineering, Royal Institute of Technology, 2006.
- [26] S. VASCHETTO, A. TENCONI and G. BRAMERDORFER, “Sizing Procedure of Surface Mounted PM Machines for Fast Analytical Evaluations”, *IEEE Int. Electric Machines and Drives Conf.*, 21-24 May 2017.
- [27] G. WEI, Z. CHENGNING and D. YUGANG, “Design and Experiments of a Deep-slot Permanent Magnet Synchronous”, in *Proceeding of International Conference on Electrical Machines and Systems*, Seul, Korea, Oct. 8-11, 2007.
- [28] A. TESSAROLO, Costruzioni elettromeccaniche, Corso di Laurea di Ingegneria Elettrica e dell'automazione, Università degli studi di Trieste, 2010-2011.
- [29] R. KRALL, J. KRENN and A. SCHMID, “Comparison of Leakage Inductance between Fractional Slot Winding and Distributed Winding”, in *Int. Power Elect. and Mot. Con. Conf.*, Antalya, Turkey, 21-24 Sept. 2014.
- [30] M. LAZZARI, “Motori asincroni”, in *Dispense di macchine elettriche*, Torino, Appunti online, Politecnico di Torino, pp. II-8.
- [31] D. MARTINEZ, *Design of Permanent-Magnet Synchronous Machine with Non-Overlapping Concentrated Winding for Shell Eco Marathon Urban Prototype*, Stockholm: Master's thesis, Royal Istitute of Technology, 2010.

## *Bibliography*

---

- [32] ZIJIAN LI, *Fractional-slot concentrated winding surface-mounted permanent magnet motor design and analysis for in-wheel application.*, Torino: Doctoral Thesis, Politecnico di Torino, 2012.

# Acknowledgements

Since I started to work on my Master's thesis several people have been involved. Hereby, I would like to thank them.

First of all, I want to express my deep gratitude to my supervisor, Silvio Vaschetto, for giving me his help when I needed it and for being my guidance throughout the project.

I would like to thank Prof. Andrea Cavagnino who helped me to discover who I want to be in the future with his course on electrical machines.

Grazie ai miei amici più cari, Claudio, Max e Biagio, che in questi anni sono stati la mia seconda famiglia. Grazie per essere stati sempre presenti, per avermi sempre sopportato e supportato. Grazie per le risate, le discussioni e i momenti felici trascorsi insieme. Per avermi consigliato, ascoltato e voluto bene come un fratello.

Quiero agradecer mis amigos Elio y Vittorio, con lo cual he vivido momento mágicos en Sevilla. Gracias por ser mis amigos, por aguantarme, por estar siempre a mi lado. La distancia que nos separa no podrá jamas dividir nuestra sincera amistad.

Thanks to my girlfriend Anneli, my better half, my German sweetheart. Thanks for being at my side at any time, despite of distance. Thanks for being patient when I was stressed or worried. Thanks for your love, mein Schatz.

Infine, voglio esprimere la mia profonda gratitudine ai miei genitori, perché senza di loro non potrei essere qui. Grazie per avermi sempre supportato in questi anni, economicamente ed emotivamente. Grazie per avermi asciugato le lacrime nei momenti di difficoltà e di incertezza sul futuro. Grazie per aver condiviso con me le gioie e per avermi sempre spinto a non accontentarmi mai. Grazie, perché se sono quello che sono, lo devo solo a voi e a nessun altro.

Voglio anche ringraziare lei, che mi guarda da lassù, per essere stata la mia forza più grande e la mia stella di riferimento quando mi sentivo in balia delle onde.

---